Max-Planck-Institut
für Meteorologie

MAX-PLANCK-GESELLSCHAFT

International Max Planck Research School
on Earth System Modelling

Wave-mean flow interactions driving the quasi-biennial oscillation in ECHAM6

Thomas Krismer

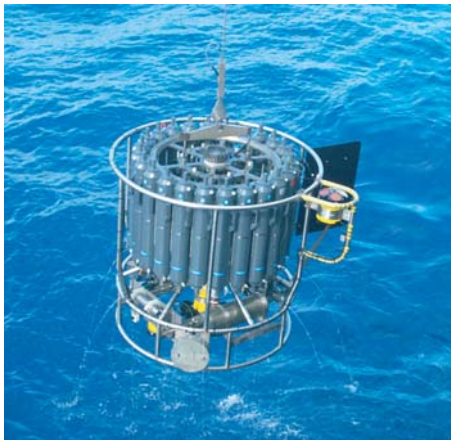

Berichte zur Erdsystemforschung 149/2014

Reports on Earth System Science

Hinweis

Die Berichte zur Erdsystemforschung werden vom Max-Planck-Institut für Meteorologie in Hamburg in unregelmäßiger Abfolge herausgegeben.

Sie enthalten wissenschaftliche und technische Beiträge, inklusive Dissertationen.

Die Beiträge geben nicht notwendigerweise die Auffassung des Instituts wieder.

Die "Berichte zur Erdsystemforschung" führen die vorherigen Reihen "Reports" und "Examensarbeiten" weiter.

Notice

The Reports on Earth System Science are published by the Max Planck Institute for Meteorology in Hamburg. They appear in irregular intervals.

They contain scientific and technical contributions, including Ph. D. theses.

The Reports do not necessarily reflect the opinion of the Institute.

The "Reports on Earth System Science" continue the former "Reports" and "Examensarbeiten" of the Max Planck Institute.

Anschrift / Address

Max-Planck-Institut für Meteorologie
Bundesstrasse 53
20146 Hamburg
Deutschland

Tel.: +49-(0)40-4 11 73-0
Fax: +49-(0)40-4 11 73-298
Web: www.mpimet.mpg.de

Layout:

Bettina Diallo, PR & Grafik

Titelfotos:
vorne:
Christian Klepp - Jochem Marotzke - Christian Klepp
hinten:
Clotilde Dubois - Christian Klepp - Katsumasa Tanaka

Berichte zur Erdsystemforschung 149/2014

Wave-mean flow interactions driving the quasi-biennial oscillation in ECHAM6

Thomas Krismer

aus Rum in Österreich

Hamburg 2014

Reports on Earth System Science 149/2014

ISSN 1614-1199

Thomas Krismer
Max-Planck-Institut für Meteorologie
Bundesstrasse 53
20146 Hamburg

Als Dissertation angenommen
vom Department Geowissenschaften der Universität Hamburg

auf Grund der Gutachten von
Prof. Dr. Bjorn Stevens
und
Dr. Marco Giorgetta

Hamburg, den 13. November 2013
Prof. Dr. Christian Betzler
Leiter des Departments für Geowissenschaften

ISSN 1614-1199

Wave-mean flow interactions driving the quasi-biennial oscillation in ECHAM6

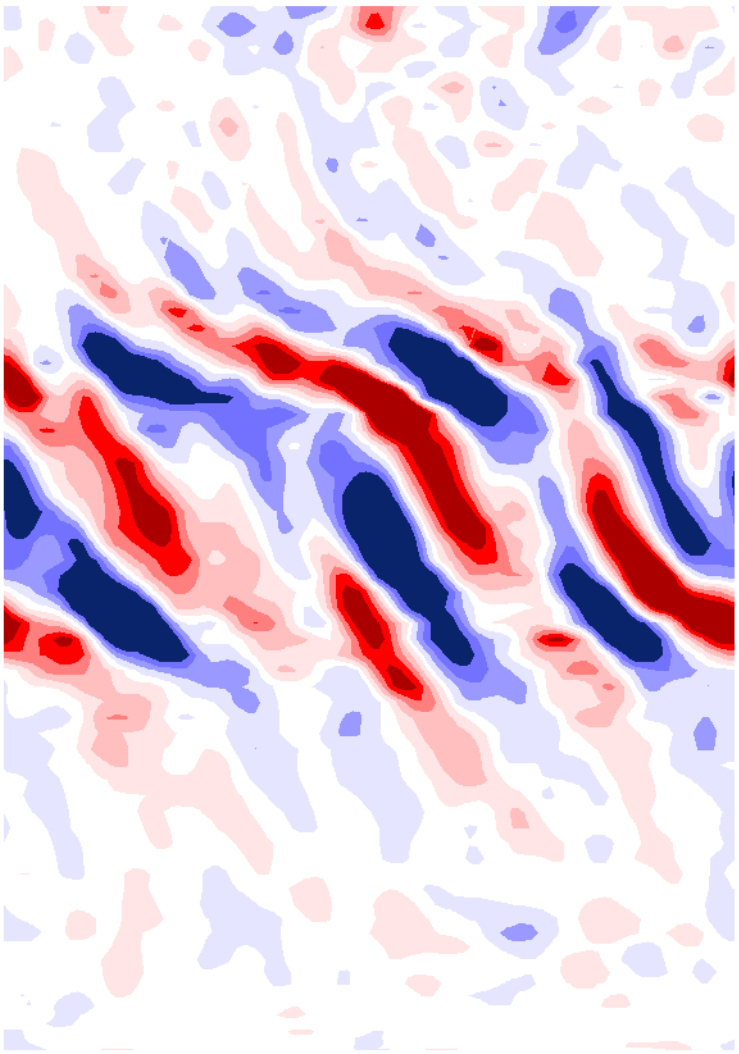

Thomas Krismer

Hamburg 2013

Abstract

This thesis investigates the dynamics of the quasi-biennial oscillation of the tropical stratosphere (QBO). For this purpose, the general circulation model ECHAM6 and the Max Planck Institute Earth System Model, which both internally generate the QBO, are applied. The QBO of the zonal wind is the dominant mode of variability in the tropical stratosphere and is driven by a large spectrum of mostly convectively triggered, vertically propagating waves. The representation of these waves in the applied models is investigated based on zonal wave number-frequency spectra of tropical precipitation, temperature and the eddy momentum flux. The waves deposit easterly and westerly momentum due to radiative and diffusive wave damping, critical level filtering and wave breaking and hence, force the QBO jets. The thesis relates the vertical structure and amplitude of Matsuno-type Kelvin waves to their radiative damping and compares the importance of radiative and diffusive damping for large scale equatorial waves and small scale gravity waves. Profiles of the EP-Flux and its divergence illustrate the dissipation of waves in the vicinity of the zero wind lines associated with the onset of the QBO jets. A comparison of the resolved wave field in two versions of ECHAM6 truncated at T63 and T255, respectively (1.9° and 0.4° horizontal resolution, respectively), comprehends the evolution of the wave field when resolving an increased part of the wave spectrum and illustrates the importance of these small scale waves for the forcing of the QBO. The thesis is concluded by the investigation of the dynamic sources of the well observed seasonal modulations of the quasi-biennial cycle by seasonal variations of the wave forcing and the equatorial upwelling and by the semi-annual oscillation in the upper stratosphere. In the ECHAM version truncated at T63, the model underestimates the strength of the tropospheric wave sources with wave numbers higher than 20 and periods shorter than two days, which suggests that also the wave momentum flux at theses spectral ranges is too low. However, in agreement with high-resolution model studies, resolved waves with planetary wave-numbers lower than 40 contribute up to 50% and 30% to the forcing of the QBO westerly and easterly jet, respectively. Large scale equatorial waves are mostly damped by long wave radiative damping, whereas small scale gravity waves are damped by horizontal diffusion. Due to the radiative and diffusive wave damping, the wave momentum flux decreases with increasing distance from the tropospheric wave sources, even in the absence of critical levels. Hence, the wave momentum flux available to force the QBO decreases with increasing altitude of the zero wind lines marking the onset of the easterly and westerly jets. The resolved wave forcing in the high resolution version of ECHAM6 is stronger than in the low resolution version equally due to weaker damping of waves with planetary wave numbers ranging from 20 to 63, which are present in both versions, and due to the representation of previously unresolved waves with zonal wave numbers from 64 up to 255. Seasonal variations of the strength of resolved large scale equatorial waves, parametrized small scale gravity waves and the equatorial upwelling contribute equally to the stalling of the QBO easterly jet in the lower stratosphere. In the upper stratosphere, small scale waves and vertical upwelling dominate the momentum balance and hence, dictate seasonal modulations. The well observed phase alignment of the onset of the QBO jets in a specific season of the year can be attributed to the semi-annual oscillation in the upper stratosphere, which periodically facilitates the development of QBO westerly jets.

Contents

Chapter 1

Introduction

After the eruption of Mount Krakatoa in today's Indonesia in 1883, observations of the edge of the ash cloud from all around the tropics indicated a regular easterly motion of the volcanic aerosols. In 1908, however, sporadic balloon observations from Equatorial Africa indicated westerly winds in the lower stratosphere. By the midst of the 20^{th} century, balloon observations of the tropical stratospheric winds became more systematic and soon showed that zonally uniform easterly and westerly jets originate in the upper stratosphere and propagate downwards to the vicinity of the tropical tropopause (Veryard and Ebdon, 1961; Reed et al., 1961). At any altitude, the jets oscillate with an irregular period close to two years ranging from 22 to 36 months (Baldwin et al., 2001). Thus, the phenomenon became know as the Quasi-Biennial Oscillation (QBO).

Early attempts to explain the QBO with quasi-biennial variations of the diabatic heating rate or the eddy momentum flux from the extra-tropics into the tropical stratosphere failed. These theories required unrealistically large amplitudes of the heating rates or the momentum flux and more importantly, could not explain the downward propagation of the QBO jets (see Lindzen and Holton, 1968). Lindzen and Holton (1968) and Holton and Lindzen (1972) developed the first successful theory on the QBO, which states that the QBO is driven by vertically propagating atmospheric waves which deposit easterly and westerly momentum due to radiative attenuation, critical layer absorption and wave breaking. The wave attenuation is most effective where the zonal phase speed of a wave is close to the zonal wind speed. Waves which deposit their wave momentum around the zero wind line between easterly and westerly jets drive the zero wind line downwards, towards the wave sources. Strong diffusion in the lowermost stratosphere hinders the further propagation of the jets, which thus, are eroded by the subsequent jet of the opposite phase. Dunkerton (1991) showed that the generally upward directed residual vertical motion in the tropics tends to advect the QBO jets upwards and hence, works against their downward propagation. Observational and modeling studies showed that a continuous spectrum of large scale equatorial waves and small scale gravity waves transports the momentum necessary to propagate the QBO jets against the resistance of the tropical upwelling (Dunkerton, 1997; Sato and Dunkerton, 1997; Ern et al., 2009a; Ortland et al., 2011; Kawatani et al., 2010a; Evan et al., 2012b). The waves are mostly triggered by tropical convection (Holton, 1972;

Manzini and Hamilton, 1993; Fritts and Alexander, 2003).

Next to being a unique phenomenon of wave-meanflow interactions, the QBO is well known to influence the general circulation outside the tropical stratosphere. When the zonal wind at 50 hPa is in the QBO westerly phase in boreal winter, the southward propagation of extra-tropical planetary Rossby waves is confined to the northern hemisphere (Holton and Tan, 1980). Hence, the waves are more likely to interact with the stratospheric polar vortex which thus, becomes weaker (Holton and Tan, 1980; Baldwin and Dunkerton, 1991; Dunkerton and Baldwin, 1991). Via the stratospheric/tropospheric coupling found by Baldwin and Dunkerton (2001), this so called Holton and Tan effect (after Holton and Tan, 1980), perturbs the tropospheric circulation (Thompson and Wallace, 2001) and the resulting QBO temperature signal during northern hemispheric winters is comparable to ENSO (Thompson et al., 2002).

The QBO also modulates the vertical extent and intensity of tropical deep convection (Giorgetta et al., 1999; Liess and Geller, 2012), the distribution and transport of water vapor and other trace gases (Mote et al., 1996; Schoeberl et al., 2008; Punge and Giorgetta, 2008), and the stratospheric and tropospheric signal of the solar cycle (Labitzke, 1987; Labitzke and Loon, 1988).

Due to the influence of the QBO on the dynamics and chemistry of the climate system, it is desirable to simulate the QBO in general circulation models (GCM). Vice versa, GCMs are still the optimal choice for studies of the QBO dynamics, as owing to the wide range of scales involved in QBO dynamics, from planetary scale Matsuno type equatorial waves (Matsuno, 1966; Lindzen and Holton, 1968) to small scale gravity waves Dunkerton (1997), it is not yet possible to close the stratospheric momentum balance based on observations (Evan et al., 2012a).

Takahashi (1996, 1999) modeled the QBO with spectral models truncated at zonal wave number 21 and 42, which thus, did not resolve waves with zonal wave lengths shorter than 2000 and 1000 km, respectively. However, the damping time scales required to allow these relatively large scale waves to transport sufficient momentum to drive the QBO were inappropriate to simulate a realistic global climate (Takahashi, 1996, 1999). Hence, unresolved waves and their interaction with the resolved flow are parametrized, as done by Scaife et al. (2000) and Giorgetta et al. (2002). Based on an atmospheric general circulation model truncated at zonal wave number 42 with 90 vertical levels and including the Hines parametrization for non orographic gravity waves, Giorgetta et al. (2006) showed that resolved large-scale waves are particularly important for the QBO westerly phase, while the parameterized gravity wave drag is more important for the QBO easterly phase. Kawatani et al. (2010a); Ortland et al. (2011) and Evan et al. (2012b) modeled the wave forcing of the QBO with high resolution models. They decomposed the stratospheric wave field into its spectral components and showed that waves with zonal wave numbers up to 200 (λ=200 km at the equator) contribute considerably to the QBO's momentum budged.

Based on the existing studies, the goal of this thesis is to analyze the wave meanflow interactions driving the QBO in a GCM in detail, to differentiate the roles of the different portions of the involved tropical wave spectrum in forcing the QBO jets, to analyze the influence of the structure of the QBO on the wave field and to investigate the processes responsible for the dissipation of the waves in the GCM. Chapter 2 and 3 of the

thesis extend the work of Giorgetta et al. (2006) by analyzing the spectral distribution of the resolved wave field as simulated with the atmospheric model ECHAM6 (Stevens et al., 2012), which is the direct successor of MAECHAM. Thus, the thesis quantifies the contribution of waves with different scales to the forcing of the QBO as done by Kawatani et al. (2010a) and Evan et al. (2012b) for GCMs with, compared to their studies, course horizontal and vertical resolution. Similar to ECHAM6, most of today's GCMs have horizontal resolutions in the order of 1.9 ° and use some sort of gravity wave parametrization to account for unresolved waves. Over the last decade, increased efforts to improve the representation of the stratosphere in atmospheric models led to a limited number of GCMs which also have a sufficiently high vertical resolutions to accurately simulate the wave-meanflow interaction of the resolved and parametrized waves and hence, internally generate a QBO. However, next to Giorgetta et al. (2006) reports on the QBO dynamics in such GCMs are scarce. The thesis aims at filling this gap.

Further, radiative and diffusive wave damping, wave breaking and wave filtering at critical levels, which are crucial for the wave-meanflow interactions driving the QBO, are well described in theory (Booker and Bretherton, 1967; Fels, 1982; Zhu, 1993) and in idealized models (Ern et al., 2009a). However, there are no comprehensive studies of the means by which wave damping processes interplay with the QBO dynamics. The thesis relates the vertical structure and amplitude of resolved waves to the radiative damping and compares the importance of radiative and diffusive wave damping for large scale equatorial waves and small scale gravity waves.

For the resolved scales, the thesis investigates the representation of the following processes in MPI-ESM, which are crucial in order to simulate the wave-meanflow interactions driving the QBO. First, the model has to excite a spectrum of tropical waves. The latent heating within convective clouds is considered the most important wave source in the tropics (Holton and Lindzen, 1972; Manzini and Hamilton, 1993; Fritts and Alexander, 2003, and references therein) and hence, the amplitude and the spatial and temporal variability of tropical convection in a GCM determines the amount of resolved wave momentum available to force the QBO. Second, the model has to allow the waves to carry wave momentum away from the tropospheric wave sources towards the shear zones associated with the QBO jets and third, the model has to provide mechanisms for the waves to dissipate in order to deposit the wave momentum and accelerate the QBO jets, such as radiative and diffusive wave damping.

It will be shown in Chapter 2 that due to the numerical diffusion applied in the ECHAM6 version truncated at T63, waves with wave numbers larger than 30 do not contribute much to the vertical transport of zonal momentum. As in models with comparable resolution, the lack of resolved waves is compensated by the gravity wave parametrization. However, these parametrizations generally do not reach the full complexity and accuracy of wave generation and wave-meanflow interactions and it is desirable to resolve the waves necessary to drive the QBO with GCMs having high horizontal and vertical resolution. Chapter 3 illustrates the wave forcing of the QBO in low and high resolution models based on AMIP-type simulations conducted with two versions of ECHAM6 with spectral truncations of T63 and T255 (1.9° and 0.4° horizontal resolution, respectively) and 95 vertical levels (700 m vertical resolution).

Thus, Chapter 3 provides a link between model studies of the QBO relying on resolved and parametrized waves such as in Giorgetta et al. (2006) and Chapter 2 of this thesis, and studies where the QBO is entirely forced with resolved waves as in Kawatani et al. (2010a) and Evan et al. (2012b).

Chapter 2 and 3 strongly focus on the generation, propagation and dissipation of equatorial waves and the resulting forcing of the QBO jets. Chapter 4 broadens the perspective from a single QBO phase as in Chapter 2 and 3 to the whole quasi-biennial cycle and investigates how seasonal variations of the wave forcing and the equatorial upwelling cause the well observed seasonal modulations of the quasi-biennial cycle. Observations show that at every altitude, the transitions from QBO easterly to QBO westerly jets et vice versa, cluster in a specific season (Dunkerton, 1990; Anstey and Shepherd, 2008). Further, the QBO phases progress more rapidly in boreal winter and spring than in summer and fall (Wallace et al., 1993; Hamilton and Hsieh, 2002; Lu et al., 2009) and the QBO easterly jet shows the tendency to stall below 30 hPa between June and February (Naujokat, 1986; Dunkerton, 1990; Pascoe et al., 2005). Another seasonal modulation of the QBO emerges from its interaction with the semiannual oscillation in the uppermost stratosphere (SAO). In the original theory of the QBO presented by Lindzen and Holton (1968), the SAO provides the westerly shear in the upper stratosphere, which is needed for effective deposition of westerly momentum by atmospheric waves. Though it has been shown in idealized model studies that the spontaneous generation of the QBO is possible without the SAO (Holton and Lindzen, 1972; Plumb, 1977; Mayr et al., 2010), the interaction of the QBO and the SAO has been observed in multiple studies (Gray and Pyle, 1989; Dunkerton and Delisi, 1997; Kuai et al., 2009).

From the seasonal aspects of the QBO discussed above, the following questions discussed in this paper arise:

How does the interaction of the QBO and the SAO influence the phase alignment of the QBO jets in the upper stratosphere and how does this phase alignment project to lower altitudes?

How does the seasonal stalling of the QBO jets in the lower stratosphere influence the propagation rates of the jets in the upper stratosphere?

How do seasonal variations of the equatorial wave forcing and the tropical upwelling contribute to variations of the propagation rates of the QBO jets?

Previous modeling studies addressing seasonal modulations of the QBO investigate the influence of a prescribed variation of the vertical velocities on QBO-like oscillations within simplified models (Kinnersley and Pawson, 1996; Hampson and Haynes, 2004). In this respect, an investigation within the setting of GCM and considering all aspects of the QBO forcing is still missing. Therefore, Chapter 4 investigates the dynamics behind seasonal modulations of the QBO based on a 500 year simulation conducted with MPI-ESM usind preindustrial boundary conditions (piControl, Giorgetta et al., 2012).

Chapters 2, 3 and 4 are written in the style of journal publications and contain their own abstract, introduction and conclusions and can be read independently of each other. Chapter 2 and Chapter 3 are in preparation for submission and Chapter 4

has been published. Chapter 5 gives a summary of the main conclusions of the three previous chapters.

Chapter 2

Wave Forcing of the Quasi-Biennial Oscillation

Abstract: This study investigates the resolved wave forcing of the Quasi-Biennial Oscillation (QBO) in the Max Planck Institute Earth System Model truncated at T63 with 95 vertical levels. The model, which parametrizes unresolved gravity waves, internally generates a QBO. The resolved waves contribute up to 50% and 30% to the total wave forcing (resolved plus parametrized) of the QBO westerly and easterly jet, respectively, mostly due to waves with zonal wavenumbers lower than 20 and frequencies lower than 0.5 cycles per day. At higher frequencies and wavenumbers, the model underestimates the strength of the tropospheric wave sources when compared to TRMM observations and applies strong horizontal diffusion, which explains the, compared to recent studies based on high resolution models, shortage of wave momentum at these scales. The study further relates the vertical structure of equatorial Kelvin waves, which contribute most to the transport and deposition of westerly wave momentum, to their radiative dissipation and compares the role of longwave radiation and horizontal diffusion for the dissipation of the resolved waves in general. The Kelvin waves adjust their vertical wavelength according to their intrinsic phase speed and are efficiently damped by longwave radiation within westerly flow, where the vertical wavelength strongly decreases. Waves with zonal wavenumbers larger than 10, however, are mostly damped by horizontal diffusion. The latitudinal distribution of the resolved wave forcing reflects the latitudinal structure of the waves and is asymmetric with respect to the equator.

2.1 Introduction

The variability of the general circulation in the tropical stratosphere is dominated by the wave driven Quasi-Biennial Oscillation (QBO) (Baldwin et al., 2001). The QBO most clearly manifests itself in easterly and westerly jets which originate in the upper stratosphere, propagate downwards to the vicinity of the tropopause and oscillate with a period ranging from 22 to 34 months (Baldwin et al., 2001).

Lindzen and Holton (1968) and Holton and Lindzen (1972) presented and refined the first plausible theoretical explanation of the QBO. They argued that the QBO is driven

by vertically propagating atmospheric waves which deposit easterly and westerly momentum due to radiative attenuation and wave breaking in the vicinity of the waves' critical levels, where the phase speed of a wave is close to the background windspeed. Waves which deposit their wave momentum around the zero wind line between easterly and westerly jets drive the zero wind line downwards, towards the wave sources. Dunkerton (1991) showed that the generally upward directed residual vertical motion in the tropics tends to advect the QBO jets upwards and hence, works against their downward propagation.

After a number of observational and modelling studies, it is now established that a continuous spectrum of large scale equatorial waves and small scale gravity waves transports the momentum necessary to propagate the QBO jets against the resistance of the tropical upwelling (Sato and Dunkerton, 1997; Canziani and Holton, 1998; Ern and Preusse, 2009a,b; Kawatani et al., 2010a; Evan et al., 2012b). The waves are mostly triggered by tropical convection (see Fritts and Alexander, 2003, and references therein).

The QBO influences the stratospheric circulation in the extratropics (Holton and Tan, 1980; Anstey and Shepherd, 2013; Watson and Gray, 2014) and the distribution of trace gases in the stratosphere (Mote et al., 1996; Schoeberl et al., 2008; Punge and Giorgetta, 2008). Further, owing to the wide range of scales, from planetary scale Matsuno-type equatorial waves (Matsuno, 1966) to small scale gravity waves, it is not yet possible to close the stratospheric momentum balance based on observations. Thus, to cover the full range of stratospheric variability and to study stratospheric dynamics, it is desirable to internally generate the QBO in general circulation models (GCMs). However, the number of GCMs capable of simulating a QBO is still limited.

In order to internally generate a QBO like oscillations comparable to observations, GCMs need to transport sufficient wave momentum into the stratosphere, either by applying some sort of gravity wave parametrization scheme to substitute unresolved waves (Scaife et al., 2000; Giorgetta et al., 2002; Orr et al., 2010; Xue et al., 2012) or by resolving the relevant wave spectrum using high horizontal resolution (Kawatani et al., 2010a; Evan et al., 2012b). A high vertical resolution is necessary to accurately simulate the waves' response to the changing background flow (Giorgetta et al., 2006).

Giorgetta et al. (2006) presented a climatology of the forcing of the QBO based on an operational GCM, showing that parametrized small scale gravity waves are as important in forcing the QBO as the resolved waves with zonal wavenumbers up to 42. The spectral distribution of the QBO's wave forcing has been presented by Kawatani et al. (2010a) and Evan et al. (2012b), however, due to the computational costs of their heigh resolution experiments, their results covered only two quasi-biennial cycles or even months. This study presents a detailed spectral analysis of the resolved wave forcing of the QBO as done by Kawatani et al. (2010a) and Evan et al. (2012b), however, based on a 500 year long simulation conducted with the operational Max Planck Earth System Model (MPI-ESM) truncated at T63 and thus, continues the work of Giorgetta et al. (2006). The study therefore gives a reference for the QBO forcing in the current generation of GCMs with relatively course resolution.

In earlier studies, the wave-meanflow interactions driving the QBO have been discussed indirectly based on the divergence of the wave momentum flux in regions of strong ver-

tical shear associated with the QBO jets. Ern and Preusse (2009b) and Yang et al. (2011) illustrated the underlying wave attenuation at hand of the loss of spectral power of filtered wave modes with altitude. However, literature lacks the explicit discussion of the dynamical and physical mechanisms by which GCMs dissipate resolved waves, which are diffusive and radiative wave damping and which are covered in theoretical work (Fels, 1982; Zhu, 1993), idealized model studies (Holton and Lindzen, 1972; Ern et al., 2009a) and implemented in gravity wave parametrization schemes. With respect to increased efforts in understanding the spread of QBO features among models in recent years, understanding these fundamental wave mechanics is crucial. It is one of the main goals of this study to show how long wave radiation and diffusion damp different parts of the resolved wave spectrum in MPI-ESM and thus, lead to the acceleration of the mean flow and the generation of a QBO like oscillation. This includes the modulation of the waves' vertical structure during opposite QBO phases, the implications for the long wave radiative damping processes and a comparison of radiative and diffusive wave damping for different parts of the wave spectrum.

The study is structured as follows. Sections 2.2 and 2.3 give a short description of the applied model and the simulated QBO. Section 2.4 validates the spectra of tropical precipitation as a proxy for the convective wave sources and thus, contributes to the ongoing discussion about the strength of tropospheric wave sources necessary to force the QBO (Lott et al., 2013). Section 2.5 describes the filtering of the stratospheric wave field by the QBO jets and the underlying wave dissipation processes. Section 2.6 presents profiles of the wave momentum flux and the wave momentum deposition during opposite QBO phases, which are extended to latitudinal cross sections and to the whole quasi biennial cycle. Section 2.7 presents the total momentum balance including the parametrized wave forcing and advection.

2.2 Model description

This work makes use of the Max Planck Institute Earth System Model (Giorgetta et al., 2013b) in the MR configuration, which consists of the ECHAM6 atmospheric GCM (Stevens et al., 2012), the JSBACH land vegetation model (Raddatz et al., 2007) and the MPIOM ocean GCM (Jungclaus et al., 2013) including the HAMOCC ocean bio-geochemistry model (for brevity, the generic name MPI-ESM is used in the following text). The MR configuration designates the resolution of atmosphere and ocean GCMs, where the ocean model makes use of a tripolar grid with a nominal resolution of 0.4°. The vertical grid has 40 z-levels. In the "MR" configuration, the atmospheric component ECHAM6 uses a spectral truncation at wavenumber 63 and an associated Gaussian grid of approximately 1.9° resolution in longitude and latitude. The vertical grid has 95 hybrid sigma pressure levels resolving the atmosphere from the surface up to the center of the uppermost layer at 0.01 hPa. The top-of-the-model pressure is defined as 0 hPa. This grid has a nearly constant vertical resolution of 700 m from the upper troposphere to the middle stratosphere, and the resolution is better than 1 km at the stratopause. Thus the vertical grid is overall comparable to that used by Giorgetta et al. (2006) with respect to the vertical resolution in the QBO domain. MPI-ESM is capable of internally generating a QBO with a realistic period, vertical

extent and seasonal modulations, but overestimates the QBOs amplitude (Krismer et al., 2013).

The parametrization of convection, which is known to influence the resolved wave field (Horinouchi et al., 2003), follows the Tiedtke-Nordeng scheme (Möbis and Stevens, 2012). ECHAM6 includes the Hines parametrization for non-orographic gravity waves (Hines, 1997a,b). The source spectrum of the Hines parametrization follows the MAECHAM5 standard setting (Manzini and McFarlane, 1998; Manzini et al., 2006). However, the otherwise constant wave-induced horizontal wind perturbations (rms winds) increase linearly from 1 to 1.2 m/s over 10°N to 5°N (10°S to 5°S). From 5°N to 5°S, the rms winds are constant at 1.2 m/s. The modification of the source spectrum of the Hines parametrization was necessary to obtain a realistic QBO period in MPI-ESM, where ECHAM6 is coupled to an ocean model. Due to non-linearities, the 20 % increase of the rms winds leads to a four times larger parametrized wave drag at the zero wind lines associated with the onset of the QBO jets. Given the lack of observational constraints on tropical gravity waves and considering that the mostly convective non-orographic wave sources, which are represented by the Hines scheme, are more abundant in the tropics than in the extra-tropics, such an enhancement seems to be justified. Giorgetta et al. (2006) showed that increasing the rms winds in MAECHAM5 by 10 % strengthens the QBO westerly jets and reduces the period. With an idealized one dimensional model, Scaife et al. (2000) showed that the QBO period generally decreases with increasing parametrized wave sources. The prescribed gravity wave sources are constant in time and the wave source is at 700 hPa.

MPI-ESM has been used for many CMIP5 simulations (Taylor et al., 2009). A number of recent publications based on MPI-ESM and its components review the dynamics of the middle atmosphere (Schmidt et al., 2012a), the seasonal modulation of the Quasi-Biennial Oscillation (Krismer et al., 2013), the stratosphere-troposphere coupling (Tomassini et al., 2012), tropical precipitation (Crueger et al., 2013) and model tuning (Mauritsen et al., 2012) for MPI-ESM. This study makes use of the pre-industrial CMIP5 control simulation (piControl), which is forced by 1850 conditions and was integrated over 1000 years (Giorgetta et al., 2012). Most of this study refers to the first 30 years of the piControl simulation, which is the only period where the parametrized gravity wave drag, the longwave radiative temperature tendency and the horizontal and vertical diffusion have been stored. The first 30 years analyzed in section 2.5 include 14 quasi-biennial cycles. The first 500 simulated years, which are analyzed to discuss the resolved wave drag in section 2.6, include 209 quasi-biennial cycles.

2.3 Mean structure of the QBO

Figure 2.1 shows the time height cross section of the zonal mean zonal wind in the tropical stratosphere over a 15 year period in ERA-40 and MPI-ESM. Though ERA-40 seems to have an easterly bias prior to the 1980ies (Punge and Giorgetta, 2008), it is known to well represent the amplitude and variance of the QBO (Baldwin, 2005). In Figure 2.1, the QBO clearly shows in the oscillation of westerly and easterly jets between 5 and 100 hPa. In the displayed 15 years, the reanalysis and the model complete

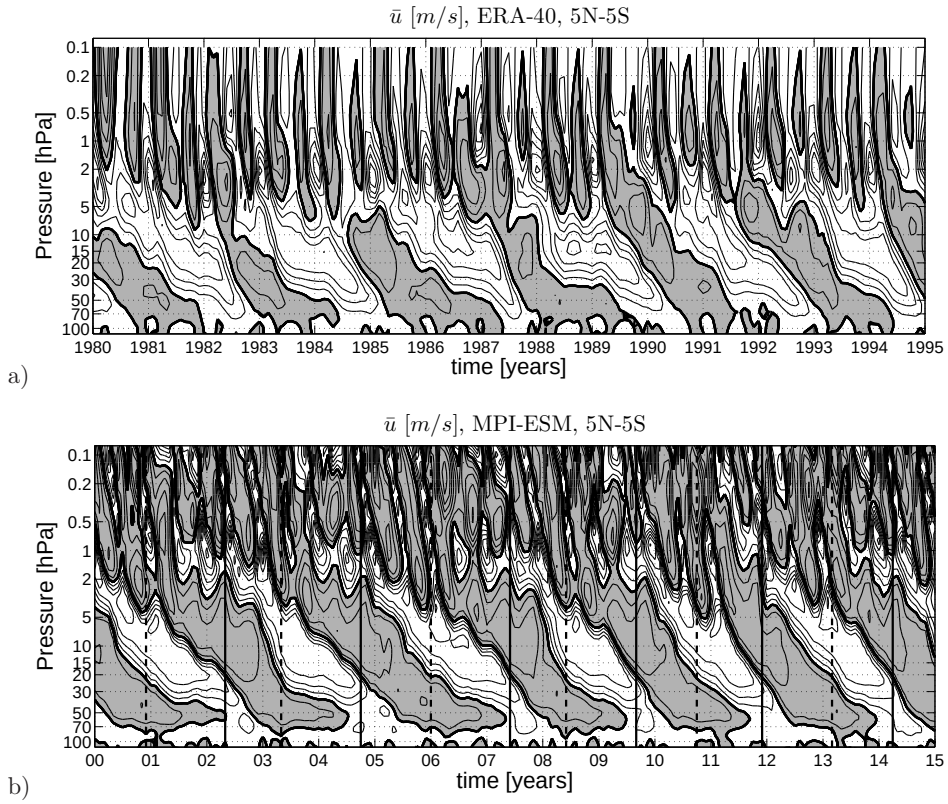

Figure 2.1: Time-height cross section of the zonal mean zonal wind in ERA-40 (a) and MPI-ESM (b). The contour interval is 10 m s^{-1}. Positive wind speeds are shaded in gray. The thick contour indicates the zero wind line. Thick vertical lines in panel b indicate months referred to as QBO westerly (solid lines) and easterly (dashed lines) phase.

about 6 quasi-biennial cycles. Over the whole 500 years of the model simulation, the average QBO period in MPI-ESM is 28.7 months, which corresponds well to observations (Baldwin et al., 2001). MPI-ESM covers the regular downward propagation rates of the QBO westerly jets as well as the stalling of the easterly jets below 30 hPa. The semiannual oscillation above 5 hPa is stronger in MPI-ESM than in ERA-40. However, consistent with the reanalysis, the SAO westerly jets penetrate to deeper altitudes in months when the QBO westerly jet is at low altitudes and comparatively weak. In ERA-40, the QBO jets are strongest at 20 hPa, where the QBO easterly and westerly jets exceed -30 and +10 m/s, respectively (Fig. 2.1a). In MPI-ESM, the QBO jets reach their maximal strength higher than in ERA-40 at 10 hPa (Fig. 2.1b). The QBO westerly jet in MPI-ESM is about 50% stronger than in observations, and exceeds +20 m/s. Above 30 hPa, the strength of the QBO easterly jet matches ERA-40, however, it does not penetrate as deep as in the reanalysis dataset. For further comparison of the QBO in MPI-ESM and ERA-40, the reader is referred to Krismer et al. (2013)

Most of this study will focus on the wave mean flow interactions in MPI-ESM during two phases within a quasi-biennial cycle, which are indicated by thick vertical lines in Figure 2.1b. The phases are defined by first finding a pair of months where the zonal wind at 20 hPa changes its sign. The month where the zonal wind is closer to 0 m/s is sampled. At 20 hPa, such a wind reversal occurs only twice during a quasi-biennial

cycle, once when the wind turns from easterly to westerly (solid vertical lines in Fig. 2.1b) and once when it turns from westerly to easterly (dashed vertical lines in Fig. 2.1b).

During months with a westerly wind transition at 20 hPa, the zonal wind is easterly below 20 hPa and westerly above. These months will hereafter be referred to as QBO westerly phase (solid lines in Fig. 2.1b). Likewise, during months with an easterly wind transition at 20 hPa, the zonal wind is westerly below 20 hPa and easterly above (dashed lines in Fig. 2.1b). These months will hereafter be referred to as QBO easterly phase. During the first 30 and the first 500 years of the piControl simulations analyzed here, 14 and 209 phase changes occur, respectively.

2.4 Spectral variability of tropical precipitation

The momentum necessary to drive the QBO is carried by a continuous spectrum of waves (Sato and Dunkerton, 1997; Canziani and Holton, 1998; Ern and Preusse, 2009b,a) which are mostly triggered by latent heat release within convective clouds (see Fritts and Alexander, 2003, and references therein). Tropical precipitation is a widely used proxy for tropical convective activity. Although Lott et al. (2013) found that the intermodel variability of Kelvin and Rossby wave activity at 50 hPa is less dependent on the intermodel variability of the precipitation spectra than anticipated before (Horinouchi et al., 2003), this section presents and validates the spectral characteristics of tropical precipitation in MPI-ESM to estimate the strength of tropical wave sources in a way comparable to earlier studies (Kawatani et al., 2010a; Evan et al., 2012b). MPI-ESM is validated against the 3B42 dataset from the satellite based Tropical Rainfall Measuring Mission (TRMM) (Huffman et al., 2007), which covers most of the rainfall events observed with gauge and radar measurements in the pacific

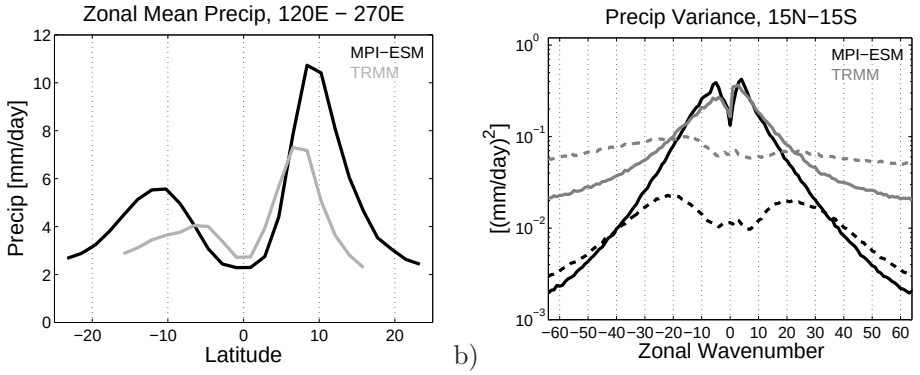

Figure 2.2: a) Latitudinal distribution of zonal mean tropical precipitation in the Pacific region in TRMM (gray line, averaged from 1998 to 2008) and MPI-ESM (black line, averaged over the first 11 years of the model run) in kg m^{-2} day^{-1}. b) Precipitation variance in TRMM (gray line) and MPI-ESM (black line) in (kg m^{-2} day^{-1})^2, averaged from 15°N to 15°S as a function of the zonal wavenumber. The variance has been integrated over frequencies ranging from 0 to 0.5 cpd (solid lines) and from 0.5 cpd to 2 cpd (dashed lines). Negative wavenumbers indicate easterly waves.

(Huffman et al., 2007) and is more accurate than most other global reanalysis products (Kim and Alexander, 2013).

Figure 2.2a shows the latitudinal distribution of the zonally averaged daily precipitation rates in TRMM and in MPI-ESM in the tropical pacific between 120°E and 270E°. Here, the TRMM data has been averaged from 1998 to 2008, and an equally long period has been chosen from the MPI-ESM piControl simulation. Both datasets show the highest precipitation rates north and south of the equator, however, compared to TRMM, the precipitation rates are generally higher and the peaks are shifted to higher latitudes in MPI-ESM.

To estimate the capability of MPI-ESM to simulate a realistic spectrum of convectively triggered waves, Figure 2.2b shows the precipitation variance in TRMM and MPI-ESM as a function of the zonal wavenumber for waves with frequencies between 0 and 0.5 cycles per day (cpd) and between 0.5 and 2 cpd. Before calculating the spectra, the TRMM data has been interpolated from the original 0.25° grid to the 1.9° grid used in MPI-ESM. Only 4 observations per day have been used (6, 12, 18 and 24 hours) to match the sampling rate of the model data. The spectra have been calculated as described by Wheeler and Kiladis (1999). First, the precipitation is partitioned into 128 day long time windows with an overlap of 75 days, which gives 72 time windows to cover the 11 year period. In every time window, the zonal and temporal means have been

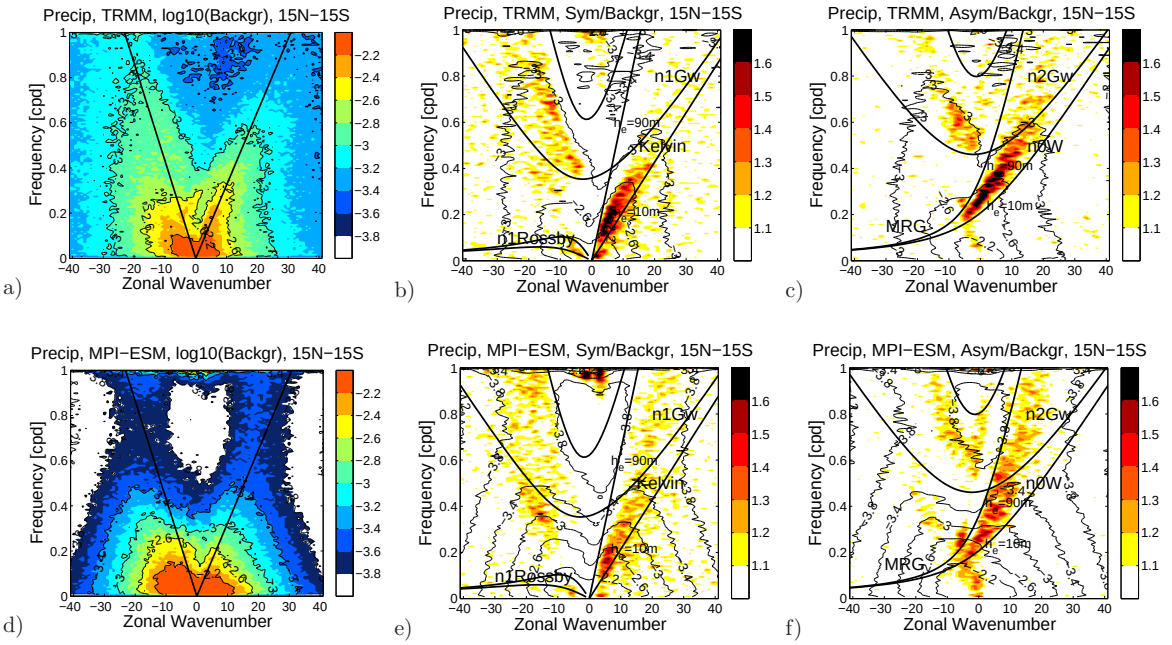

Figure 2.3: Latitudinal mean (15°N to 15°S) background, symmetric and antisymmetric zonal wavenumber-frequency spectra of precipitation variance in TRMM (a to c) and MPI-ESM (d to f) in $\log((\text{kg } m^{-2}\text{day}^{-1})^2)$. Black lines in a, d) are lines of constant phase speed of -20 and 15 m/s. The dispersion lines of symmetric Kelvin waves, easterly Rossby waves and n1 gravity waves (b, e) and the antisymmetric mixed Rossby gravity waves, n0 westerly waves and n2 gravity waves (c, f) with equivalent depths of 10 and 90 m are superimposed on the symmetric and antisymmetric spectrum, respectively. Negative wavenumbers indicate easterly waves.

subtracted from the data, and each time window has been tapered in time. Following Lin et al. (2006), the data has been averaged from 15°S to 15°N prior to calculating the wave spectrum. The latitudinal range fully includes the peaks in precipitation in MPI-ESM around ± 10° (Fig. 2.2a). The spectral powers are calculated by applying the fast Fourier transform in time and longitude on the precipitation data in each time window and then averaged over all time windows. Figure 2.2b demonstrates that compared to TRMM, MPI-ESM well simulates the precipitation variance at frequencies lower than 0.5 cpd and wavenumbers lower than ±20 (zonal wavenumber λ=2000 km), but underestimates the variance at wavenumbers larger than ± 20 and frequencies larger than 0.5 cpd.

The organization of the tropical wave field is illustrated by the wavenumber-frequency spectra of the precipitation variance in TRMM and MPI-ESM shown in Figure 2.3. The spectra are computed as describer for Figure 2.2b, however, following Wheeler and Kiladis (1999), the precipitation is decomposed into symmetric and antisymmetric anomalies around the equator before applying the latitudinal average, so that $P(\phi)_{sym} = [P(\phi) + P(-\phi)]/2$ and $P(\phi)_{asym} = [P(\phi) - P(-\phi)]/2$, where P is the precipitation rate and ϕ is the latitude.

Figures 2.3a and d show the sum of the symmetric and antisymmetric wave spectra $P_{sym}(\omega, k) + P_{asym}(\omega, k)$ for TRMM and MPI-ESM, where ω is the frequency and k is the zonal wavenumber. As shown by Kim and Alexander (2013), the precipitation variance in TRMM is red in wavenumber and frequency and clearly organizes along phase speeds of -20 and +15 m/s (Fig. 2.3a). Also MPI-ESM shows this organization, but less pronounced than TRMM (Fig. 2.3d). At frequencies higher than 0.5 cpd, the TRMM spectrum has more spectral power at easterly than at westerly waves (negative and positive wavenumbers, respectively) while in MPI-ESM, the spectrals powers are more evenly distributed. At wavenumbers smaller than ±20 and frequencies lower than 0.2 cycles per day, the precipitation variance in MPI-ESM is larger than in TRMM. However, compared to TRMM, the variance in MPI-ESM decreases much more rapidly with higher wavenumbers and frequencies.

Figures 2.3b and e show the spectra of the symmetric precipitation variance in TRMM and MPI-ESM, respectively, and Figures 2.3 c and f show the antisymmetric spectra of both datasets. The contour lines indicate the symmetric and antisymmetric spectral power, while the shading indicates the ratio of the symmetric and antisymmetric spectra to a background spectra. The background spectrum is computed by adding the symmetric and antisymmetric wave spectrum and smoothing it with multiple 1-2-1 filters in wavenumber at each frequency (Wheeler and Kiladis, 1999). Ratios larger than 1.1 indicate organized convection (Wheeler and Kiladis, 1999). The dispersion lines of Matsuno-type equatorial waves (Matsuno, 1966), which are the preferred modes of variability in the tropics (Wheeler and Kiladis, 1999; Kiladis et al., 2009), are superimposed on the plots. In TRMM and MPI-ESM, the shapes of the symmetric and antisymmetric spectra do not differ much from the sum of both spectra (cf. Fig. 2.3a to b and c and Fig. 2.3d to e and f). However, in both datasets, the ratios of the symmetric and antisymmetric spectra to the background spectrum show clear signals of symmetric Kelvin waves and n1 gravity waves (Fig. 2.3b, e) and antisymmetric mixed Rossby gravity waves, n0 westerly waves and n2 gravity waves (Fig. 2.3c, f)

with equivalent depths between 10 and 90 m (the notation n0, n1 and n2 gravity waves refers to solutions for equatorial waves in Matsuno (1966) with the order n=0, n=1, and n=2). In TRMM, the ratios of Kelvin and MRG waves are slightly higher than in MPI-ESM, which demonstrates the higher grade of organization in TRMM.

2.5 The stratospheric wave field

2.5.1 Wavenumber-frequency spectra

The tropical precipitation discussed above excites vertically propagating waves which carry the zonal momentum necessary to force the QBO. In the following, the wavenumber-frequency spectra of temperature at various altitudes during the QBO westerly and easterly phase are discussed, as Ern and Preusse (2009b) and Yang et al. (2012) showed that waves filtered by the QBO jets loose spectral power with altitude and thus, identified the waves potentially contributing to the QBO forcing. It shall be put infront that the ground based frequency of a convectively triggered wave is mostly defined by the interplay of the tropospheric heating profile associated with the convective event and the background wind at the source level (see Fritts and Alexander, 2003, and references therein). Given slowly varying background winds in the stratosphere, the wave's ground based frequency does not change with altitude, and only the wave's

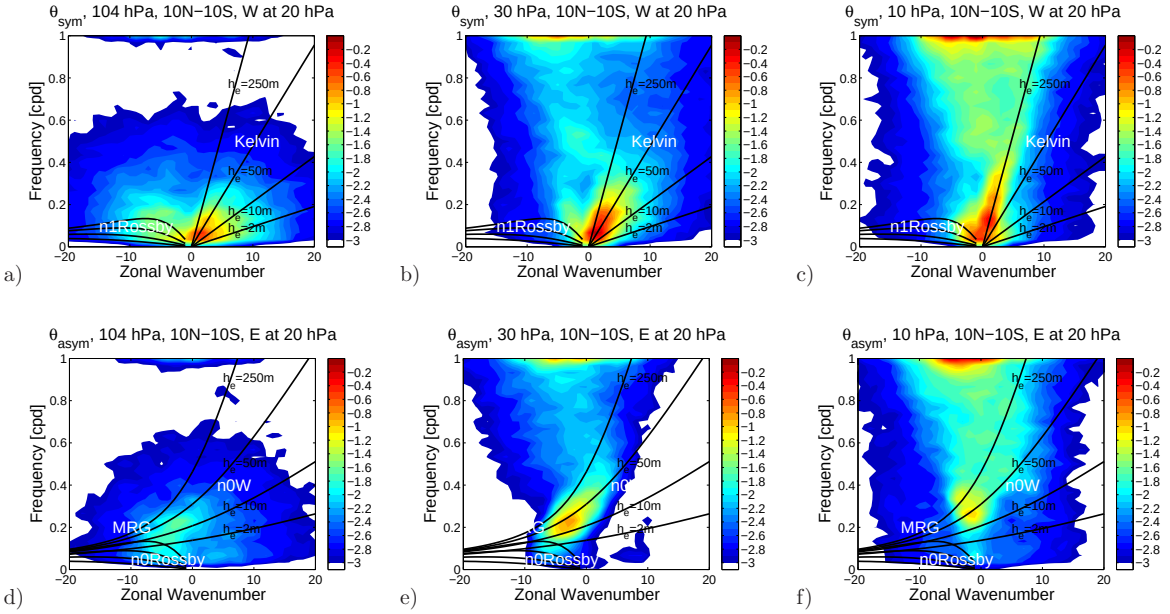

Figure 2.4: a) to c): Symmetric wavenumber-frequency spectra of the temperature variance in $\log(K^2)$ at 104, 30 and 10 hPa during the QBO westerly phase. The dispersion lines of Kelvin waves and n1 equatorial Rossby waves with equivalent depths of 2, 10, 50 and 250 m are superimposed on the plots. d) to f): same as a) to c), but for the antisymmetric waves during the QBO easterly phase and with the dispersion lines of n0 equatorial Rossby waves, mixed Rossby gravity waves and n0 westerly waves. Negative wavenumbers indicate easterly waves.

intrinsic phase speed, equivalent depth and vertical wavenumber are Doppler shifted. Hence, assuming linearity, the signal of a wave will remain at the same place in the ground based wavenumber-frequency spectra at every altitude.

Figures 2.4a to c show the symmetric wavenumber-frequency spectra at 104, 30 and 10 hPa averaged over the 14 months defined as QBO westerly phase during the first 30 years of the piControl run as described in section 2.3. Figures 2.4d to f show the antisymmetric spectrum at the same pressure levels averaged over the 14 months defined as the QBO easterly phase. Before applying the Fourier transform, the temperature perturbations have been decomposed into symmetric and antisymmetric parts as described in Section 2.4. Then, 14 individual spectra have been computed over the 14 individual months separately for each latitude using a time window of 30 days, and then averaged over the 14 spectra and from 10°N to 10°S. The input frequency of the data is 4 samples per day. Figure 2.4 also shows the dispersion lines of Matsuno-type equatorial waves (Matsuno, 1966) with equivalent depths of 2, 10, 50 and 250 m assuming zero background wind.

A direct downward influence of the wind field on the wave field is impossible in the tropical stratosphere (Plumb, 1977). Accordingly, despite the potential influence of the QBO on tropical convection (Giorgetta et al., 1999; Liess and Geller, 2012), the wavenumber-frequency spectra at 104 hPa, just above the convective wave sources and below the region influenced by the QBO, are qualitatively equal during the QBO westerly and easterly phase (not shown). Waves framed by the dispersion lines of Kelvin and equatorial Rossby waves dominate the symmetric spectrum (Fig. 2.4a). In the antisymmetric wave spectrum, mixed Rossby gravity waves (MRG waves) show the largest variance at easterly zonal wavenumbers, while there is relatively little power at westerly wavenumbers (Fig. 2.4d).

During the months defined as QBO westerly phase, the zonal wind below 20 hPa is easterly (see solid vertical lines in Fig. 2.1b) and thus, favourable for the propagation of westerly waves (Ern et al., 2008; Yang et al., 2011). However, comparing the wave spectra at 104 and 30 hPa in Figure 2.4a and b shows that Kelvin waves with ground based phase speeds slower than 10 m/s ($h_e < 10\,m$) are absorbed within the easterly flow in the lower stratosphere and thus, can not contribute to the QBO westerly jet's forcing. As shown by Ern et al. (2009a) and later in this paper, Kelvin waves are mostly radiatively damped, and the damping becomes more efficient with decreasing Doppler shifted phase speed. Apparently, the slow Kelvin waves are slow enough for efficient radiative wave damping even within easterly flow. Due to the decrease of density with altitude, the power of the remaining waves increases, especially at frequencies higher than 0.4 cpd. The QBO westerly jet, which starts at 20 hPa, strongly filters westerly waves. Thus, at 10 hPa, the symmetric spectrum lacks Kelvin waves with phase speeds slower than 20 m/s ($h_e < 50\,m$) and mostly shows Kelvin waves with phase speeds faster than 50 m/s ($h_e > 250\,m$, Fig. 2.4c). This illustrates that the westerly jet is forced by waves with phase speeds considerably faster than the jet itself.

During the QBO easterly phase, antisymmetric waves with frequencies larger than 0.1 cpd propagate to 30 hPa undisturbed (cf. Fig. 2.4d and e). At 30 hPa, just below the onset of the QBO easterly jet, MRG waves dominate the antisymmetric spectrum (Fig. 2.4e). Between 30 and 10 hPa, the QBO easterly jet strongly filters easterly

waves slower than 30 m/s (cf. Fig. 2.4e and f). However, a distinct peak of the spectral power displays the presence of very fast MRG waves with zonal wavenumbers lower than 5 and frequencies higher than 0.3 cpd. These waves are fast enough to propagate through the easterly jet into the middle and upper stratosphere. This is consistent with observations, which show that high speed Rossby gravity waves can even reach the mesopause region (Garcia and Lieberman, 2005; Ern et al., 2009b).

The discussion above omitted the antisymmetric and symmetric wave spectra, respectively, during the QBO westerly and easterly phase, respectively. The symmetric wave spectrum is dominated by westerly Kelvin waves, which are mostly filtered within the westerly flow below 20 hPa during the QBO easterly phase. Hence, during the QBO easterly phase, the symmetric wave spectrum at 30 hPa qualitatively resembles the symmetric wave spectrum at 10 hPa during the QBO westerly phase (not shown). Similarly, the MRG waves, which dominate the antisymmetric wave spectrum, are strongly filtered below 30 hPa during the QBO westerly phase, when the zonal wind below 20 hPa is easterly (not shown).

2.5.2 Vertical structure of Kelvin waves

Consistent with results presented by Ern and Preusse (2009b) and Yang et al. (2011), the loss of spectral power with altitude shown above illustrates the filtering of atmospheric waves by the QBO jets. In this section, the dynamical and physical processes leading to the observed wave attenuation are investigated. These wave dissipation processes depend on the wave induced gradients of temperature and wind and hence, the evolution of the waves' vertical wavelength (Fels, 1982). In the following, the connection between wave structure and wave damping is discussed based on Figure 2.5, which shows the time/height cross section of temperature perturbations induced by two sets of Kelvin waves. The focus lies on Kelvin waves as they are generally well developed in MPI-ESM (Fig. 2.4) and other models (Lott et al., 2013) and contribute most to the forcing of the QBO westerly jet (shown below). The waves have been isolated by first applying a fast Fourier transformation in longitude and time on the symmetric temperature field at every model level and at every latitude. The latitudinal and temporal means have been subtracted from the data prior to the spectral decomposition, but no detrending and no tapering has been applied. Then, only the spectral components at wavenumbers ranging from 1 to 5, frequencies ranging from 0 to 0.5 cycles per day and ground based phase speeds between 10 and 20 m/s (Fig. 2.5a, d) and between 20 and 50 m/s (Fig. 2.5b, e), respectively, have been transformed back to physical space by applying the inverse fast Fourier transform on the spectra at each pressure level and each latitude. The chosen range of phases speeds corresponds to the dispersion lines of Kelvin waves with equivalent depths of 10, 50 and 250 m, which dominate the stratospheric wave spectrum (Fig. 2.4a-c).

The cross sections in Figure 2.5a, b and d, e show two of the months defined as QBO westerly and easterly phase, respectively. The zero wind line between the upper and the lower-level QBO jets is indicated by a black horizontal line at 20 hPa. Though the reconstructed wave fields have particular characteristics depending on the month,

latitude and longitude which they are representative for, the qualitative results discussed next are robust with respect to these parameters. Figures 2.5c and f show the zonal wind profiles and the theoretical vertical wavelengths (2π/m) of Kelvin waves with ground bases phase speeds of 10, 20 and 50 m/s for zero background wind (dashed black lines) and including Doppler shift (solid gray lines) during the two months. The vertical wavenumber m of Kelvin waves relates to the intrinsic phase speed c-$\bar{u}$ and the equivalent depth h_e as

$$m = \frac{N}{c - \bar{u}} = \frac{N}{\sqrt{g\, h_e}} \tag{2.1}$$

were N is the buoyancy frequency.

The slow and fast sets of Kelvin waves (low and high equivalent depths) have vertical wavelengths of roughly 5 and 10 km, respectively, within the lower-level QBO easterly jet (Fig. 2.5a, b) and of 2 and 7.5 km, respectively, within the lower-level QBO westerly jet (Figure 2.5d,e). These values are in accordance with the Doppler shifted theoretical values (Fig. 2.5c, f).

During the QBO easterly phase, the slow Kelvin waves meet critical levels within the lower level QBO westerly jet, where their intrinsic phase speed $c - \bar{u}$ and hence, their vertical wave-lengths become zero (Fig. 2.5f). The waves do not propagate beyond that level (Fig. 2.5d), and as shown below, deposit westerly momentum. The same Doppler shift of the vertical wavelengths and the resulting dissipation of the slow Kelvin waves can be observed within the QBO westerly jet above 20 hPa in Figure 2.5a, c.

Due to the strong easterly winds between 50 and 30 hPa during the QBO westerly phase, Equation (2.1) predicts a Doppler shift of all selected waves to large vertical wavelengths (Fig. 2.5c). However, the layer is too shallow for the waves to adjust, and their vertical wavelength does not change as strongly as predicted (Fig. 2.5a, b). The QBO westerly and easterly jets above 20 hPa in Figures 2.5a, b and d, e, respectively, extend over a large vertical layer and the waves adjust their vertical wavelengths according to Equation (2.1).

When the fast Kelvin waves enter the strong QBO westerly jet above 20 hPa, their wavelengths halve from 10 to 5 km and the waves do not propagate beyond 10 hPa (Fig. 2.5b, c). However, during the QBO easterly phase, the fast Kelvin waves propagate through the weaker QBO westerly jet in the lower stratosphere, and their vertical wavelength increases from 10 to 20 km within the QBO easterly jet above 20 hPa (Fig. 2.5e, f). In the month selected to represent the QBO easterly phase, a westerly jet of the semiannual oscillation is located above 5 hPa (Fig. 2.5f). Here, the vertical wavelength of the fast Kelvin waves again decreases from 20 to 5 km, which is followed by the waves' dissipation (Fig. 2.5e, f).

2.5.3 Wave damping

The shortening of the Klevin waves' vertical wavelengths within westerly flow and the resulting increase of the waves' amplitudes facilitates longwave radiative heat loss

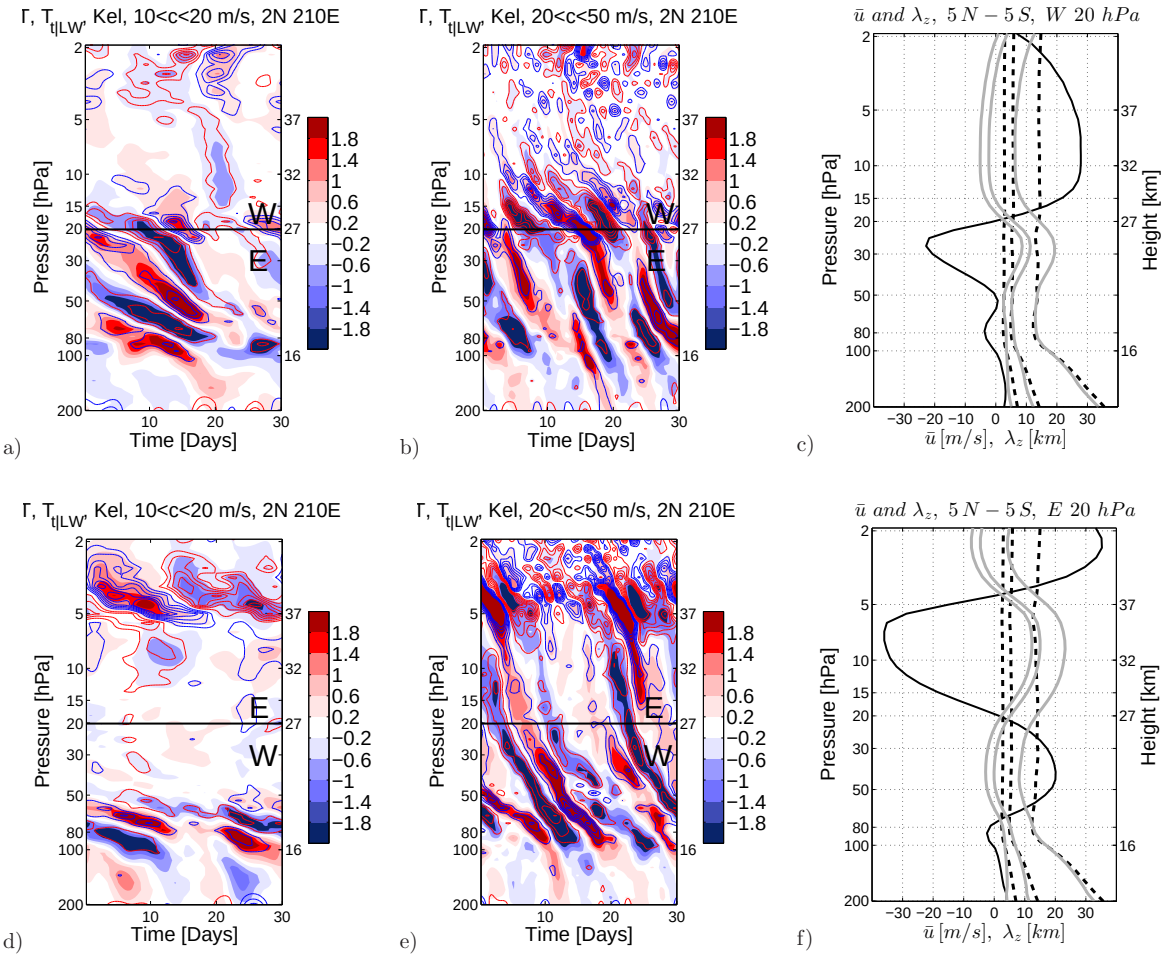

Figure 2.5: Temperature perturbation (K) induced by Kelvin waves (shading) with ground based phase speeds between 10 and 20 m/s (a, d) and between 20 and 50 m/s (b, e) during one month classified as the QBO westerly (a, b) and easterly (d, e) phase. The contour lines indicate the longwave radiative temperature tendencies associated with the Kelvin waves. The contour interval is 0.01 K/day. Positive and negative tendencies are drawn in red and blue, respectively. Panel c) and f) show the zonal mean zonal wind (m/s, solid black) and theoretical vertical wavelengths of Kelvin waves (km) with ground based phase speeds of 10, 20 and 50 m/s with and without Doppler shift (dashed black and gray, respectively) during the two months shown in panel a, b) and d, e).

(Fels, 1982; Zhu, 1993; Hitchcock et al., 2010), which is illustrated by the contour lines depicting the longwave radiative temperature tendencies associated with the isolated Kelvin waves in Figure 2.5. The tendencies have been isolated the same way as the wave induced temperature perturbations as described in section 2.5.2. The temperature and the temperature tendencies have the same vertical structure and are almost perfectly in phase (Fig. 2.5). Their average correlation coefficient between 100 and 10 hPa is -0.97. Within the QBO westerly jet, the waves' phase speed is Doppler shifted to lower values, which coincides with large radiative tendencies (Fig. 2.5a, b, d). Hence, an individual air parcel experiences the temperature perturbation and the anti correlated tendency for an increased amount of time, which enhances the radiative wave damping. Within the QBO westerly jet above 20 hPa in Figures 2.5a and b, the time an air parcel's

temperature is perturbed matches the radiative time scales and the shown Kelvin waves dissipate quickly. When the QBO westerly jet is in the lower stratosphere and relatively weak as in Figures 2.5d and e, the Doppler shifted phase speed of the slow Kelvin waves is low enough for them to dissipate below 30 hPa (Fig. 2.5d), whereas the still relatively large intrinsic phase speed of the fast Kelvin waves allows them to propagate beyond the westerly jet into the upper stratosphere (Fig. 2.5e).

Ern et al. (2009a) showed that Kelvin waves which are faster than the QBO westerly jet are mostly damped by longwave radiation. To estimate the contribution of radiative and diffusive processes to the wave damping in the GCM applied here, Figure 2.6 shows the amplitude spectrum (absolute value of the spectral coefficients) of temperature, the longwave radiative temperature tendencies, the zonal wind and the horizontal zonal wind diffusion at 20 hPa during the QBO westerly phase. The temperature spectrum shows Kelvin waves faster than 10 m/s, a mix of gravity waves with frequencies higher than 0.5 cpd and wavenumbers lower than 20, and atmospheric tides (Fig. 2.6a). At wavenumbers larger than 20, the temperature amplitudes vary little with frequency and decrease continuously with increasing wavenumber. The spectrum of the zonal wind amplitudes is qualitatively equal to the temperature spectrum (cf. Fig. 2.6a and d). Also the amplitudes of the longwave radiative tendency organize similar to the temperature spectrum (cf. Fig. 2.6a and b), which is to be expected as longwave radiation follows Planck's law and is a function of temperature.

Im MPI-ESM, horizontal diffusion does not involve a physical model of subgrid-scale processes but as in many models, is expressed in the form of an eight's order Laplacian, which is a numerically convenient form of scale selective diffusion with empirically determined coefficients to ensure a realistic behaviour of the resolved scales (Roeckner et al., 2003). The horizontal diffusion is zero at wavenumber 0 and increases with increasing zonal wind and wavenumber. At wavenumbers lower than $\pm$ 20 and frequencies lower than 0.5 cpd, the amplitudes of horizontal diffusion are strong (Fig. 2.6e) as at such scales, also the amplitudes of the zonal wind perturbations are strong (Fig. 2.6d). However, the spectrum of the horizontal diffusion does not organize in e.g. Kelvin waves (Fig. 2.6d). The dominant factor of the horizontal diffusion is the zonal wavenumber: for wavenumbers beyond $\pm$20 the horizontal diffusion increases sharply over all frequencies (Fig. 2.6d).

Figures 2.6c and f show the amplitude spectra of temperature and the zonal wind divided by the amplitude spectra of the longwave radiative temperature tendency and the diffusive zonal wind tendency, respectively. These e-folding timescales are first order approximations of the time longwave radiation and horizontal diffusion need to damp the wave induced temperature and zonal wind perturbations. The efficiency of a damping process increases with decreasing time scale.

Theoretical studies showed that the radiative damping is more efficient for waves with low vertical wavelengths (see Fels, 1982, and discussion therein). Accordingly, the radiative time scales in MPI-ESM vary little with zonal wavenumber and increases with increasing phase speed (Fig. 2.6c) and hence, with increasing vertical wavelength. The diffusive time scales, however, shorten with increasing wavenumber and vary little with frequency (Fig. 2.6f). For Kelvin waves with wavenumbers between 0 and 10 and frequencies lower than 0.5 cycles per day, the radiative time scales are shorter

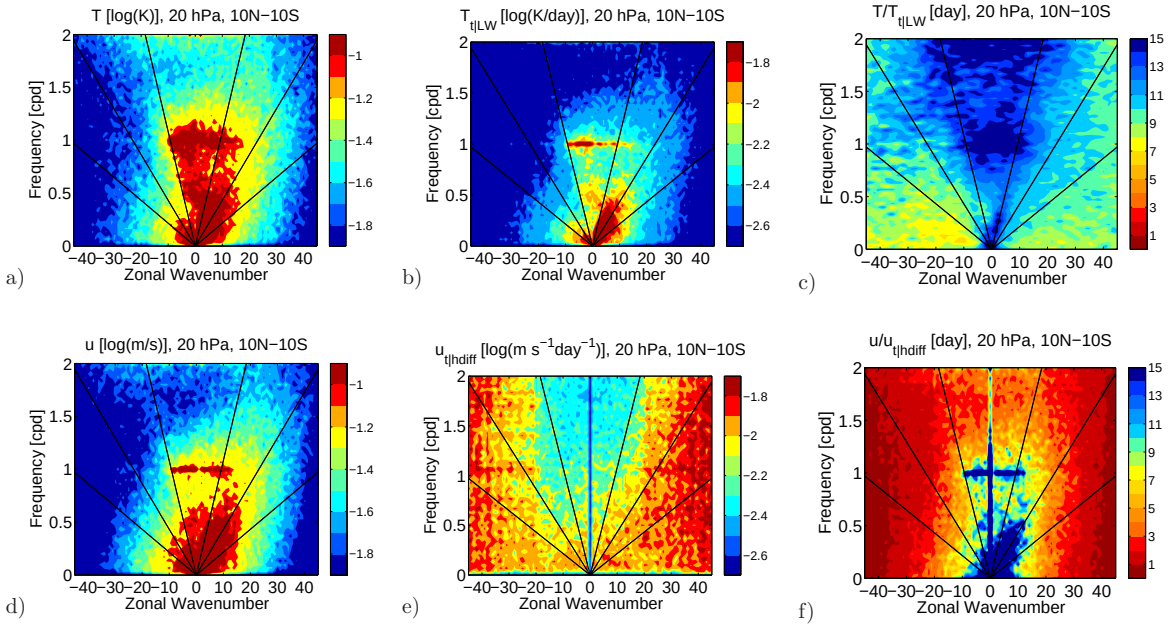

Figure 2.6: Latitudinal mean (10°N to 10°S) symmetric wavenumber-frequency spectra of the amplitudes of a) temperature in log(K), b) the longwave radiative temperature tendency in log(K day^{-1}), c) the e-folding time of the temperature perturbations due to longwave radiative damping (day) d) the zonal wind in log(m s^{-1}), e) the horizontal diffusion of the zonal wind in log(m s^{-1} day^{-1}) and f) the e-folding time of the zonal wind perturbation due to horizontal diffusion (day). All panels show the amplitudes at 20 hPa averaged over months defined as the QBO westerly phase. Note the different scales of the shading. Black lines indicate constant phase speeds of ± 10, 50 and 100 m/s. Negative wavenumbers indicate easterly waves.

than the diffusive time scales, (cf. Fig. 2.6c and f). Hence, longwave radiation is the dominant damping mechanism for these waves. However, with increasing wavenumber, the temperature and zonal wind perturbations decrease (Fig. 2.6a, d), whereas the horizontal wind diffusion increases (Fig. 2.6e). Thus, the diffusive time scales become shorter than the radiative time scales and hence, dominate the wave damping. So the choice of the numerical diffusion scheme, which is needed for the closure of the discretized dynamics, matters for the high wavenumber spectrum in general, and for wave mean flow interaction driving the QBO in particular.

Note that, in the Model, the numerical horizontal temperature diffusion and the numerical meridional and vertical diffusion of the dynamic variables are an order of magnitude weaker than the values just presented and hence, are not important for the wave damping in MPI-ESM.

2.6 Resolved wave forcing

The influence of the mean flow on the propagation of tropical waves has been shown above. Next, the actual forcing of the QBO easterly and westerly jets which results from the wave attenuation will be discussed based on the 209 quasi-biennial cycles

of the first 500 years of the piControl run. Such an analysis has been presented for high resolution models by Kawatani et al. (2010a) and Evan et al. (2012b), but is still missing for GCMs with a relatively course resolution comparable to MPI-ESM, which however, still form the majority of operational GCMs.

The stratospheric wave forcing is commonly described within the framework of the Transformed Eulerian Mean (TEM) equations (Andrews et al., 1987). Within this framework, the Eliassen-Palm flux F and its divergence $\nabla \cdot F$ are measures of the transport and deposition of zonal momentum and heat by atmospheric waves (Andrews et al., 1987). To distinguish the contribution of waves with different zonal wavenumbers, frequencies and phase speeds to the zonal wind tendency, the spectral distribution of the EP-flux is computed following Horinouchi et al. (2003):

$$\begin{aligned} \frac{F^{(\phi)}(k,\omega)}{\rho_0\, a\, cos\phi} &= real\,[\,\bar{u}_z \hat{v}(k,\omega)\hat{\theta}^*(k,\omega)/\bar{\theta}_z] - \\ &\quad real\,[\,\hat{u}(k,\omega)\hat{v}^*(k,\omega)] \end{aligned} \tag{2.2}$$

$$\begin{aligned} \frac{F^{(z)}(k,\omega)}{\rho_0\, a\, cos\phi} &= real\Big\{\Big[f - \frac{(\bar{u}\, cos\phi)_\phi}{a\, cos\phi}\Big]\,\hat{v}(k,\omega)\hat{\theta}^*(k,\omega)/\bar{\theta}_z\Big\} - \\ &\quad real\{\hat{u}(k,\omega)\hat{w}^*(k,\omega)\} \end{aligned} \tag{2.3}$$

In Equations (2.2) and (2.3), ρ_0 is the log-pressure height-dependent density, a is the Earth radius, ϕ and z are the latitude and the log-pressure height and f is the Coriolis parameter ($f \equiv 2\Omega\, sin\phi$ and Ω is the rotation rate of the Earth). u, v, w and θ are the zonal, meridional and vertical wind and the potential temperature. An overbar denotes the zonal mean of the variables, a hat above variables denotes their Fourier coefficients and an asterisk denotes the complex conjugate. The Fourier coefficients have been derived by applying a Fast Fourier Transform in longitude and time at each latitude for each of the 209 months defined as QBO westerly and easterly phase, respectively. u, v, w and θ have not been decomposed into symmetric and antisymmetric components, have not been detrended and have not been tapered before calculating the spectral EP-flux. The EP-flux and the EP-flux divergence for each individual month have been averaged over the individual spectra and from 10°N to 10°S. In Equations (2.2) and (2.3), subscripts ϕ, z and t denote the meridional, vertical and temporal derivatives. k and ω denote the zonal wavenumber and frequency. In this study, F denotes the EP-flux carried by waves resolved in MPI-ESM-MR with global wavenumbers k ranging from 0 to 63.

2.6.1 Spectral distribution of vertical EP-flux

The wavenumber-frequency spectrum of the vertical EP-flux at 104 hPa, below the region influenced by the QBO, is shown in Figure 2.7a. Except for the diurnal peak, the spectrum is red in wavenumber and frequency and continuous over the whole spectral

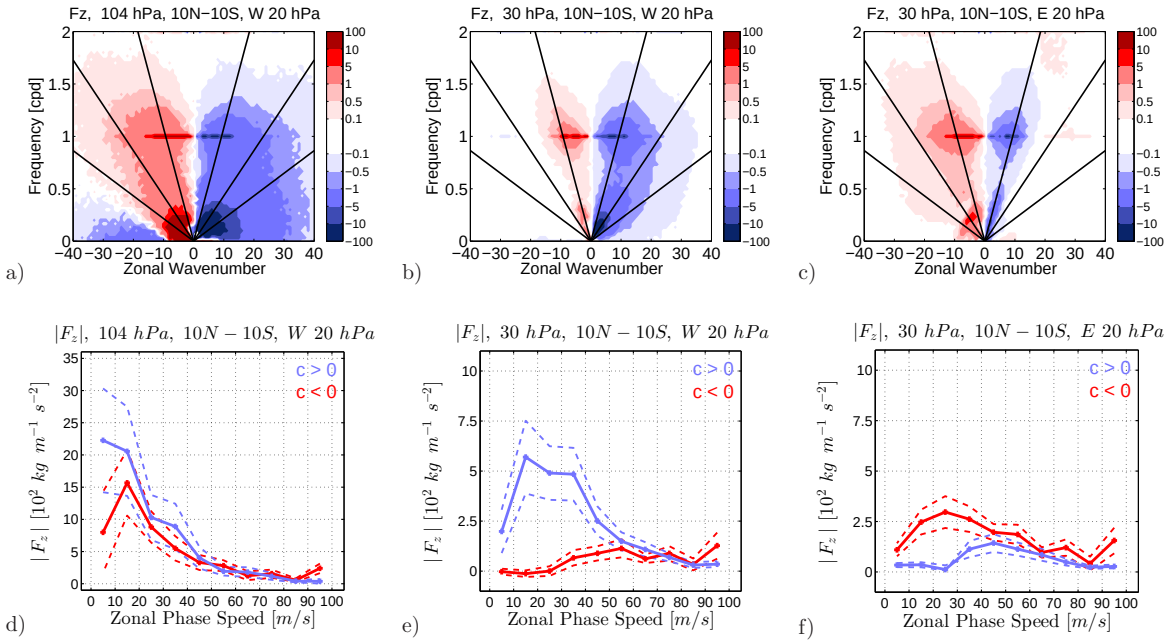

Figure 2.7: Latitudinal mean (10°N to 10°S) zonal wavenumber-frequency spectra of the vertical EP-flux (kg m^{-1} s^{-2}) at 104 and 30 hPa (a, b) during the QBO westerly phase and at 30 hPa during the QBO easterly phase (c). The black lines indicate constant phase speeds of ± 10, 50 and 100 m/s. Negative wavenumbers indicate easterly waves. Panels d-f show the EP-flux shown in panel a to c for easterly (red) and westerly (blue) waves integrated over discrete pairs of wavenumbers and frequencies which correspond to 10 m/s bins of constant phase speeds. Thin dashed lines indicate the standard deviations within the 209 EP-flux spectra for each phase speed bin.

range. The EP-flux is largest at wavenumbers lower than 20 and frequencies lower than 0.5 cpd, where the spectrum shows an asymmetry such that the decrease of the momentum flux with wavenumber is less pronounced at positive (westerly) than negative (easterly) wavenumbers. This is associated with a reversal of the sign of the EP-flux at wavenumbers lower than -10, probably due to the Doppler shift of very slow Kelvin waves (Ortland and Alexander, 2011). The EP-flux stays almost constant at frequencies ranging from 0.5 to 1 cpd. Peaks at 1 cpd are due to atmospheric tides. At frequencies higher than 1 cpd, the momentum flux decreases quickly. In Figure 2.2b it has been shown that compared to TRMM, MPI-ESM underestimates the variability of precipitation with wavenumbers higher than 20 and periods shorter than 5 days. Though in general, convectively triggered waves are strongly filtered in the uppermost troposphere and thus, the stratospheric wave spectrum is not expected to completely match the spectrum in the troposphere (Lott et al., 2013), the shortage of precipitation variability at high wavenumbers and frequencies in MPI-ESM indicates that MPI-ESM will underestimate the EP-flux at these frequencies and wave numbers also in the stratosphere.

Figure 2.4 showed that equatorial waves are filtered depending on their zonal phase speed rather than their wavenumber or frequency. Hence, the distribution of the wave momentum among zonal phase speeds contains information about the potential forcing of the QBO jets. Figure 2.7d shows the EP-flux at 104 hPa integrated over discrete pairs

of wavenumbers and frequencies which correspond to 10 m/s bins of constant phase speeds. The EP-flux carried by westerly waves (blue line in Fig. 2.7d) is largest at phase speeds between 0 and 10 m/s. For easterly waves (red line in Fig. 2.7d) the maximum is shifted to higher phase speeds between - 10 and -20 m/s. The wave momentum flux decreases continuously with increasing phase speed, and waves faster than ± 40 m/s carry less than 10 % of the total EP-flux. Easterly waves carry less momentum than westerly waves, especially at low phase speeds. As in MPI-ESM, the variance of tropical precipitation and hence, the convective wave source, is balanced between easterly and westerly waves (Fig. 2.2b), the imbalance of the wave momentum flux at 104 hPa indicates stronger filtering of easterly waves in the uppermost troposphere.

The dashed lines in Figure 2.7d indicate the standard deviations within the 209 binned EP-flux spectra for each phase speed bin. The standard deviations reach 30 % of the mean values. This variability is partly seasonal and contributes to the stalling of the QBO easterly jet in the lower stratosphere and together with parametrized waves and advection, modulates the downward propagation rate of the QBO jets (Krismer et al., 2013).

Figures 2.7b, e and c, f show the wavenumber-frequency spectra and the phase speed distribution of the vertical EP-flux at 30 hPa during the QBO westerly and easterly phase, respectively. The EP-flux carried by waves propagating into the direction of the man flow below 20 hPa (easterly waves in Fig. 2.7b, e and westerly waves in Fig. 2.7c, f) is strongly reduced. However, also the flux carried by waves with phase speeds opposite to the mean flow decreases (westerly waves in Fig. 2.7b, e and easterly waves in Fig. 2.7c, f), most strongly at low phase speeds. Once more, this illustrates the weakening of waves due to radiation and diffusion, even in the absence of critical levels.

2.6.2 Change of EP-flux with altitude

The connection between the background wind field and the phasespeed distribution of the wave momentum flux and the wave forcing is displayed in Figures 2.8a and b, which show profiles of the vertical EP-flux as a function of the ground based zonal phase speed averaged over the months defined as QBO westerly and easterly phase. To emphasize the change of the wave momentum flux with altitude rather than with phase speed, the flux in every phase speed bin has been normalized by its value at 104 hPa. Figures 2.8c and d show the profiles of the zonal wind tendency due to the total EP-flux divergence ($\nabla \cdot [\mathrm{F}_y, \mathrm{F}_z]$), also as a function of the zonal phase speed. The zonal wind profiles during the two QBO phases are superimposed on the plots.

During both phases, the vertical EP-flux carried by waves slower than ± 20 m/s strongly decreases in the lowermost stratosphere between 100 and 80 hPa (Fig. 2.8a, b), where the zonal wind is weak and there are no well defined QBO jets. This leads to pronounced easterly and westerly momentum deposition (Fig. 2.8c and d) and little net acceleration of the mean flow. During the QBO westerly phase, the winds are weak up to 50 hPa (Figure 2.8a, c) and longwave radiative damping of the slow westerly waves strongly reduces the wave momentum available to force the QBO westerly jet at higher altitudes. A comparison of the vertical EP-flux at 104 hPa and below the

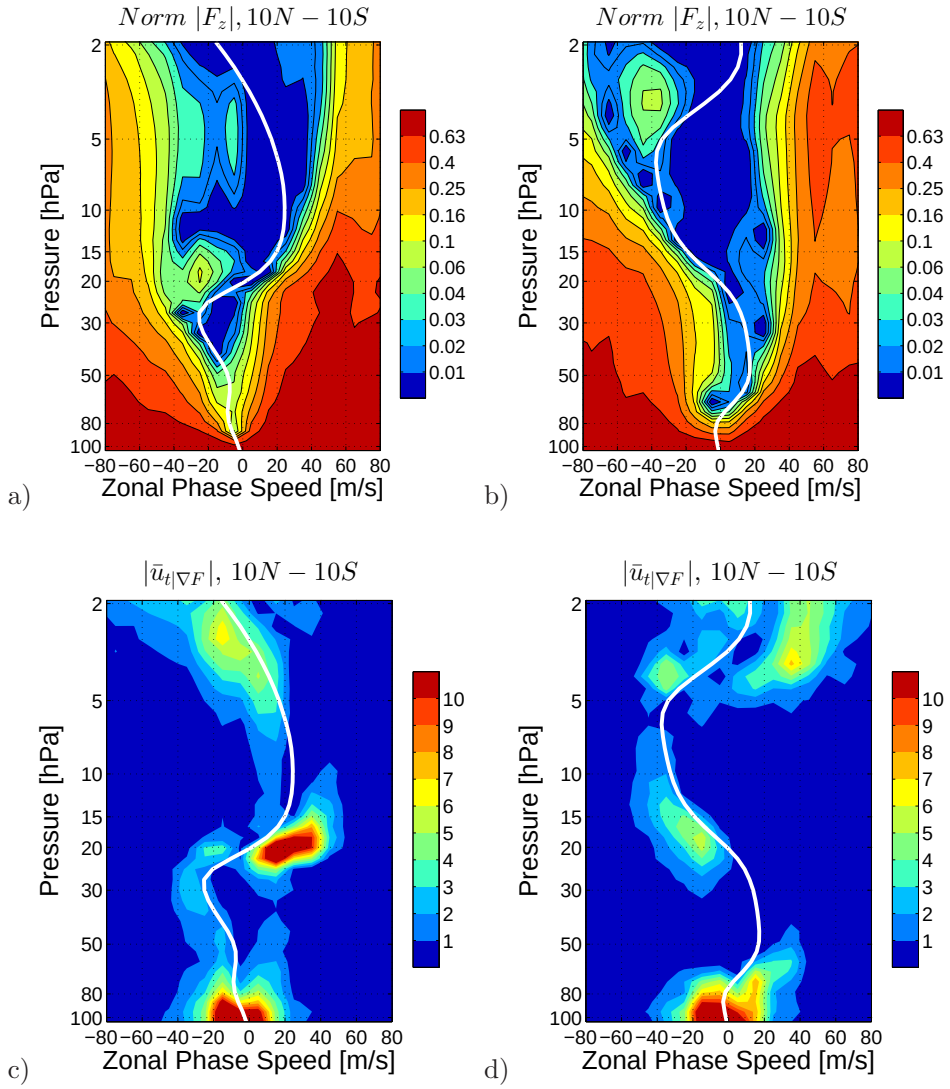

Figure 2.8: Profiles of the latitudinal mean (10°N to 10°S) vertical EP-flux (a, b) normalized by the values at 100 hPa and the zonal acceleration due to the EP-flux divergence in cm s^{-1} day^{-1} (c, d) during the QBO westerly (a, c) and easterly (b, d) phase as a function of the zonal phase speed. The white line represents the zonal mean zonal wind in m s^{-1}.

QBO westerly jet at 30 hPa in Figure 2.7d and e demonstrates that westerly waves with phase speeds between 10 and 20 m/s and between 20 and 50 m/s deposit about 75% and 50% respectively, of the vertical EP-flux within the lower level QBO easterly jet, which strongly reduces the wave momentum available to force the QBO westerly jet at higher altitudes.

In regions where the QBO jets are well developed - like the westerly jet above 20 hPa in Figure 2.8a and between 70 and 20 hPa in Figure 2.8b and the easterly jet above 20 hPa in Figure 2.8b - waves with phase speeds opposite to the direction of the mean flow propagate upwards without much loss of vertical EP-flux. Waves propagating in the direction of the zonal wind - like westerly waves above 20 hPa in Figure 2.8a or below 20 hPa in Figure 2.8b and easterly waves above 20 hPa in Figure 2.8b - lose momentum to the flow. The tilt of the contour lines towards higher phase speeds

indicates that with the strengthening of the QBO jets at higher altitudes, ever faster waves deposit wave momentum as their intrinsic phase speeds decrease and radiative wave damping becomes more efficient. Where waves meet critical levels where c-$\bar{u}$ =0, the wave momentum flux reduces to less than 1% of its reference value at 100 hPa.

When located in the lower stratosphere, the QBO westerly jet is mostly forced by waves with phase speeds between 0 and 10 m/s (Fig. 2.8d). As just described, these waves do not propagate high enough to reach the QBO westerly jet if located at 20 hPa, where the forcing of the westerly jet is mostly due to waves with phase speeds between 10 and 40 m/s (Fig. 2.8c). This means that waves almost twice as fast as the QBO jet still contribute to its forcing. Due to longwave radiative damping, the forcing of the QBO westerly jet can focus within a narrow layer between 30 and 15 hPa (Fig. 2.8c), even though most of the waves are still faster than the westerly jet and do not meet critical levels. Above 5 hPa, waves with phase speeds between 30 and 60 m/s force the westerly shear zone associated with the semiannual oscillation (Fig. 2.8d), which, on average, is located around 2 hPa in the 209 months defined as QBO easterly phase.

During the QBO easterly phase, the wave forcing of the easterly jet is weaker than the wave forcing of the westerly jet during the QBO westerly phase (cf. Figure 2.8c, d). Integrated from 30 to 10 hPa, the difference amounts to 30% of the westerly wave forcing (not shown), which is about the same as the difference between the easterly and westerly wave momentum reaching 30 hPa (cf. Fig. 2.7d, f).

Figure 2.9 shows the distribution of the wave forcing ($\nabla\cdot[F_y, F_z]$) among bins of 10 zonal wavenumbers during the QBO westerly and easterly phase, integrated over frequencies ranging from 0 to 0.5 cpd and from 0.5 to 2 cpd as a function the zonal wavenumber and integrated from 30 to 10 hPa to include all levels with considerable wave forcing during the respective QBO phases. Westerly waves ($k > 0$) with frequencies lower than 0.5 cpd (black line in Fig. 2.9a) and zonal wavenumbers lower than 10 (the spectral range of Kelvin waves) contribute most to the forcing of the QBO westerly jet (Fig. 2.9a). At wavenumbers between +10 and +30, the largest contribution to the QBO westerly jet's forcing comes from waves with frequencies between 0.5 and 2 cpd (gray line in Fig. 2.9a). The easterly waves' tendencies in Figure 2.9a are partly due to the inclusion of the forcing around the core of the QBO easterly jet at 30 hPa in the vertical integral from 30 to 10 hPa. Partly, the forcing is due to the build up of downward vertical EP-flux around the zero wind line at 20 hPa (Fig. 2.8a), which draws momentum from the flow. The origin of this peak is still investigated, but could be due to waves with easterly phase speeds with respect to the ground, but westerly intrinsic phase speeds at their level of origin. Such waves have negative vertical EP-flux and could become dominant after the bulk of easterly waves with also easterly intrinsic phase speeds has been filtered by the QBO easterly jet in the lower stratosphere. The masking of such waves is possible due to the zonally uniform representation of the EP-flux which, however, can be zonally highly variable (Kawatani et al., 2010b).

The forcing of the QBO easterly jet is distributed more evenly among frequencies, even at low wavenumbers, and there is no cancelling effect of westerly waves on the easterly forcing (Fig. 2.9b). The relative importance of easterly waves with high frequencies increases rapidly with wavenumber.

Based on model studies, Kawatani et al. (2010a) and Evan et al. (2012b) showed

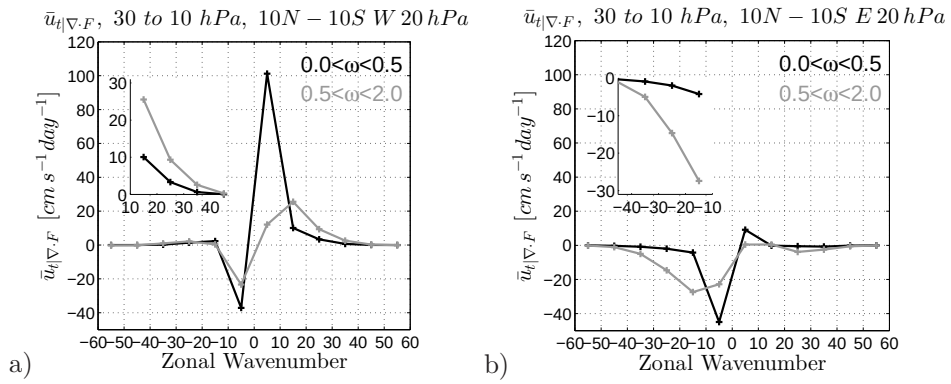

Figure 2.9: Latitudinal mean (10°N to 10°S) zonal wind tendency due to the divergence of the EP-flux integrated from 30 to 10 hPa (m s^{-1} day^{-1}) during the QBO westerly (a) and easterly (b) phase. The tendency has been integrated over frequencies ranging from 0 to 0.5 cpd (black), 0.5 to 1 cpd (dark gray) and 1 to 2 cpd (light gray). The small boxes show closeups of the zonal wind tendency at the respective wavenumbers. Negative wavenumbers indicate easterly waves.

that waves with zonal wavenumbers between 40 and 200 contribute about 60 and 80 % to the total forcing of the QBO westerly and easterly jet, respectively. Based on observations, also Ern et al. (2009a) showed that small scale waves have to account for 60 % of the wave forcing of the QBO easterly jet. Figure 2.8 clearly demonstrates that in a GCM truncated at T63, the contribution of small scale waves becomes negligible at wavenumbers larger than 40. To account for the missing resolved wave drag, most GCMs parametrize the propagation and dissipation of smaller scale waves.

2.6.3 Latitudinal structure of resolved wave forcing

QBO dynamics are mostly studied based on latitudinal and zonal means. However, Kawatani et al. (2010b) showed that there are substantial variations of wave activity and wave forcing in both longitude and latitude. The latitudinal structure of the QBO forcing is also displayed in Figure 2.10, which shows the latitude/height cross section of the zonal wind and the zonal wind tendency due to the divergence of the EP-flux carried by resolved waves during the QBO westerly and easterly phase (Fig. 2.10a to c and d to f, respectively). The forcing has been integrated over equatorial westerly waves with wavenumbers lower than 10 and frequencies lower than 0.5 cpd (Fig. 2.10a, d), over westerly gravity waves with wavenumbers lower than 10 and frequencies larger than 0.5 and with wavenumbers larger than 10 (Fig. 2.10b, e), and over all easterly waves (Fig. 2.10c, f). The latitudinal structures of the wind field and the forcing strongly depend on the season, and only months when the respective QBO phase occurs in June, July or August (JJA) have been sampled. This criterion leaves 67 and 46 individual months for the QBO westerly and easterly phase, respectively. In December, January and February, the latitudinal structure of the wind field and the forcing is mirrored with respect to the equator (not shown).

Consistent with the structure of Kelvin waves, which have a single maximum at the equator which decays towards the poles, the forcing of the QBO westerly jet due to

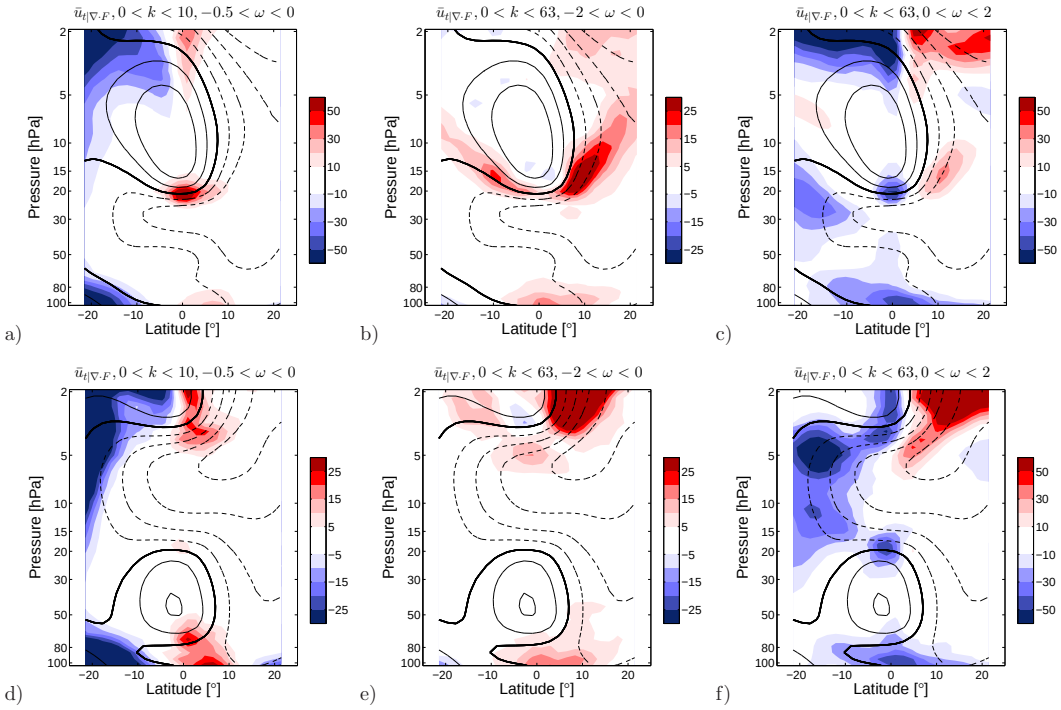

Figure 2.10: Latitude-height cross section of the zonal mean zonal wind in m s^{-1} (contours) and the resolved wave forcing in cm s^{-1} day^{-1} (shading) in months when the QBO westerly (a to c) and easterly (d to f) phase occurs in June, July or August. The contour interval is 10 m s^{-1}. Westerly (easterly) winds are drawn in solid (dashed) lines. The thick black contour indicates the zero wind line. The wave forcing has been integrated over equatorial westerly waves with wavenumbers lower than 10 and frequencies lower than 0.5 cpd (a, d), over westerly gravity waves with wavenumbers lower than 10 and frequencies larger than 0.5 cpd and with wavenumbers larger than 10 (b, e), and over all easterly waves (c, f).

equatorial westerly waves concentrates in a narrow band from 10°N to 10°S (Fig. 2.10a, d). The forcing due to westerly gravity waves is strongest away from the equator at the flanks of the QBO westerly jet, which is again consistent with the latitudinal structure of the gravity waves. Opposite to Kelvin waves, these have node 0, 2 or 4 structures with at least one relative minimum of the wave induced perturbations at the equator and maximal wave induced perturbations at higher latitudes (Matsuno, 1966; Kiladis et al., 2009). The westerly gravity wave's forcing is stronger in the summer hemisphere (Fig. 2.10b, e). This can be explained by stronger convective activity in the summer hemisphere and hence, stronger excitation of gravity waves (not shown) and the circumstance that the zonal wind in the summer hemisphere is easterly above 500 hPa, which facilitates the propagation of westerly waves (Fig. 2.10).

Easterly waves impose a westerly forcing along the flank of the westerly jet in the summer hemisphere (Fig. 2.10c), mostly due to the divergence of the horizontal momentum flux (not shown) and thus, to the meridional propagation of the easterly waves. During the QBO easterly phase, easterly waves force the easterly jet at its lowermost edge close to the equator (Fig. 2.10f) and, much stronger, over the whole depth of the easterly jet in the winter hemisphere. As the convective wave sources are weaker in the winter than in the summer hemisphere (not shown), this subtropical maximum has to be due

to the enhanced excitation of easterly waves which propagate equatorwards and the circumstance that zonal wind between 10° S and 20° S is westerly from 500 to 50 hPa in the selected season, which facilitates the propagation of easterly waves.

2.6.4 Resolved wave forcing during a quasi-biennial cycle

To investigate the dependence of the resolved wave forcing on the altitude of the QBO jets, a series of composites including only months when the zonal wind turns from easterly to westerly, such as presented for the phase transition at 20 hPa in Figure 2.8c, have been computed for every of the 28 model levels between 5 and 80 hPa. The occurrence of the phase transition is the only sampling criterion. In Figure 2.11, which shows the mean zonal wind, the vertical EP-flux (Fig. 2.11a to c) and the resolved wave forcing (Fig. 2.11d to f) for all these composites, the composites are sorted in such a way as to start and end with the onset of the QBO westerly jet at 5 and 80 hPa, respectively, which thus, creates the impression of a continuous QBO westerly jet descending from the upper to the lower stratosphere. The x-axis indicates the average time the QBO westerly jet needs to descend from 5 hPa to the respective level. As for Figure 2.10, EP-flux and the zonal acceleration due to resolved waves has been integrated over equatorial westerly waves with wavenumbers lower than 10 and frequencies lower than

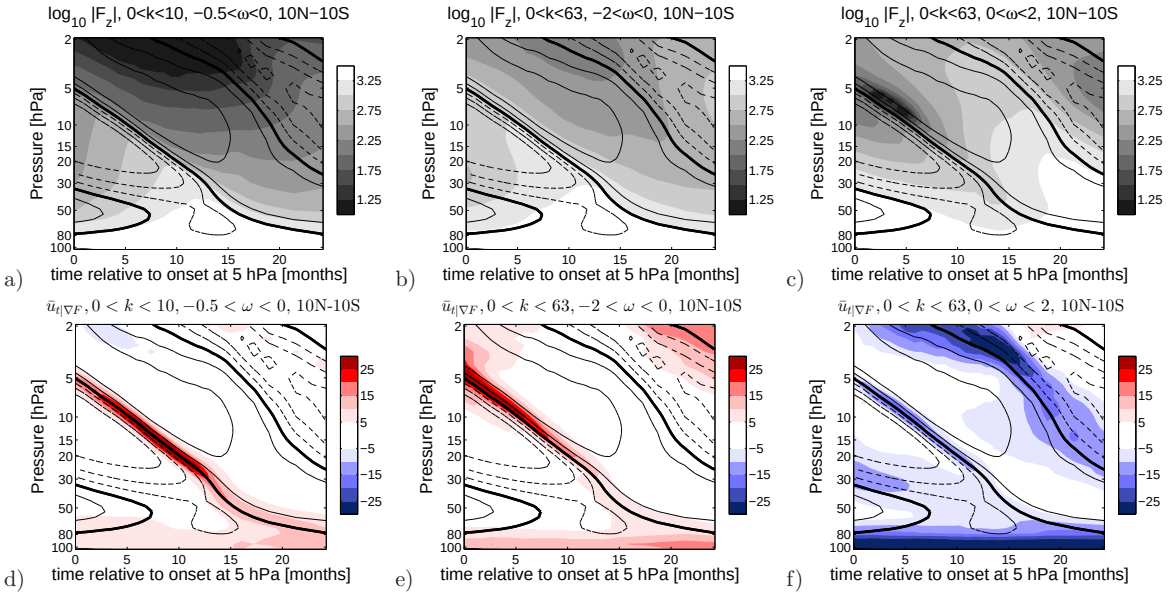

Figure 2.11: Altitude-time cross section of the zonal mean zonal wind in m s^{-1} (contours), the vertical EP-flux in $\log_{10}$(kg m^{-1} s^{-2}) (shading in a to c) and the resolved wave forcing in cm s^{-1} day^{-1} (shading in d to f). Each month is representative for a composite including all months when the onset of the QBO westerly jet is located at the respective level between 5 and 100 hPa. The contour interval is 10 m s^{-1}. Westerly (easterly) winds are drawn in solid (dashed) lines. The thick black contour indicates the zero wind line. The EP-flux and the wave forcing have been integrated over equatorial westerly waves with wavenumbers lower than 10 and frequencies lower than 0.5 cpd (a, d), over westerly gravity waves with wavenumbers lower than 10 and frequencies larger than 0.5 cpd and with wavenumbers larger than 10 (b, e), and over all easterly waves (c, f).

0.5 cpd (Fig. 2.11a), over westerly gravity waves with wavenumbers lower than 10 and frequencies larger than 0.5 cpd and with wavenumbers larger than 10 (Fig. 2.11b), and over all easterly waves (Fig. 2.11c).

Figures 2.11a and b show that - due to the continuous radiative attenuation - the vertical EP-flux carried by westerly waves decreases continuously with increasing distance between the tropopause and the zero wind line associated with the onset of the QBO westerly jet. This becomes especially obvious between month 7 and 15, when the zonal wind is easterly between 100 and 30 hPa, and hence, does not provide critical levels for westerly waves. Within this easterly flow, the EP-flux carried by easterly waves decreases continuously with height (Fig. 2.11c). However, within the QBO westerly jet, the EP-flux carried by easterly waves stays relatively constant (e.g. month 15 to 25 in Fig. 2.11c).

Figure 2.11d shows that, averaged from 10° N to 10° S, the forcing due equatorial westerly waves is strongest if the onset (lower boundary) of the QBO westerly jet is located between 30 and 10 hPa. If the onset of the QBO westerly jet is located at higher altitudes, the equatorial waves are partly filtered by the QBO westerly jet of the previous quasi-biennial cycle still present in the lower stratosphere. If the onset of the QBO westerly jet is located below 30 hPa, the westerly jet is weaker than at higher altitudes, and thus, less waves are Doppler shifted to intrinsic phase speeds and vertical wavelengths suitable for efficient wave dissipation. Further, the values in Figure 2.11 are not density corrected. Hence, the same amount of wave momentum deposition results in stronger zonal acceleration at high altitudes with relatively low air densities.

The westerly gravity waves with frequencies higher than 0.5 cpd and wavenumbers lower than 10, which are included in the forcing shown in Figure 2.11e, are generally very fast and thus, less affected by the lower level QBO westerly than equatorial waves with slower phase speed. As the wave filtering at low altitudes is less pronounced, the forcing due to westerly gravity waves increases with increasing altitude of the onset of the QBO westerly jet due do the decrease of density with altitude (Fig. 2.11e).

Above 80 hPa, the forcing due to westerly waves is limited to a narrow vertical band around the onset of the QBO westerly jet (Fig. 2.11d, e). Easterly waves, however, deposit easterly wave momentum at the zero wind line associated with the onset of both the QBO easterly and westerly jet (Fig. 2.11f). The forcing increases with altitude, probably due to the decrease of density with height and, in part, latitudinal propagation of extra tropical large scale easterly waves.

Note that due to the decrease of density with altitude, the zonal wind tendency (unit 10^{-2} m s^{-1}) can increase with increasing altitude of the zero wind line (Fig. 2.11d-f), even though the EP-flux decreases due to wave filtering below (Fig. 2.11a-c). However, due to this wave filtering, the actual momentum tendency due to wave dissipation (unit kg m^{-2} s^{-1} strongly decreases with altitude (not show).

2.7 The Zonal Momentum Balance

The zonal wind tendency equation does not only include resolved wave drag. Following Andrews et al. (1987), the Transformed Eulerian Mean (TEM) momentum equation

states:

$$\begin{aligned} \bar{u}_t &= \bar{v}^* \left[f - (a\,cos\phi)^{-1} (\bar{u}\,cos\phi)_\phi \right] - \bar{w}^* \bar{u}_z + \\ & \quad (\rho_0\, a\, cos\phi)^{-1} \nabla \cdot F + \bar{u}_{t|GWD} \end{aligned} \tag{2.4}$$

where $\bar{v}^*$ and $\bar{w}^*$ are the meridional and vertical residual mean winds and $\bar{u}_{t|GWD}$ represents the parametrized gravity wave drag. The gravity wave drag has only been stored during the first 30 years of the MPI-ESM piControl run, and the results presented next are based on this period. However, the averages of the resolved wave drag and the advective terms do not change significantly if computed over the first 500 years of the piControl run.

Figure 2.12 shows profiles of the zonal wind and the terms of the momentum balance for the QBO westerly and easterly phase. To make the results comparable to Giorgetta et al. (2006), the values are latitudinally averaged from 5°N to 5°S. The total zonal acceleration at the zero wind line associated with the onset of the QBO westerly jet at 20 hPa amounts to 0.6 m/s (gray line in Figure 2.12a). Within the narrow layer where longwave radiative damping results in pronounced resolved wave momentum deposition, the resolved and the parametrized wave forcing (green and orange line in Fig. 2.12a, respectively) are about equally strong (0.4 m/s). However, the parametrized waves mainly give momentum to the flow where the zonal phase speed closely matches the background zonal wind. Hence, the parametrized wave forcing extends further into the QBO westerly jet, where faster waves meet critical levels. Above the zero wind line, this parametrized acceleration mostly strengthens the QBO jet and and thus, contributes to the QBO's amplitude rather than its downward propagation rate. The vertical advection around the zero wind line is positive and amounts to about one quarter of the total wave forcing (dark blue line in Fig. 2.12a).

Figure 2.12c shows the profiles of the tropical and equatorial vertical velocity (averaged from 20°N to 20°S and from 5°N to 5°S, respectively) for the QBO westerly phase. From 80 to 15 hPa, the tropical vertical upwelling (solid gray line) amounts to 0.20 mm/s. The secondary circulation induced by the QBO westerly jet, which is directed downwards in the equatorial area, strongly reduces the vertical velocity and turns the equatorial vertical motion (dashed gray line) at 20 hPa downwards. Hence, the QBO westerly jet advects itself to lower altitudes.

The total zonal acceleration at the zero wind line associated with the onset of the QBO easterly jet at 20 hPa amounts to 0.3 m/s (Fig. 2.12b). The forcing from parametrized waves is about twice that of the resolved waves. Compared to parametrized westerly waves, parametrized easterly waves are less filtered between the source level at 700 hPa and the lowermost stratosphere (not shown) in MPI-ESM, which has also been reported by Kim et al. (2013) for another GCM. Hence, compared to the QBO westerly jet, the parametrized wave forcing is almost two times larger at the onset of the QBO easterly jet (cf. orange lines in Fig. 2.12a and b). The QBO easterly jet strengthens the upward motion in the equatorial area and, due to its larger latitudinal extent, also over the whole tropics (Fig. 2.12d). Between 30 and 15 hPa, the average tropical and equatorial vertical velocities amount to 0.3 and 0.5 mm/s, respectively. Hence, the

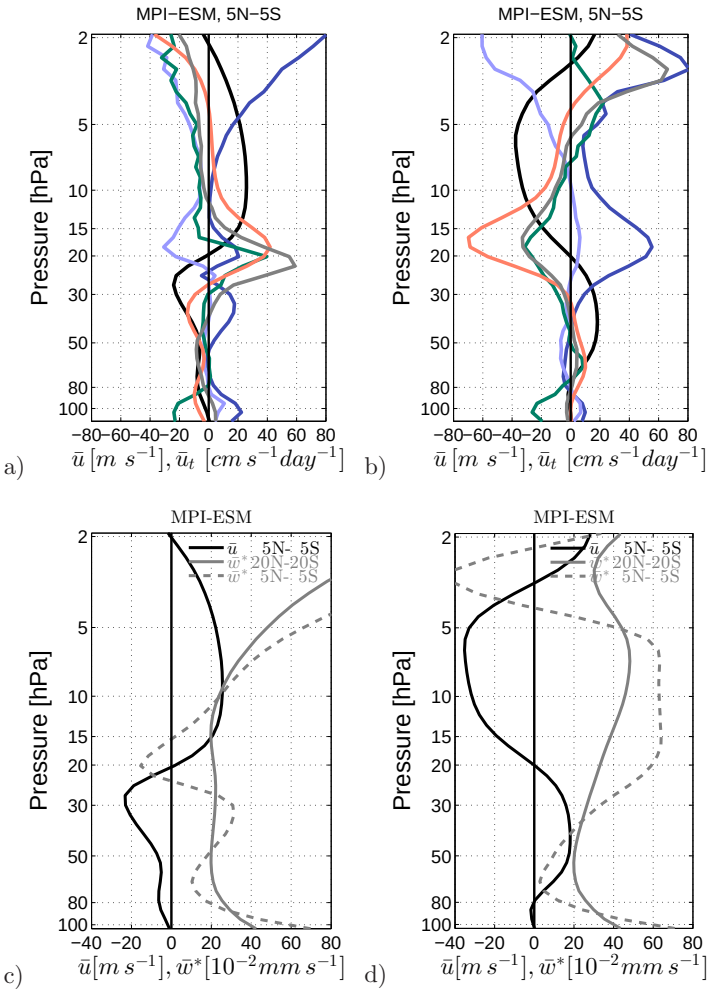

Figure 2.12: Latitudinal mean (5°N to 5°S) profile of the zonal wind (m/s, black), the zonal wind tendency (gray) and the zonal wind tendency due to resolved waves (green), parametrized waves (orange), vertical advection (dark blue) and horizontal advection (light blue) during the QBO westerly (a) and easterly (b) phase in cm s^{-1} day^{-1}. Panel c) and d) show the latitudinal mean profile of the zonal wind (m/s, 5°N to 5°S, black) and the residual vertical motion averaged from 20°N to 20°S (10^{-2}mm s^{-1}, solid gray) and from 5°N to 5°S (10^{-2}mm s^{-1}, dashed gray) during the QBO westerly (c) and easterly (d) phase.

vertical advection at the onset of the QBO easterly jet is largely positive and works against its downward propagation (Figure 2.12d).

A zonal momentum balance for the two QBO phases shown in Figure 2.12 has been presented by Giorgetta et al. (2006) based on the global atmosphere model MAECHAM5 truncated at T42 (their Figure 10) and by Evan et al. (2012b) based on the WRF tropical channel model with a resolution of 37 km (their Figure 10). Compared to Giorgetta et al. (2006), the wave forcing at the zero wind line (resolved + parametrized waves) is about 60% stronger in MPI-ESM than in MAECHAM5 (0.8 compared to 0.5 m $s^{-1}day^{-1}$) during the QBO westerly phase. This has multiple reasons. First, the source strength of the Hines gravity wave scheme is stronger in MPI-ESM, which strengthens the parametrized wave forcing. Second, MPI-ESM has a larger spectral truncation and resolves slightly more waves which contribute to the resolved wave forc-

ing. Third, the QBO jets are 10 m/s stronger in MPI-ESM than in Giorgetta et al. (2006). Hence, a larger spectrum of waves and in particular of parametrized waves, meets critical levels and contributes to the forcing. However, the slightly larger total acceleration at the zero wind line in MPI-ESM causes the jets to descend more quickly than in MAECHAM5 (not shown). Compared to Evan et al. (2012b), the forcing from small scale waves (parametrized waves in MPI-ESM) is about equal, however, the large scale wave forcing (resolved waves in MPI-ESM) and the total forcing are stronger in MPI-ESM.

2.8 Summary and Discussion

This study presented an in depth analysis of the resolved wave forcing of the QBO in the Max Planck Institute Earth System model (MPI-ESM), which spectrally truncates at T63. Extending the work on the QBO forcing by Giorgetta et al. (2006), a spectral analysis of tropical precipitation as a proxy for wave sources, the temperature variance and the EP-flux in the stratosphere as performed for high resolution models by Kawatani et al. (2010a) and Evan et al. (2012b) documents the processes of wave generation, propagation and forcing for the applied course resolution model, thus setting a reference for the current generation of operational GCMs. Special emphasis is given to the dynamical and physical processes involved in the radiative and diffusive damping of resolved waves.

The T63 truncation of MPI-ESM limits this study to large scale waves, which compared to TRMM observations, have a realistic precipitation variance at wavenumbers lower than 20 and frequencies lower than 0.5 cpd. At these large scales and low frequencies, precipitation is mostly organized in Matsuno-type (Matsuno, 1966) Kelvin waves, mixed Rossby gravity waves and n0 westerly waves, which is a common feature in today's GCMs (Lott et al., 2013). However, the model underestimates the precipitation variance at wavenumbers large than 20 and frequencies higher than 0.5 cpd , which suggests that also the QBO wave forcing at these scales is too low and explains the need for gravity wave parametrisations in order to transport sufficient momentum into the stratosphere to force the QBO.

MPI-ESM shows the expected loss of spectral variance and wave-momentum flux due to the filtering effect of the QBO easterly and westerly jets, which have been reported by Ern and Preusse (2009b); Yang et al. (2011) and Evan et al. (2012b). The study linked the observed loss of spectral power to the Doppler shift of the waves' vertical wavelength and an associated increase of the waves amplitude, both leading to increased wave damping. The longwave radiative damping of the wave induced temperature perturbation is the dominant damping mechanism for large scale equatorial waves, which in accordance with high resolution studies, contribute about 40 and 50 % to the total resolved wave forcing of the QBO easterly and westerly jet, respectively. Horizontal diffusion of the zonal wind perturbation dissipates waves with zonal wavenumbers larger than 10 and frequencies larger than 0.5 cpd. In this respect, it is important to note that the time scales of the radiative wave damping decrease with zonal phase speed, which is to be expected from physical considerations, while horizontal diffusion

increases mostly with the zonal wavenumber. It is found that the horizontal diffusion scheme efficiently suppresses waves with wavenumbers larger than 20, independently of the wave's frequencies. Hence the suppressed spectrum, though resolved in the model, does not contribute considerably to the QBO's forcing.

The different damping mechanisms also manifest in the profiles of the vertical EP-flux and the wave induced zonal wind tendency. The forcing of the QBO westerly jet is confined to a thin vertical layer around the zero wind line, where most Kelvin waves do not meet critical levels but have sufficiently low vertical wavelengths to be efficiently damped by longwave radiation, and waves with phasespeeds considerably faster than the QBO westerly jet can contribute to its forcing. Easterly waves, however, are mostly damped by horizontal diffusion at critical levels, which spreads the easterly wave forcing from the zero wind line to the core of the easterly jets at higher altitudes.

The latitudinal dependence of the wave forcing found by Kawatani et al. (2010b) is also evident in MPI-ESM. The westerly forcing due to large scale equatorial waves is confined to a narrow band around the equator, while the forcing due to smaller scale waves with higher frequencies is strongest off the equator at the edges of the westerly jet and strongest in the summer hemisphere. This structure is consisted with the latitudinal structure of large and small scale waves proposed and shown by Matsuno (1966) and Kiladis et al. (2009). The easterly wave forcing of the QBO easterly jet is strongest in the winter hemisphere at the upper margin of the easterly jet, partly due to equatorward propagation of extra-tropical easterly waves and partly due to westerly winds in the lower stratosphere, which facilitate the propagation of easterly waves.

The investigated model run covers 209 quasi-biennial cycles, which gives the unique opportunity to study the mean evolution of the QBO forcing during a whole cycle. It is found that because large scale waves are mostly damped by radiation also away from critical levels, the EP-flux they carry diverges even when the background flow is opposite to their propagation direction and therefore, would be favourable for their upward propagation. Hence, the waves' contribution to the forcing of the QBO jets decreases with increasing altitudes of the zero wind line, when the waves propagate through an increasingly deep layer in the lower stratosphere. Waves with wavenumbers much smaller than the truncation limit no longer contribute substantially to the QBO's forcing at high altitudes.

As already proposed by Takahashi (1999), horizontal diffusion effectively limits the modelled wave activity in the stratosphere. However, due to observational limitations, it is difficult to validate the simulated strength of resolved stratospheric wave field. Increasing the horizontal resolution of the model and adjusting the applied horizontal diffusion should allow to estimate the constraints on wave propagation in the low resolution version.

Chapter 3

The influence of the spectral resolution on resolved wave mean flow interactions in ECHAM6

Abstract: This study compares the wave forcing of the Quasi-Biennial Oscillation (QBO) based on AMIP-type simulations with two versions of the ECHAM6 atmospheric model with spectral truncations of T63 and T255 (1.9° and 0.4° horizontal resolution, respectively) and 95 vertical levels (700 m vertical resolution). Both models internally generate a QBO like oscillation with periods of 25.5 and 18.7 months, respectively. In the low and high resolution version of the applied model, the sum of the resolved and parametrized wave forcing of the QBO jets is equal during most of the quasi-biennial cycle. Due to its lower amplitude, the oscillation in the high resolution version needs less momentum to swing back and forth, thus, the QBO period is 7 months shorter. The lower amplitude is due to increased resolved easterly wave drag within the QBO westerly jet in the upper stratosphere. In the lowermost stratosphere, waves with wave numbers up to 30 are stronger in the low resolution version. However, the horizontal diffusion, which weakens the waves as they propagate away from the tropospheric wave sources towards the zero wind lines below the QBO jets, is stronger too. Hence, the resolved wave forcing in the low resolution version is mostly due to waves with wave numbers lower than 20, whereas in the high resolution version, waves with wave numbers up to 120 contribute considerably to the momentum balance.

3.1 Introduction

The Quasi-Biennial Oscillation (QBO) dominates the general circulation in the tropical stratosphere (Baldwin et al., 2001). The most prominent feature of the QBO are easterly and westerly jets which alternate with a period ranging from 22 to 32 months, originate in the upper stratosphere and propagate downwards to the vicinity of the tropopause (Baldwin et al., 2001). This study compares the spectral distribution of the QBO's wave forcing based on two versions of the ECHAM6 atmospheric model with spectral truncations of T63 and T255 and 95 vertical levels.

The QBO is driven by vertically propagating atmospheric waves which deposit easterly and westerly momentum due to radiative attenuation, critical layer absorption and wave breaking (Lindzen and Holton, 1968; Holton and Lindzen, 1972). The wave attenuation is most efficient where the zonal phase speed of a wave is close to the zonal wind speed. Waves which deposit their wave momentum around the zero wind line between easterly and westerly jets drive the zero wind line downwards, towards the wave sources. However, Dunkerton (1997) found that the upwards directed equatorial branch of the Brewer-Dobson circulation works against the downward propagation of the QBO jets. Observational studies show that a continuous spectrum of large scale equatorial waves and small scale gravity waves transports the momentum necessary to drive the QBO (Dunkerton, 1991; Sato and Dunkerton, 1997; Ern et al., 2009a). The waves are mostly triggered by tropical convection (Wheeler and Kiladis, 1999; Piani et al., 2000; Fritts and Alexander, 2003; Kiladis et al., 2009; Ortland et al., 2011).

Owing to the wide range of scales, from planetary scale Klevin, Rossby and Mixed Rossby Gravity waves (Matsuno, 1966) to small scale gravity waves, it is not yet possible to close the stratospheric momentum balance based on observations (Alexander et al., 2010; Evan et al., 2012a), which is why atmospheric models are still the optimal choice for studies on QBO dynamics. However, only few of today's climate models are able to internally generate the QBO. To support the QBO, models have to allow the generation, transportation and dissipation of sufficient wave momentum to propagate the QBO jets against the resistance of the tropical upwelling.

Krismer and Giorgetta (2014) showed that a GCM which truncates at T63 underestimates the resolved wave forcing not only due to the lack of waves with zonal wave numbers beyond the truncation limit, but also because there is almost no wave momentum transported by waves with zonal wave numbers larger than 40 (λ=1000 km at the equator). In numerical models employing the spectral transform method, waves close to the truncation limit are damped by strong horizontal diffusion. Takahashi (1996, 1999) demonstrated that increasing the e-folding time of the dissipative wave damping has the same effect as increasing the truncation limit, namely a strengthening of the QBO's resolved wave forcing. However, the damping time scales required to resolve sufficient wave forcing at low spectral resolutions are inappropriate to simulate a realistic global climate (Takahashi, 1996, 1999). Hence, unresolved waves and their interaction with the resolved flow are parametrized, as done by Scaife et al. (2000); Giorgetta et al. (2002, 2006) and Krismer and Giorgetta (2014). The choice of the source spectrum and the breaking criteria of the parametrized waves alters the QBO's period and amplitude (Scaife et al., 2000; Giorgetta et al., 2006) and hence, mask shortcomings of the resolved dynamics. However, gravity wave parametrization generally do not reach the full complexity and accuracy of wave generation and wave-mean flow interactions and it is desirable to resolve the waves necessary to drive the QBO with GCMs having high horizontal and vertical resolution. Giorgetta et al. (2006) increased a GCM's truncation limit from T43 to T63 but kept the parametrized wave settings, and noticed a strengthening of the QBO westerly jet in the upper stratosphere. Based on high resolution models without gravity wave parametrizations, Kawatani et al. (2010a); Ortland et al. (2011) and Evan et al. (2012b) showed that waves with zonal wave numbers up to 200 (λ=200 km at the equator) contribute considerably to the QBO's momentum budget. Kawatani et al. (2010a) reduced the truncation limit from T213 to T105,

which lead to the decrease of the resolved wave forcing by the amount contributed by waves only resolved in the high resolution version.

Giorgetta et al. (2006) and Kawatani et al. (2010a) did not directly compare the spectral distribution of the QBO's wave forcing in the low and high resolution versions of the applied models, the stratospheric momentum balance in association with the QBO jets or the QBO features evolving from their different model setups. Thus, it is not know to which extend models with relatively course resolution limit the representation of the waves they resolve, and how the QBO reacts on the shift of the wave forcing from parametrized to resolved waves. This study addresses these questions. Therefore, the QBO amplitude and period, the momentum balance and the spectral wave fields in two versions of the ECHAM6 atmospheric GCM using spectral truncations at wave number 63 and 255 are compared. The parametrized wave sources are reduced in the high resolution version as the resolved wave spectrum is larger than in the low resolution version. The study also investigates to which extend the high resolution version better represents waves close to the truncation limit of the hgh resolution version.

The paper is structured as follows: The model is described in section 3.2. Section 3.3 compares the representation of the QBO and the semi-annual oscillation in both model versions and ERA-Interim. Section 3.4 compares the stratospheric momentum balance and its individual terms and section 3.5 compares the wave number-frequency spectra of tropical precipitation and the wave momentum flux in the high and low resolution version of ECHAM6.

3.2 Model Description

This work makes use of two AMIP-type simulations conducted with the ECHAM6 atmospheric GCM (Stevens et al., 2012) using spectral truncations at wave number 63 (Giorgetta et al., 2013a) and 255, and an associated Gaussian grid of approximately 1.9° and 0.4° resolution, respectively. For brevity, the two ECHAM6 versions will hereafter be referred to as E6-MR and E6-XR, respectively. In both versions, the vertical grid has 95 hybrid sigma pressure levels resolving the atmosphere from the surface up to the center of the uppermost layer at 0.01 hPa. The top-of-the-model pressure is defined as 0 hPa. This grid has a nearly constant vertical resolution of 700 m from the upper troposphere to the middle stratosphere, and the resolution is better than 1 km at the stratopause. The version truncated at wave number 63 is the atmospheric part of the Max Planck Institute Earth System Model (MPI-ESM) (Giorgetta et al., 2013b), and a number of recent publications based on E6-MR review the dynamics of the middle atmosphere (Schmidt et al., 2012a), the resolved wave forcing and seasonal modulation of the Quasi-Biennial Oscillation (Krismer and Giorgetta, 2014; Krismer et al., 2013), the stratosphere-troposphere coupling (Tomassini et al., 2012), tropical precipitation (Crueger et al., 2013) and model tuning (Mauritsen et al., 2012).

In the following, the major parts of ECHAM6 relevant for this paper are discussed. In general, all specifications apply to the low and high resolution version. The high resolution version required some additional tuning in order to obtain a realistic global

climate when coupling E6-XR to an ocean model. The tuning followed the procedure reported by Mauritsen et al. (2012).

Owing to the higher resolution in E6-XR, the time step of the numerical integration was set from 450 to 120 s and the e-folding damping time for the largest wave number in the horizontal diffusion scheme for vorticity, divergence and temperature was reduced from 7 to 0.5 hours. As discussed below, the diffusive damping on large scale waves is weaker than in E6-MR.

ECHAM6 includes the sub-grid scale orography scheme described by Lott (1999) and the Hines parametrization (Hines, 1997a,b) for unresolved orographic and non orographic gravity waves, respectively. The launch level of the non orographic gravity waves is at 700 hPa. The source spectrum of the Hines parametrization follows the MAECHAM5 standard setting (Manzini and McFarlane, 1998; Manzini et al., 2006). However, in E6-MR, the otherwise constant wave-induced horizontal wind perturbations (rms winds) increase linearly from 1 to 1.2 m/s over 10°N to 5°N (10°S to 5°S). From 5°N to 5°S, the rms winds are constant at 1.2 m/s. The modification of source spectrum of the Hines parametrization was necessary to obtain a realistic QBO in MPI-ESM, where E6-MR is coupled to an ocean model. After increasing the rms winds, the zonal parametrized wave drag at the zero wind lines associated with the onset of the QBO jets is about four times larger. Given the lack of observational constraints on tropical gravity waves and considering that the mostly convective non-orographic wave sources, which are represented by the Hines scheme, are more abundant in the tropics than in the extra-tropics, such an enhancement seems to be justified. The prescribed gravity wave sources are constant in time.

Compared to E6-MR, E6-XR resolves a larger spectrum of horizontal wave numbers which thus, no longer need to be parametrized. To keep the biases of the stratospheric polar jets within an acceptable range, the rms winds in the Hines scheme in E6-XR are set to 0.9 globally and the orographic gravity waves are weakened by 75%. As shown in the next section, the reduction of the gravity wave drag in E6-XR was to modest to prevent the QBO period from being to short.

The parametrization of convection, which is known to influence the resolved wave field in atmospheric models, follows the Tiedtke-Nordeng scheme (Möbis and Stevens, 2012). In E6-XR, the relative cloud mass flux one level above the non-buoyancy level and the coefficients for determining the conversion from cloud water to rain have been reduced (0.23 to 0.16 and $2e^{-4}$ to $1.2e^{-4}$, respectively) in order to keep the cloud cover, the liquid water path, the precipitation rate and the top of the atmosphere radiation balance within acceptable limits (Mauritsen et al., 2012). The variability of tropical precipitation in both ECHAM6 versions is compared to TRMM observations in section 3.5.

3.3 Zonal Wind in the tropical Stratosphere

Figure 3.1 shows the time/height cross sections of the zonal mean zonal wind in the tropical stratosphere averaged from 5°N to 5°S in ERA-Interim (Fig. 3.1a) and

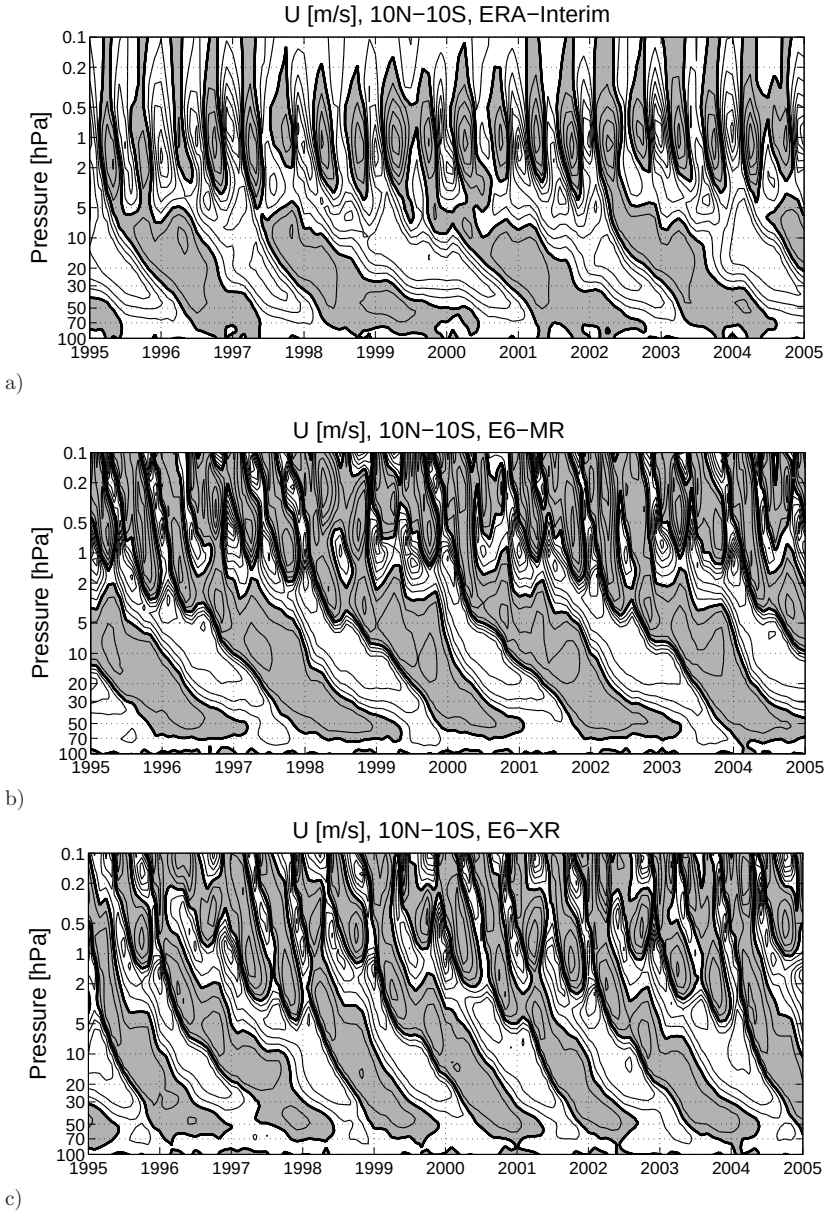

Figure 3.1: Time-height cross section of the monthly mean zonal mean zonal wind in the tropical stratosphere in a) ERA-Interim, b) E6-MR and c) E6-XR, averaged from 5°N to 5°S. The contour interval is 10 m s^{-1}. Positive wind speeds are highlighted in gray. The zero wind line is indicated by the thick black contour.

ECHAM6 with the spectral truncation at T63 and T255, respectively (Fig. 3.1b, c, respectively). Between 100 and 5 hPa, the three datasets complete about 6, 7 and 10 cycles of alternating easterly and westerly jets within the displayed 15 years. The QBO period amounts to 28.7, 25.5 and 18.7 months in ERA-Interim, E6-MR and E6-XR, respectively (Fig. 3.2a). Despite its much shorter period in E6-XR, the oscillation in the high resolution model will be called quasi-biennial for simplicity.

Consistent with ERA-Interim, the QBO westerly jets in E6-MR and E6-XR propagate regularly from the upper stratosphere to the vicinity of the tropopause. The downward propagation rate of the QBO westerly jet is larger in E6-XR (4 months from 20 to 50

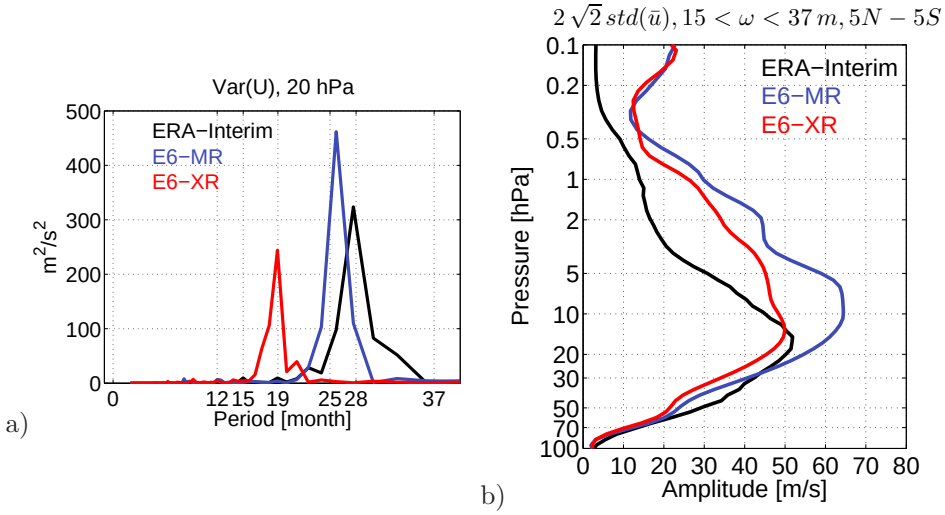

Figure 3.2: a) Variance of the montly mean zonal mean zonal wind averaged from 5°N to 5°S at 20 hPa in $m^2\ s^{-2}$ in ERA-Interim (black line), E6-MR (blue line) and E6-XR (red line). b) Profiles of the peak to peak zonal wind amplitude of the QBO in ERA-Interim (black line), E6-MR (blue line) and E6-XR (red line). A spectral filter with band passed periods of 15 to 37 months has been used to isolate the signal of the QBO.

hPa) than in ERA-Interim and E6-MR (6 months from 20 to 50 hPa).

In ERA-Interim, the stalling of the QBO easterly jet below 30 hPa, for example between 1992 and 1994 and between 1998 and 2002 in Figure 3.1a, locks the QBO in a specific phase and prolongs the quasi-biennial cycle. The stalling can be attributed to seasonal variations of the tropical upwelling and the wave forcing of the QBO easterly and westerly jets (Kinnersley and Pawson, 1996; Krismer et al., 2013) as well as volcanic activity and ENSO. The stalling is simulated with E6-MR (Fig. 3.1b), however, only weakly developed in E6-XR (Fig. 3.1c), which contributes to the shortening of the QBO period.

Figure 3.2b shows profiles of the QBO's zonal wind amplitude in ERA-Interim and the two ECHAM versions, where band pass filters of 15 to 37 months have been used to isolate the QBO signal. In ERA-Interim, the QBO amplitude is close to 0 below 100 hPa , maximal at 20 hPa and decreases slowly at higher altitudes (black line in Fig. 3.2b). In E6-MR, the QBO is strongest at 10 hPa and the peak amplitude is 15 m/s larger than in ERA-Interim (blue line in Fig. 3.2b). In E6-XR, the peak amplitude is 3 m/s smaller than in the reanalysis, however, the whole amplitude profile is shifted to higher altitudes (red line in Fig. 3.2b). Hence, the QBO in E6-XR is weaker than in the reanalysis at pressure levels higher than 10 hPa and stronger below.

Above 5 hPa, both ECHAM6 versions show the semiannual oscillation (SAO) of westerly and easterly jets (Fig. 3.1). The SAO is best illustrated in the climatology of the stratospheric zonal wind, shown for ERA-Interim and ECHAM6 in Figure 3.3. In ERA-Interim, the SAO jets, which are strongest at 1 hPa, propagate down to 5 hPa (Fig. 3.3a). The amplitude of the SAO is stronger during the semiannual cycle starting in December and ending in June, when the easterly and westerly jets reach -40 m/s and +30 m/s, respectively. In July and October, the jets only reach ± 15 m/s, respec-

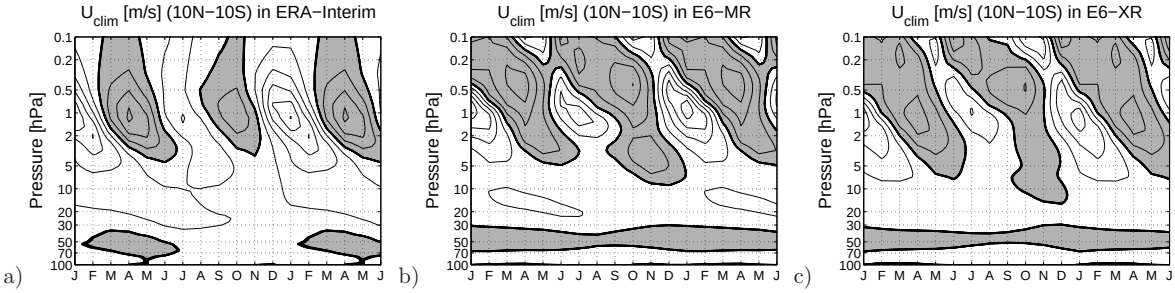

Figure 3.3: Time-height cross section of the climatological zonal mean wind U(clim) in a) ERA-Interim, b) E6-MR and c) E6-XR, averaged from 5°N to 5°S. The contour interval is 10 m s^{-1}. Positive wind speeds are highlighted in gray. The zero wind line is indicated by the thick black contour.

tively. The annual modulation of the SAO amplitude is well observed and associated with stronger meridional momentum advection in boreal winter (Delisi and Dunkerton, 1988). In E6-MR, the core of the SAO jets is located at 0.5 hPa (Fig. 3.3b), which is higher than in ERA-Interim. The strength of the SAO easterly and westerly jets amounts to -40 and 30 m/s in January and April, respectively, and to -30 and 25 m/s in June and October, respectively. Thus, in E6-MR, the first semi-annual cycle matches ERA-Interim, however, the second semi-annual cycle is stronger than in ERA-Interim. In E6-XR (Fig. 3.3c), the amplitude of the SAO is generally weaker than in E6-MR. The strength of the SAO easterly and westerly jets amounts to -25 and 20 m/s in January and April, respectively, and to -10 and 15 m/s in June and October, respectively. Thus, in E6-MR, the first semi-annual cycle is weaker than in ERA-Interim, however, the second semi-annual cycle matches the reanalysis. In both ECHAM6 versions, the signal of the SAO westerly jet starting at 1 hPa in August/September propagates deep into the stratosphere down to 10 hPa (Fig. 3.3b, c). This is due to the QBO westerly jets which are induced in the upper stratosphere by SAO westerly jets and hence, almost exclusively occur in spring and fall (Kuai et al., 2009; Krismer et al., 2013). The QBO westerly jets tend to be more persistent in winter than in spring due to seasonally enhanced vertical upwelling and a lower downward propagation rate (Krismer et al., 2013). Therefore the QBO westerly jets can project onto the climatological mean. This also shows in ERA-Interim, where compared to the period from January to March, the zonal wind between 2 and 20 hPa is only weakly easterly from March to December (Fig. 3.3a). Also the bands of westerly winds between 30 and 100 hPa in ERA-Interim, which persist over the whole climatological year in both ECHAM6 versions, are due to the more frequent occurrence of the QBO westerly jets.

3.4 The Zonal Momentum Balance

Above it has been shown that in E6-XR, the QBO period is shorter, the strength of the QBO jets is weaker and the stalling of the QBO jets in the lower stratosphere is less pronounced than in ERA-Interim and E6-MR. The discussion of the dynamics of the stratosphere is usually based upon the Transformed Eulerian Mean (TEM) momentum equation (Andrews et al., 1987), which states:

$$\bar{u}_t = \bar{v}^* \left[f - (a\,cos\phi)^{-1} (\bar{u}\,cos\phi)_\phi \right] - \bar{w}^* \bar{u}_z + (\rho_0\, a\, cos\phi)^{-1} \nabla \cdot F + \bar{X} \tag{3.1}$$

where ρ_0 is the log-pressure height-dependent density, a is the Earth radius and ϕ and z are the latitude and the log-pressure height. $\bar{u}$ is the zonal mean zonal wind and f is the Coriolis parameter ($f \equiv 2\Omega\, sin\phi$ and Ω is the rotation rate of the Earth). Subscripts ϕ, z and t denote the meridional, vertical and temporal derivatives. $\bar{v}^*$ and $\bar{w}^*$ are the meridional and vertical residual mean winds defined as

$$\bar{v}^* = \bar{v} - \rho_0^{-1} (\rho_0\, \overline{v'\,\theta'} / \bar{\theta}_z)_z \tag{3.2}$$

$$\bar{w}^* = \bar{w} + (a\,cos\phi)^{-1} (cos\phi\, \overline{v'\,\theta'} / \bar{\theta}_z)_\phi \tag{3.3}$$

where $\bar{v}$ and $\bar{w}$ are the zonally averaged meridional and vertical wind, θ is the potential temperature and the primes indicate the deviation of the variables from their monthly mean zonal mean.

∇·F in Equation 3.1 denotes the vertical and meridional divergence of the Eliassen Palm flux (EP-flux), which is a measure of the transport and deposition of zonal momentum by atmospheric waves in the stratosphere (Andrews et al., 1987). F is defined as

$$F^{(\phi)} = \rho_0\, a\, cos\phi\, (\bar{u}_z\, \overline{v'\,\theta'} / \bar{\theta}_z - \overline{u'\,v'}) \tag{3.4}$$

$$F^{(z)} = \rho_0\, a\, cos\phi \left[\left(f - \frac{(\bar{u}\,cos\phi)_\phi}{a\,cos\phi} \right) \overline{v'\,\theta'} / \bar{\theta}_z \right] - \overline{u'\,w'} \tag{3.5}$$

In this study, F denotes the EP-flux carried by resolved waves with zonal wave numbers k ranging from 0 to 63 in E6-MR and ranging from 0 to 255 in E6-XR.

In Equation 3.1, the residual term $\bar{X}$ includes the non-orographic gravity wave drag and horizontal and vertical diffusion. However, these terms have not been stored for the high resolution ECHAM6 run. Therefore, $\bar{X}$ is computed according to Equation (3.1) as the difference of the total acceleration minus the sum of the advective terms and the resolved wave forcing. To investigate the composition of $\bar{X}$, the parametrized wave drag and the diffusion terms in the low resolution ECHAM6 have been compared. Locally, all three terms are of the same order of magnitude. However, in the zonal mean, the parametrized wave drag is two orders of magnitude higher than the diffusive terms, and there is no reason to expect that these terms could become comparable to the wave drag even after reducing the parametrized wave sources in E6-XR.

In ERA-Interim, the QBO does not emerge from the freely running model and thus, is generated through the assimilation process. Ern et al. (2008) found that ERA-40

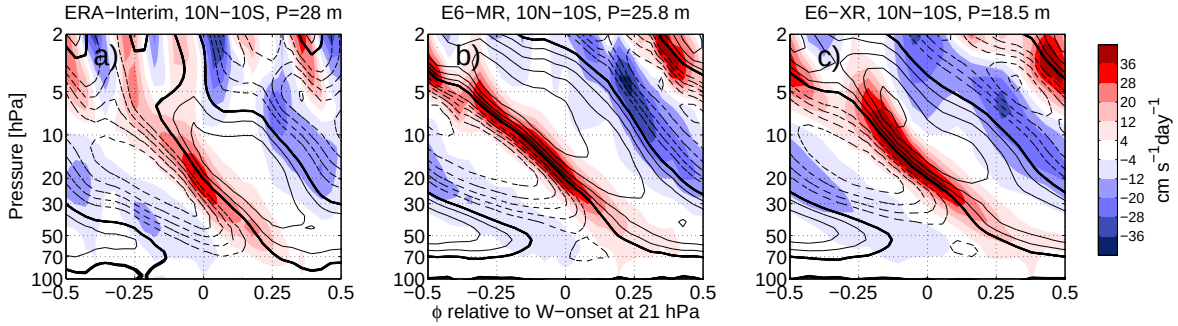

Figure 3.4: Time-height cross section of the composites of the zonal mean zonal wind in m s^{-1} (contour) and its acceleration in cm s^{-1} day^{-1} (shading) in a) ERA-Interim, b) E6-MR and c) E6-XR. The contour interval is 10 m/s. Positive wind speeds are solid, negative wind speeds are dashed. The zero wind line is indicated by the thick black contour. The x axis shows the QBO phase ϕ which is the time in months relative to the onset of the QBO westerly jet at 20 hPa divided by the average QBO periods in the respective dataset.

well represents Kelvin waves, but underestimates the variances due to gravity waves by a factor of 3 when compared to satellite observations. This did not improve in ERA-Interim (Maury et al., 2011) and thus, it has to be expected that the term $\nabla \cdot F$ in ERA-Intrim (Eq. 3.1) is smaller than the real wave forcing. An additional term, which accounts for the assimilation increments, enters the momentum balance (Eq. 1) in ERA-Interim. However, unlike gravity wave parametrizations in GCMs, which also account for missing resolved wave drag, this additional term in ERA-Interim is not based on physical considerations. Hence, for ERA-Interim, only the total acceleration $\bar{u}_t$ is considered in the following discussion.

Figure 3.4 shows composites of the zonal mean zonal wind (contours) and the zonal wind tendency $\bar{u}_t$ (shading) in the tropical stratosphere for ERA-Interim and the low and high resolution ECHAM6. The composites are based on the onset of the QBO westerly jet at 20 hPa (ϕ=0). The time axis has been transformed to the QBO phase ϕ by dividing time by the QBO period in the respective data-set. Thus, panel a to c in Figure 3.4 show the progression of the QBO jets over an average quasi-biennial cycle from ϕ=-0.5 to ϕ=+0.5, which corresponds to a time period of 28.7, 25.5 and 18.7 months in ERA-Interim, E6-MR and E6-XR, respectively.

During the first half cycle of the QBO (-0.5< ϕ <0), the tendency around the zero wind line associated with the onset of the QBO easterly jet between 10 and 70 hPa is strongest in E6-XR, which is consistent with the shorter stalling period of the QBO easterly jets below 30 hPa. The forcing around the zero wind line associated with the onset of the QBO westerly jet, which propagates from 10 to 70 hPa over the half-cycle from ϕ=-0.25 to ϕ=+0.25, is weakest in ERA-Interim, however, about equally strong in the two ECHAM6 versions. This is puzzling, as the QBO phase progression is faster in E6-XR than in E6-MR.

To clarify this apparant contradiction, Figure 3.5 shows the zonal momentum $\rho(z)\bar{u}(z)$ and the momentum tendency $\rho(z)\bar{u}_t(z)$ for the composites shown in Figure 3.4, integrated over the volume between 30 and 10 hPa. The rate of change of momentum within the volume is positive between ϕ=$\pm$0.25 (dashed lines in Fig. 3.5). This corre-

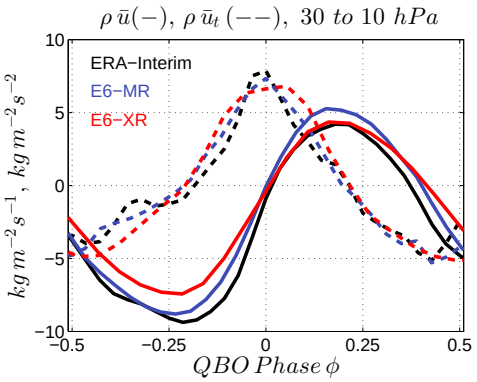

Figure 3.5: Zonal momentum $\rho(z)\bar{u}(z)$ (solid lines) and momentum tendency $\rho(z)\bar{u}_t(z)$ (dashed lines) integrated from 30 and 10 hPa and averaged from 10°N to 10°S in ERA-Interim (black line), E6-MR (blue line) and E6-XR (red line) over a quasi biennial cycle from ϕ=-0.5 to ϕ=+0.5.

sponds to the time between the phase when the region of pronounced westerly forcing around the onset of the QBO westerly jet enters the volume at 10 hPa at ϕ=-0.25 and when the zero wind line leaves the volume at 30 hPa at ϕ=+0.25 (Fig. 3.4). The rate of change of momentum is about equal in all three models. However, when the acceleration becomes positive at ϕ=-0.25, the momentum within the volume (solid lines in Fig. 3.5) is least negative in E6-XR, as the QBO easterly jet is roughly 5 m/s slower than in ERA-Interim and E6-MR (Fig. 3.4). Hence, given the same rate of change of momentum as in the other models, the transition from minimal (most easterly) to maximal (most westerly) momentum within the volume from ϕ=-0.25 to ϕ=0.25 consummates the least time in E6-XR (7 months). Considering the whole wind profile, the faster build up of westerly momentum manifests in the faster propagation of the QBO westerly jet.

Note that at ϕ=+0.25, the momentum within the volume is less westerly in E6-XR than in E6-MR, which has two reasons. First, as the region of strong westerly forcing leaves the volume earlier in E6-XR than in E6-MR, there is less time to deposit westerly momentum. Second, at $\phi = 0$, E6-XR shows strong easterly forcing above 5 hPa (Fig. 3.4c), which is not yet present in the other models (Fig. 3.4a, b). The stronger forcing supports the development of the QBO easterly jet and weakens the QBO westerly jet during a comparatively early stage of the quasi-biennial cycle. As the weaker QBO easterly jet between 30 and 10 hPa facilitated the progression of the QBO westerly jet, the weaker QBO westerly jet facilitates the progression of the QBO easterly jet. This brings the period of easterly momentum deposition forward and thus, completes the quasi-biennial cycle in E6-XR faster than in E6-MR.

The profiles of the individual forcing terms of the momentum equation at $\phi = 0$, which are shown in Figure 3.6, demonstrate that compared to E6-MR, the surplus of easterly momentum above 10 hPa in E6-XR comes from the divergence of the EP-flux transported by resolved waves (dashed dark and light gray lines in Fig. 3.6b). Above 10 hPa, the residual terms (Fig. 3.6c) and the advective terms (Fig. 3.6d, e), however, are about equal in both models. The stronger resolved wave forcing in E6-XR was to be expected, as E6-XR resolves a larger spectrum of waves than E6-MR. Also in the

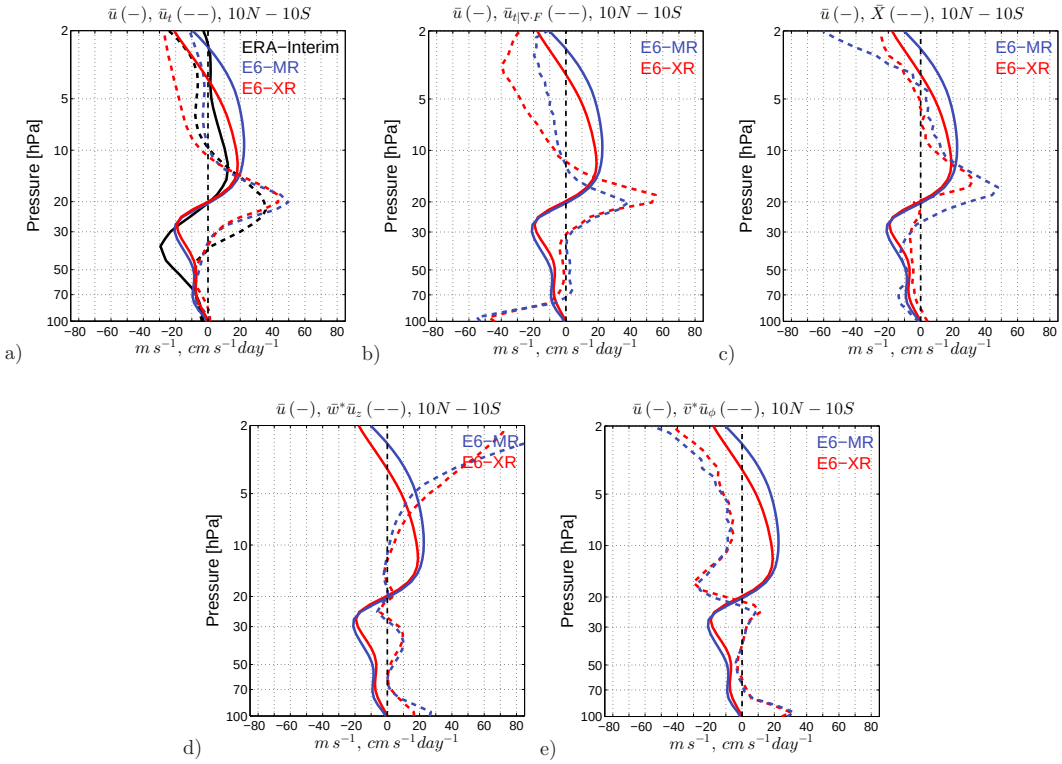

Figure 3.6: Profiles of the zonal mean zonal wind in m s^{-1} (solid line) and the terms of the momentum equation (dashed lines) averaged over months when the QBO westerly jet starts at 20 hPa in ERA-Interim (black line), E6-MR (blue line) and E6-XR (red line). The zonal wind and the tendencies have been averaged from 5°N to 5°S and from 10°N to 10°S, respectively. The panels show a) the total acceleration of the zonal wind $\bar{u}_t$, b) the acceleration due to the resolved EP-flux divergence $\bar{u}_{t\,\nabla.F}$, c) the parametrized wave drag and diffusion $\bar{u}_{t\,\bar{X}}$ and d), e) the vertical and horizontal momentum advection $\bar{w}^*\bar{u}_z$ and $\bar{v}^*\,[f\,-\,(a\,cos\phi)^{-1}$ in cm s^{-1} day $^{-1}$.

middle stratosphere between 10 and 30 hPa, the resolved wave drag in E6-XR is up to 0.2 m s^{-1} day^{-1} stronger than in E6-MR (Fig. 3.6b). To compensate for the expected increase of momentum flux carried by resolved waves, the rms wind, which controls the amplitude of the parametrized wave sources in the Hines scheme, was set from 1.2 in E6-MR to 0.9 in E6-XR. Accordingly, the residual term $\bar{X}$ (dashed lines in Fig. 3.6c), which mostly represents the parametrized wave drag, is up to 0.2 m s^{-1} day^{-1} weaker in E6-XR than in E6-MR.

Below 10 hPa, the different settings of the parametrized wave sources seem to be well suited, as the total forcing u_t is about the same in E6-MR and E6-XR (dashed gray lines in Fig. 3.6a).

In ERA-Interim, the mean flow acceleration at the altitude of the zero wind line associated with the onset of the QBO westerly jet is weaker than in ECHAM6, but extends deeper into the QBO easterly jet below (dashed lines in Fig. 3.6a). This is illustrated for the average quasi-biennial cycle in Figure 3.3 and for the onset of the QBO westerly jet at 20 hPa in Figure 3.6a. Compared to E6-MR, the stronger deceleration of the QBO easterly jet in ERA-Interim compensates for the weaker forcing of the westerly jet,

and the QBO period is about the same in both models. Omitting the possible influence of advection, the differences of the QBO forcing and amplitude between ERA-Interim and ECHAM6 could due to different characteristics of the wave fields. Based on a one dimensional model using the Hines scheme, Scaife et al. (2000) showed that the QBO period and amplitude vary with the parametrized source strength and the characteristic vertical wave number of the Hines scheme, which determines where the parametrized gravity waves give momentum to the flow. Hence, differential distribution of the wave forcing can lead to QBO like oscillation with similar periods but different amplitudes.

3.5 Spectral Distribution of Resolved waves in low and high resolution

The spectral distribution of the QBO's wave forcing is one of the key question of QBO studies ever since Lindzen and Holton (1968) proposed wave-mean flow interactions as its driving mechanism (Holton and Lindzen, 1972; Plumb, 1977; Dunkerton, 1997; Baldwin et al., 2001; Kawatani et al., 2010a; Yang et al., 2011; Ortland et al., 2011; Evan et al., 2012b; Krismer and Giorgetta, 2014). The discussion above revealed that the stronger wave forcing in E6-XR compared to E6-MR is crucial for the shorter QBO period in the high resolution model. How the - compared to E6-MR - higher spectral resolution in E6-XR changes the resolved wave field and causes the stronger wave forcing is investigated next.

Most of the tropical waves are generated by convection, and tropical precipitation is a widely used proxy for the tropical convective activity. Figure 3.7 shows the tropical precipitation variance in TRMM observations (Huffman et al., 2007), E6-MR and E6-XR as a function of the zonal wave number. To obtain the variances, the zonal wave number-frequency spectra of precipitation have been calculated using the fast Fourier transform in longitude and time at each latitude for each month of the period from 1998 to 2008. Over the selected period, TRMM observations overlap with the AMIP

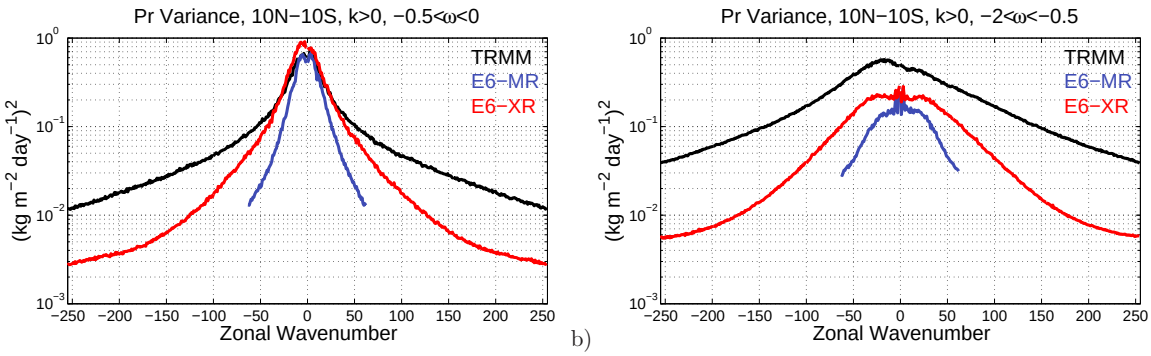

Figure 3.7: Total variance of the zonal mean precipitation in TRMM (black line), E6-MR (blue line) and E6-XR (red line) in log((kg m^{-2} day^{-1})^2), averaged from 10°N to 10°S as a function of the planetary wave number integrated over frequencies ranging from 0 to 0.5 cpd (a) and from 0.5 to 2 cpd (b). Frequencies ranging from 0.9 to 1.1 cpd have been excluded from the integrals to avoid sampling the spectral peaks associated with the daily cycle

observations which force the ECHAM6 model runs. The zonal wave number-frequency spectra have been averaged over the latitudinal band from 10°S to 10°N. The instantaneous precipitation rates of the high resolution model run (and all other variables) are stored once every 6 hours, which limits the analysis to waves with frequencies lower than 2 cycles per day (cpd). The TRMM data has been interpolated to the 0.5° grid used in E6-XR. For Figure 3.7, the zonal wave number-frequency spectra have been integrated over frequencies ranging from 0 to 0.5 cpd (Fig. 3.7a) and from 0.5 to 2 cpd (Fig. 3.7b). Frequencies ranging from 0.9 to 1.1 cpd have been excluded from the integrals to avoid sampling the spectral peaks associated with the daily cycle

At frequencies lower than 0.5 cpd and wave numbers up to 10, the variance in E6-MR (blue line in Fig. 3.7a) matches TRMM observations (black line in Fig. 3.7a). However, the variance decreases too quickly at higher wave numbers. In E6-XR, the low frequency precipitation variance compares well to TRMM up to wave number 30 and is larger than in E6-MR over the whole range of wave numbers resolved in both model versions (red line in Fig. 3.7a). Hence, increasing the spectral resolution does not only add precipitation variance due to previously unresolved waves, but also improves the representation of waves with relatively low zonal wave numbers. However, as E6-MR, E6-XR underestimates tropical precipitation variance beginning at wave numbers well below the truncation limit of T255.

In both ECHAM versions, the precipitation variance due to waves with frequencies larger than 0.5 is smaller than in TRMM over the whole range of zonal wave numbers (Fig 3.7b). Tropical precipitation is strongly related to the sea surface temperatures (SST). In the AMIP run, the models are forced with observed SSTs, however, with only monthly temporal resolution, which limits the temporal variability of the simulated precipitation. However, the variability in E6-XR is closer to TRMM than in E6-MR.

To compute the QBO's wave forcing due to individual waves, the zonal wave number-frequency spectrum of the EP-flux is computed following Horinouchi et al. (2003):

$$\begin{aligned} \frac{F^{(\phi)}(k,\omega)}{\rho_0\, a\, cos\phi} &= Real\,[\,\bar{u}_z\hat{v}(k,\omega)\hat{\theta}^*(k,\omega)/\bar{\theta}_z] - \\ &\quad Real\,[\,\hat{u}(k,\omega)\hat{v}^*(k,\omega)] \end{aligned} \tag{3.6}$$

$$\begin{aligned} \frac{F^{(z)}(k,\omega)}{\rho_0\, a\, cos\phi} &= Real\Big\{\Big[f - \frac{(\bar{u}\, cos\phi)_\phi}{a\, cos\phi}\Big]\,\hat{v}(k,\omega)\hat{\theta}^*(k,\omega)/\bar{\theta}_z\Big\} - \\ &\quad Real\{\hat{u}(k,\omega)\hat{w}^*(k,\omega)\} \end{aligned} \tag{3.7}$$

In Equations (3.6) and (3.7), a hat denotes the Fourier coefficients of the variables, whereas an asterisk denotes the complex conjugate. The Fourier coefficients have been derived by applying a Fast Fourier Transform in longitude and time for each month of the simulation separately, each month having six hourly data output. There is no temporal overlap between the months. k and ω denote the zonal wave number and frequency.

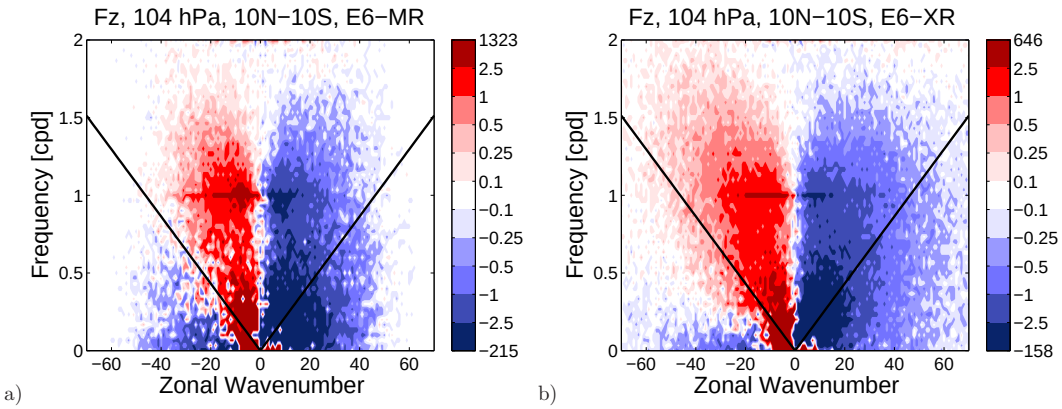

Figure 3.8: Latitudinal mean (10°N to 10°S) zonal wave number-frequency spectra of the vertical EP-flux at 104 hPa (kg m^{-2} s^{-2}) averaged over months when the QBO westerly jet starts at 20 hPa in a) E6-MR and b) E6-XR. The black lines indicate constant phase speeds of ± 10 m/s.

Figure 3.8 shows the wave number-frequency spectra of the vertical EP-flux at 104 hPa in E6-MR and E6-XR averaged over months defined as QBO phase ϕ=0 in section 3.4. In the selected months, the zonal wind is easterly between 80 and 20 hPa and westerly above (Fig. 3.6). Except for the daily cycle at 1 cpd, the EP-flux is largest at wave numbers lower than ±20 and frequencies lower than 0.5 cpd in both models. The EP-flux decreases quickly with increasing frequencies larger than 1 cpd. Due to Doppler shifted Kelvin waves, the EP-flux at zonal phase speeds between 0 and -10 m/s is directed downwards, contrary to the flux carried by faster easterly waves.

To facilitate the qualitative comparison of the stratospheric wave activity in both models, Figure 3.9 shows the vertical EP-flux integrated over frequencies ranging from -2 to 0 cpd as a function of the planetary wave number at 104, 30 and 10 hPa during the QBO phase ϕ=0 (note that negative frequencies and positive/negative wave numbers indicate westerly/easterly waves). In the logarithmic plot, positive and negative values are indicated by solid and dashed lines, respectively. Note that during the selected QBO phase, the zonal wind below 20 hPa is easterly, and a QBO westerly jet extends from 20 to 2 hPa (solid lines in Fig. 3.6)

At 104 hPa, westerly waves up to zonal wave number 25 carry more vertical EP-flux in E6-MR than in E6-XR and the EP-flux in both models still compares well up to zonal wave number 50 (Fig. 3.9a). Easterly waves, however, carry more EP-flux in E6-XR than in E6-MR starting at wave number -10 (Fig. 3.9d).

The EP-flux carried by easterly and westerly waves decreases between 104 and 30 hPa in E6-MR and E6-XR (cf. Fig. 3.9 a and b and d and e). However, the wave momentum away from the source regions should be independent of altitude in the absence of critical levels and wave damping (Lindzen, 1971). As only easterly waves with phase speeds slower than -20 m/s meet critical levels below 30 hPa, radiative wave damping and horizontal diffusion have to account for most of the apparent wave momentum deposition between 104 and 30 hPa. Krismer et al. (2013) showed that in E6-MR, waves with wave numbers larger than 20 are strongly damped by the horizontal diffusion of the zonal wind perturbation. Hence, at 30 hPa, waves with wave numbers

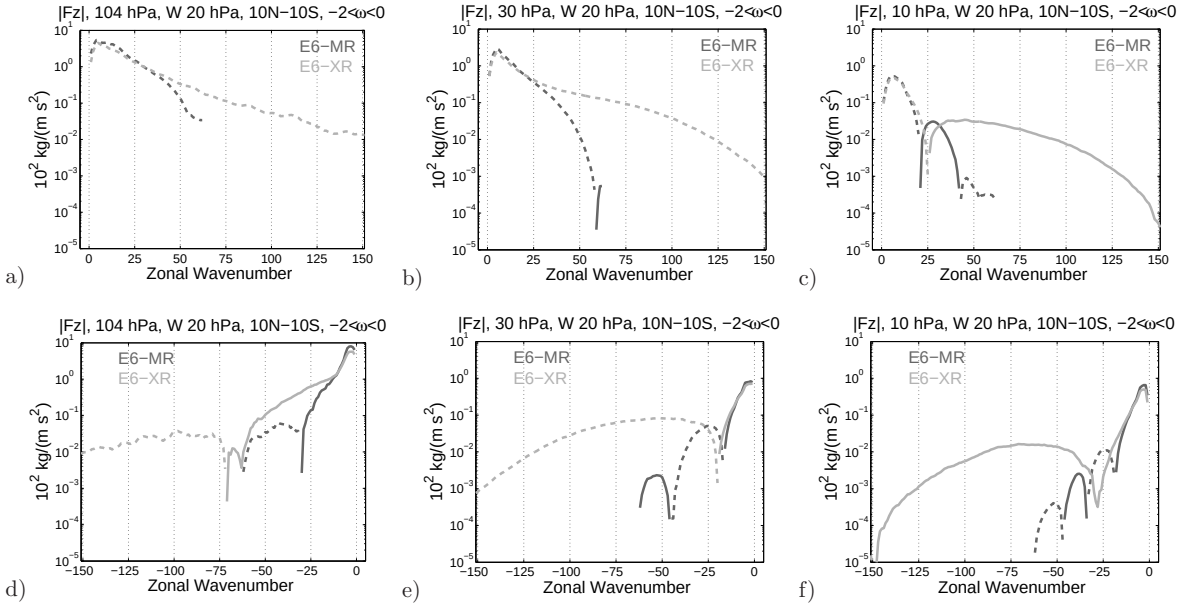

Figure 3.9: Latitudinal mean (10°N to 10°S) vertical EP-flux (kg m^{-2} s^{-2}) as a function of the planetary wave number in E6-MR (dark gray) and E6-XR (light gray) averaged over months when the QBO westerly jet starts at 20 hPa. Upward (positive) and downward (negative) EP-fluxes are drawn with solid and dashed lines, respectively. Panels a and d), b and e) and c and f) show the EP-flux at 104, 30 and 10 hPa, respectively. Panels a) to c) show westerly waves (positive wave numbers) and panel d) to f) show easterly waves (negative wave numbers).

ranging from 20 to 63 carry little westerly wave momentum (blue line in Fig. 3.9b). Due to the larger spectral resolution, the horizontal diffusion in E6-XR acts on larger wave numbers than in E6-MR and waves up to wave number 120 can propagate to 30 hPa with little loss of momentum (cf. red lines in Fig. 3.9a, b).

Between 30 and 10 hPa, the EP-flux carried by westerly waves again strongly decreases (cf. Fig. 3.9 b and c). Within the QBO westerly jet above 20 hPa, westerly waves are Doppler shifter to low intrinsic phase speeds and partly meet critical levels, which both facilitate the dissipation of westerly waves. Additionally, due to the positive temperature anomaly at the zero wind line associated with the onset of the QBO westerly jet, the temperature perturbations due to westerly and easterly waves alike strongly increase (not show). This further enforces thermal and diffusive wave damping and explains the reduction of wave momentum carried by easterly waves between 30 and 10 hPa (cf. Fig. 3.9 e and f). At 10 hPa, the EP-flux carried by westerly and easterly waves in E6-MR is again comparable to E6-XR up to wave number 20 and strongly decreases afterwards (Fig. 3.9c, f).

The zonal acceleration with results from the divergence of the total EP-flux ($\nabla \cdot [F_y, F_z]$) in E6-MR and E6-XR is shown in Figure 3.10 as a function of the zonal wave number (Fig. 3.10a, b) and integrated over zonal wave numbers ranging from 0 to 20, 21 to 63 and 64 to 255 (Fig. 3.10c, d) during the QBO phase ϕ=0. The wave forcing has been density corrected, summed over easterly and westerly waves (positive and negative wave numbers) and integrated from 10 to 30 hPa (Fig. 3.10a, c) and

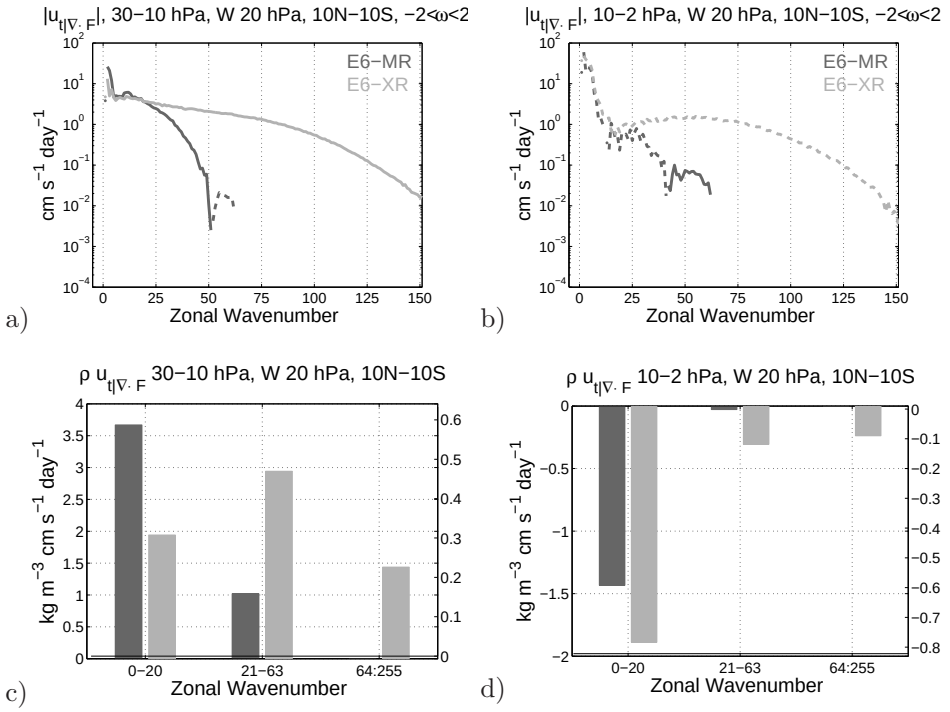

Figure 3.10: Latitudinal mean (10°N to 10°S) zonal wind tendency due to the divergence of the EP-flux (m s^{-1} day^{-1}) in E6-MR (dark gray) and E6-XR (light gray) averaged over months when the QBO westerly jet starts at 20 hPa. Westerly (positive) and easterly (negative) tendencies are drawn with solid and dashed lines, respectively. The tendencies have been integrated from a), c) 30 to 10 hPa and b), d) from 10 to 2 hPa. Panels a) and b) show the tendencies as a function of the zonal wave number and panels c) and d) show the tendencies binned over zonal wave numbers ranging from 0 to 20, 21 to 63 and 64 to 255, respectively.

from 10 to 2 hPa (Fig. 3.10b, d). As shown in Figure 3.6b, this is the altitude region with strong westerly forcing around the zero wind line associated with the onset of the QBO westerly jet (30 to 10 hPa) and the region within the QBO westerly jet, where the larger westerly wave forcing in E6-XR compared to E6-MR contributes to the weakening of the QBO westerly jet (10 to 2 hPa).

Figure 3.10a again illustrates that in E6-MR, most of the wave forcing comes from waves with wave numbers between 0 and 20. However, integrated over the respective bin of wave numbers, the total forcing in E6-MR is even stronger than in E6-XR (Fig. 3.10c). The forcing due to waves with wave numbers between 21 and the truncation limit 63 decreases quickly in E6-MR (Fig. 3.10a) and amounts to only 20 % of the total wave forcing (Fig. 3.10c). In E6-XR, however, the contribution from these waves stays relatively constant with increasing wave number (Fig. 3.10a) and amounts to 40 % of the total wave forcing (Fig. 3.10c). Waves with wave numbers larger than 64, which are not resolved in E6-MR but well represented in E6-XR (Fig. 3.10a), still contribute 20 % to total forcing in E6-XR (Fig. 3.10c).

Integrated from 10 to 2 hPa, the easterly forcing due to waves up to wave number 20 in ET-T63 and E6-XR amounts to 99 and 80 %, of the wave forcing, respectively (Fig. 3.10b, d) and is larger in E6-XR than in E6-MR. At these wave numbers, the forcing is

almost entirely due to the horizontal divergence of the horizontal EP-flux (not sown). The contribution from waves with wave numbers larger than 21 is negligible in E6-MR. (Fig. 3.10d). In E6-XR, waves with wave numbers ranging from 21 to 63 and 64 to 255 each contribute roughly 10 % to the wave momentum balance. Hence, the stronger deceleration of the QBO westerly jet between 10 and 2 hPa in E6-XR compared to E6-MR is mostly due to the better representation of the waves with wave numbers between 0 and 64 (Fig. 3.10b, d).

Using a model truncated at T205 wit 255 vertical levels, Kawatani et al. (2010a), showed that waves with wavenumbers ranging from 107 to 213 impose the same forcing on the QBO westerly jet as waves with wave numbers ranging from 43 to 106. For E6-XR, Figure 3.10a shows that despite the larger zonal resolution applied in Kawatani et al. (2010a), waves with wave numbers between 120 and 255, a range which overlaps with the range of wavenumbers still important in Kawatani et al. (2010a), contribute only little to the forcing of the QBO westerly jet. A direct comparison of both models is not possible at this point, so whether E6-XR has too weak wave sources at high wave numbers or too little vertical resolution to support small scale waves with

When calculating the wave number-frequency spectrum of the EP-flux according to Equations (3.6) and (3.7), the coarse temporal resolution of 1 sample every 6 hours in E6-XR limits the analysis of the resolved wave spectrum to waves with frequencies lower than 2 cycles per day. However, at large wave numbers, the EP-flux increases with increasing frequency (not shown). Hence, when integrating the EP-flux spectra over all frequencies, the integrated value is too low.

3.6 Conclusion

This study investigated the sensitivity of the Quasi-Biennial Oscillation to the tropospheric wave spectra. For this purpose, AMIP-type simulations conducted with ECHAM6 with spectral truncation at T63 and T255 and a vertical resolution of 700 m were performed.

The period of the QBO like oscillation in E6-XR is 7 months shorter than in E6-MR. In the upper stratosphere, the faster QBO phase progression in E6-XR is due to stronger resolved wave forcing. Considering resolved waves, the high resolution version has three advantages over the low resolution version. First, the tropical wave sources in E6-XR are stronger than in E6-MR over the whole range of zonal wave numbers resolved in both models. Second, due to the higher spectral resolution, the diffusive wave damping in the absence of critical levels in E6-XR is weaker than in E6-MR. Hence, the forcing of the QBO jets due to waves with wave numbers ranging from 20 to 64 is stronger in E6-XR. Third and most obviously, the larger spectral resolution in E6-XR adds zonal wave momentum due to previously unresolved waves.

In E6-XR, the QBO jets alternate with a higher frequency than in E6-MR and hence, there is less time to build up easterly or westerly momentum at a specific altitude. Consequently, the amplitude of the QBO in E6-XR is weaker than in E6-MR. In the lower stratosphere, both models have the same rate of change of momentum over most

of the quasi-biennial cycle, as the surplus of resolved waves in E6-XR is balanced by the reduction of the parametrized wave drag. As the forcing is equal in both model versions, the faster phase progression in E6-XR can only be explained by the weaker amplitude of the oscillation. The harmonic oscillation of a mathematical pendulum helps to understand this circumstance. Every pendulum is driven by the constant gravitational force, which corresponds to the equal momentum tendency in E6-XR and E6-MR. However, decreasing the length of the pendulum's string shortens the segment of the circle swept by the pendulum, which corresponds to the weaker amplitude of the QBO jets. In both examples, the outcome is a shorter period of the oscillation.

The frequency of the model output in the high resolution run, which is once every 6 hours, limits the analysis of the wave forcing to waves with frequencies lower than 2 cycles per day. Therefore the analysis underestimates the wave drag due to waves with wave numbers larger than 100, which have the largest EP-flux at frequencies higher than 2 cpd.

In ECHAM6, the zonal wind tendency at the zero wind line associated with the onset of the QBO jets is stronger than in ERA-Interim, which is compensated by weaker forcing away from the zero wind line and weaker QBO easterly jets in the lower stratosphere. Thus, compared to ERA-Interim, the QBO period in E6-MR is only three months too short. However, both ECHAM6 versions overestimate the QBO amplitude in the upper stratosphere. The differences in the QBO structure and QBO forcing could be due to differences in the wave forcing. However, contrary to the zonal wind, the wave forcing is not represented realistically in ERA-Interim. To gain clarity about the magnitude of the individual forcing terms of the QBO, one has to find the wave field and the equatorial upwelling which leads to the internal generation of a QBO like oscillation with a realistic period and amplitude in high resolution models resolving the wave forcing. Currently, such efforts are being made by gradually reducing the parametrized wave drag in the high resolution ECHAM6 to obtain the observed QBO period.

Chapter 4

Seasonal Modulations of the Quasi-Biennial Oscillation in MPI-ESM and ERA-40[1]

Abstract This study investigates seasonal modulations of the quasi-biennial oscillation (QBO) of the tropical stratosphere. For this purpose, the Max Planck Institute Earth System Model (MPI-ESM), which internally generates a realistic QBO compared to the ERA-40 dataset, is employed. The modeled QBO is forced with resolved and parametrized waves. At 5 hPa, the seasonal distribution of the onset of QBO westerly jets clusters in spring and fall due to the coupling of the QBO and the semi-annual oscillation . This seasonal clustering of the westerly jets extends throughout the stratosphere, shifting to later months with increasing pressure. QBO westerly jets starting in the upper stratosphere in fall propagate to the middle stratosphere more slowly than westerly jets starting in spring. This is attributed to seasonal modulations of the QBO forcing and enhanced wave filtering by the QBO westerly jet in the lower stratosphere in fall and winter compared to spring and summer. The observed stalling of the QBO easterly jet in the lower stratosphere and the accompanied prolonged persistence of the QBO westerly jet in the vicinity of the tropopause are attributed equally to seasonal variations of the resolved and parametrized wave forcing and the advective forcing.

4.1 Introduction

In the tropical stratosphere, the variability of the zonal mean zonal wind is dominated by the well known Quasi Biennial Oscillation (QBO). It manifests most clearly in the oscillation of westerly and easterly jets which originate in the upper stratosphere, propagate downwards to the vicinity of the tropical tropopause and alternate with a quasi-biennial period between 22 and 34 months (Baldwin et al., 2001). For this paper, a global climate model internally generating a realistic QBO is applied to investigate

[1]Published as Krismer, T. R., Giorgetta, M. A., and Esch, M. (2013). Seasonal aspects of the quasibiennial oscillation in MPIESM and ERA40. Journal of Advances in Modeling Earth Systems, doi:10.1002/jame.20024

seasonal aspects of the QBO, namely, the coupling of the QBO to the Semi-Annual Oscillation in the vicinity of the stratopause, the clustering of the QBO phase onsets at specific times of the year as a function of altitude and the seasonal modulation of the propagation rates of the QBO jets.

In observational data, Dunkerton and Delisi (1985) and Dunkerton (1990) found that the onsets of the westerly and easterly jets of the QBO at 50 hPa have a seasonal preference, both clustering in northern hemisphere spring and summer. At higher altitudes, the preferred season shifts to earlier months (Dunkerton, 1990; Anstey and Shepherd, 2008). The month a QBO jet starts at a specific level is related to the month of the year the jet began in the upper stratosphere and the rate at which it propagates downward. Wallace et al. (1993), Hamilton and Hsieh (2002) and Lu et al. (2009) documented that integrated from 10 to 70 hPa, the QBO phases progress more rapidly in boreal winter and spring than in summer and fall. Between 30 and 50 hPa the descent of the easterly jet often slows down, and easterly and westerly jets stall for several months from July to February (Naujokat, 1986; Dunkerton, 1990; Pascoe et al., 2005).

In idealized numerical studies, seasonal variations of the QBO phase propagation have been related to a seasonal cycle of the equatorial upwelling (Kinnersley and Pawson, 1996; Hampson and Haynes, 2004). Seasonal variations of the equatorial- and gravity wave activity and hence, the QBO momentum sources, also have the potential to alter the propagation rates (Dunkerton, 1990). Such variations have been observed by Allen and Vincent (1995), Fritts and Alexander (2003) and Li et al. (2010), but their influence on the QBO has not been investigated further.

Another interaction of the annual cycle with the QBO emerges from the interaction of the quasi-biennial oscillation and the semi-annual oscillation (SAO) that occurs directly above the QBO. In the original theory of the QBO presented by Lindzen and Holton (1968), the SAO provides the westerly shear in the upper stratosphere, which is needed for effective deposition of westerly momentum by atmospheric waves. Holton and Lindzen (1972) introduced radiative wave damping as a dissipation mechanism for vertically propagating waves and found that the SAO was no longer needed to create the QBO. Plumb (1977) showed that in such a model, however, the evolution of the mean flow at any particular level is independent of what happens above, and downward influence is impossible if vertical diffusion is negligible. Numerical studies (Gray and Pyle, 1989; Dunkerton and Delisi, 1997; Mayr et al., 2010) illustrated the evolution of a QBO-like wave driven oscillation with and without a coupling to the SAO. Kuai et al. (2009) identified the initialization of QBO westerly jets by the SAO in the ERA-40 dataset.

From the seasonal aspects of the QBO discussed above, the following questions discussed in this paper arise:

1. How does the interaction of the QBO and the SAO influence the phase alignment of the QBO jets in the upper stratosphere and how does this phase alignment project to lower altitudes?

2. How does the seasonal stalling of the QBO jets in the lower stratosphere influence the propagation rates of the jets in the upper stratosphere?

3. How do seasonal variations of the equatorial wave forcing and the tropical upwelling contribute to variations of the propagation rates of the QBO jets?

To explain the interaction of the annual cycle with the QBO, it is necessary to understand its forcing mechanism. The QBO is driven by vertically propagating atmospheric waves which deposit easterly and westerly momentum due to radiative attenuation, critical layer absorption and wave breaking (Lindzen and Holton, 1968; Holton and Lindzen, 1972). The wave attenuation is most effective where the zonal phase speed of a wave is close to the zonal wind speed. Waves which deposit their wave momentum around the zero wind line between easterly and westerly jets drive the zero wind line downwards, towards the wave sources. However, the tropical upwelling in the stratosphere, which is driven by extra-tropical wave activity, tends to move stratospheric air upwards, and thus works against the downward propagation of the QBO jets (Dunkerton, 1997). Through a long history of observational and modeling studies, large scale equatorial and extra-tropical waves, small scale gravity waves and vertical advection are recognized as the main forcing factors of the QBO (Baldwin et al., 2001; Giorgetta et al., 2006; Kawatani et al., 2010a; Evan et al., 2012b).

Most modeling studies addressing seasonal aspects of the QBO investigate the influence of a prescribed variation of the vertical velocities on QBO-like oscillations within simplified models (Kinnersley and Pawson, 1996; Hampson and Haynes, 2004). In this respect, an investigation within the setting of a global climate model (GCM) is still missing. It is desirable to generate a realistic QBO within GCMs because of the influence of the QBO on the extra-tropical climate (Holton and Tan, 1980; Hamilton and Hsieh, 2002; Anstey and Shepherd, 2008). GCMs embed the QBO into their global circulation where the variability of the resolved wave forcing and the equatorial upwelling is internally generated, and thus consistent with the simulated climate. This sets a realistic setting, within which variations of the QBO can be investigated.

Over the last decade, general circulation models (GCM) have developed the skill to internally generate QBO-like oscillations (Takahashi, 1999; Scaife et al., 2000; Giorgetta et al., 2002; Kawatani et al., 2010a). High vertical resolution is required to simulate a QBO (Giorgetta et al., 2006; Kawatani et al., 2010a). The number of GCMs generating a QBO is still limited, and modeled QBOs often show systematic biases in structure, amplitude or period. Nevertheless modeled QBOs result from the ability of models to capture the essential wave-meanflow interaction.

The investigation of the annual modulation of the QBO presented here is based on a 500 year long simulation of the Max Planck Institute Earth System Model (MPI-ESM) which generates a realistic QBO. In Section 4.2, a brief description of the climate model MPI-ESM is given. General aspects of the simulated QBO are discussed in Section 4.3. Section 4.4 describes how the interaction of the QBO and the SAO influences the phase alignment of the QBO jets in the upper stratosphere. The influence of seasonal variations of the QBO forcing on the propagation of the QBO jets in the upper stratosphere and on the stalling of the QBO jets in the lower stratosphere are discussed in Section 4.5 and 4.6. Section 4.7 discusses the phase alignment of the QBO jets in the middle stratosphere, and a summary is given in Section 4.8.

4.2 Model, Experiment and Methods

This work makes use of the Max Planck Institute Earth System Model (Giorgetta et al., 2013b), which consists of the ECHAM6 atmospheric GCM (Stevens et al., 2012), the JSBACH land vegetation model (Raddatz et al., 2007) and the MPIOM ocean GCM (Marsland et al., 2003) including the HAMOCC ocean bio-geochemistry model. For brevity, the generic name MPI-ESM is used in the following text. Here, the MPI-ESM-MR configuration is used, where "MR" designates the resolution of atmosphere and ocean GCMs. The ocean model makes use of a tripolar grid with a nominal resolution of 0.4°. The vertical grid has 40 z levels. The atmospheric component ECHAM6 is the direct successor of MAECHAM5, which is capable of internally generating a realistic QBO in terms of its periodicity, amplitude and vertical and latitudinal structure (Giorgetta et al., 2002, 2006; Peña Ortiz et al., 2008, 2010). ECHAM6 generates an equally realistic QBO as MAECHAM5. In the "MR" configuration, ECHAM6 uses a spectral truncation at wave-number 63 and an associated Gaussian grid of approximately 1.9° resolution in longitude and latitude. The vertical grid has 95 hybrid sigma pressure levels resolving the atmosphere from the surface up to the center of the uppermost layer at 0.01 hPa. The top-of-the-model pressure is defined as 0 hPa. This grid has a nearly constant vertical resolution of 700 m from the upper troposphere to the middle stratosphere, and the resolution is better than 1 km at the stratopause. Thus the vertical grid is overall comparable to that used by Giorgetta et al. (2006) with respect to the vertical resolution in the QBO domain.

The parametrization of sub-grid scale convection, which is known to influence the resolved wave field, follows the Tiedtke-Nordeng scheme (Tiedtke, 1989; Nordeng, 1996). ECHAM6 includes the Hines parametrization for non-orographic gravity waves (Hines, 1997a,b). The parametrized wave source is at 700 hPa. The source spectrum of the Hines parametrization follows the MAECHAM5 standard setting (Manzini and McFarlane, 1998; Manzini et al., 2006). However, the otherwise constant wave-induced horizontal wind perturbations (rms winds) increase linearly from 1 to 1.2 m/s over 10°N to 5°N (10°S to 5°S). From 5°N to 5°S, the rms winds are constant at 1.2 m/s. The modification of the Hines parametrization was necessary to obtain a realistic QBO in MPI-ESM, where ECHAM6 is coupled to an ocean model. In MPI-ESM, the increase of the rms winds results in a four times larger wave momentum deposition in the domain of the QBO, given comparable wind profiles and wind shear in the stratosphere. Giorgetta et al. (2006) showed that increasing (decreasing) the rms winds in MAECHAM5 by 10 % strengthens (weakens) the QBO westerly jets and reduces (increases) the period. With an idealized one dimensional model, Scaife et al. (2000) showed that the QBO period generally decreases with increasing parametrized wave sources. For MPI-ESM, the applied equatorial strengthening of the rms winds meets the need for technically simple changes of the parametrization and, as shown below, a realistic QBO. Given the lack of observational constraints on tropical gravity waves and considering that the mostly convective non-orographic wave sources, which the Hines scheme mimics, are more abundant in the tropics than in the extra-tropics, such an enhancement seems to be justified. The parametrized gravity wave sources are constant in time.

MPI-ESM has been used for many CMIP5 simulations (Taylor et al., 2009), and an

overview over the dynamics of the middle atmosphere in these simulations is given by Schmidt et al. (2012b). This study makes use of the pre-industrial CMIP5 simulation, which is forced by 1850 conditions and was integrated over 500 years (Giorgetta et al., 2012). The 500 simulated years include 209 complete quasi-biennial cycles, which allows us to calculate sound statistics of the discussed QBO features.

In this study, the forcing of the QBO jets will be discussed within the framework of the Transformed Eulerian Mean (TEM) equations (Andrews et al., 1987). Within this framework, the zonally averaged momentum equation states:

$$\begin{aligned} \bar{u}_t &= \bar{v}^* \left[f - (a\,cos\phi)^{-1} (\bar{u}\,cos\phi)_\phi \right] - \bar{w}^* \bar{u}_z + \\ &\quad (\rho_0\, a\, cos\phi)^{-1} \nabla \cdot F + \bar{X} \end{aligned} \tag{4.1}$$

where ρ_0 is the log-pressure height-dependent density, a is the Earth radius and ϕ and z are the latitude and the log-pressure height. $\bar{u}$ is the zonal mean zonal wind and $\bar{v}^*$ and $\bar{w}^*$ are the meridional and vertical residual mean winds. f is the Coriolis parameter ($f \equiv 2\Omega\, sin\phi$ and Ω is the rotation rate of the Earth). Subscripts ϕ, z and t denote the meridional, vertical and temporal derivatives. $\bar{X}$ represents unresolved forcing terms.

The non-orographic gravity wave drag and horizontal and vertical diffusion contribute to $\bar{X}$. However, these terms have not been stored for the CMIP5 simulation presented here. Therefore, $\bar{X}$ is computed according to Equation (4.1) as the difference of the total acceleration minus the sum of the advective terms and the resolved wave forcing. To investigate the composition of $\bar{X}$, the first 30 years of the MPI-ESM pre-industrial run have been repeated and the parametrized wave drag and the diffusion terms have been stored. Comparing the forcing terms showed that the parametrized wave drag dominates the total residuum, thus making $\bar{X}$ a good approximation for the parameterized gravity wave drag.

∇·F denotes the vertical and meridional divergence of the Eliassen Palm Flux (EP-Flux), which is a measure of the transport and deposition of zonal momentum by atmospheric waves in the stratosphere (Andrews et al., 1987). In this study, F denotes the EP-Flux carried by waves resolved in MPI-ESM-MR with global wave numbers k ranging from 0 to 63. To distinguish the contribution of easterly and westerly waves to the atmospheric wave forcing, the zonal wave number/frequency distribution of the EP-Flux is computed following Horinouchi et al. (2003):

$$\begin{aligned} \frac{F^{(\phi)}(k,\omega)}{\rho_0\, a\, cos\phi} &= RE\left[\, \bar{u}_z \hat{v}(k,\omega) \hat{\theta}^*(k,\omega)/\bar{\theta}_z \right] - \\ &\quad RE\left[\, \hat{u}(k,\omega) \hat{v}^*(k,\omega) \right] \end{aligned} \tag{4.2}$$

$$\begin{aligned} \frac{F^{(z)}(k,\omega)}{\rho_0\, a\, cos\phi} &= RE\Big\{ \Big[f - \frac{(\bar{u}\,cos\phi)_\phi}{a\,cos\phi} \Big] \hat{v}(k,\omega) \hat{\theta}^*(k,\omega)/\bar{\theta}_z \Big\} - \\ &\quad RE\{ \hat{u}(k,\omega) \hat{w}^*(k,\omega) \} \end{aligned} \tag{4.3}$$

In Equations (4.2) and (4.3), θ is the potential temperature. A hat denotes the Fourier coefficients of the variables, whereas an asterisk denotes the complex conjugate. The Fourier coefficients have been derived by applying a Fast Fourier Transform in longitude and time for each month of the simulation separately, each month having six hourly data output. There is no temporal overlap between the months. k and ω denote the zonal wave number and frequency. The acceleration of the mean flow due to resolved waves with a certain phase speed is derived by summing the divergence of the spectral EP-Flux over bins of the same ground based phase speed c, which is related to k and ω via the relation $c(k, \omega)=\omega/k$:

$$\bar{u}_{t\,(\nabla \cdot F(c))} = \sum \frac{\nabla \cdot F(k,\omega)|_{\frac{\omega}{k}=c}}{\rho_0\, a\, cos\phi} \tag{4.4}$$

For the understanding of the QBO it is important to remember that the wave momentum deposition is strongest where the wind speed is close to the phase speed (Lindzen and Holton, 1968; Dunkerton and Fritts, 1984; Fritts and Alexander, 2003). The shear layer associated with a stronger QBO jet includes a larger range of velocities than the shear layer of a weaker jet. Hence, a broader spectrum of waves with larger phase speeds meet their critical level within the stronger shear zone. To a certain degree, this results in stronger wave momentum deposition and stronger acceleration of the mean flow.

4.3 The QBO in MPI-ESM

Figures 4.1a and c show the monthly mean zonal mean zonal wind in the tropical stratosphere and lower mesosphere over a 15 year period of the 500 year long MPI-ESM simulation and from 1984 to 1998 in the ERA-40 reanalysis dataset. Between 0.1 and 2 hPa, the easterly and westerly jets of the semi-annual oscillation dominate the zonal wind field. Between 5 and 100 hPa, westerly and easterly jets alternate with a quasi-biennial period. The QBO in MPI-ESM has the same range of periods between 24 and 34 months and the same mean period of 28.8 months as the QBO in ERA-40.

In MPI-ESM, the peak to peak amplitude of the QBO steadily increases from 100 to 10 hPa, where it reaches 70 m/s (Fig. 4.1b). Compared to ERA-40, the maximal QBO amplitude is roughly 50% stronger and higher up in the stratosphere.

Consistent with the ERA-40 dataset, the semi annual oscillation becomes important above 7 hPa in MPI-ESM (Fig. 4.1b). Again, in MPI-ESM, the peak amplitude of the SAO is stronger (50 compared to 40 m/s) and higher up in the stratosphere (1 compared to 2 hPa) than in ERA-40. Above 10 hPa, no wind observations are assimilated into the ERA-40 reanalysis system to constrain the QBO and the SAO, which then are internally generated above that altitude. However, Baldwin (2005) showed that the amplitude of the QBO in ERA-40 generally compares well to rocket- and rawisonde data, and that the QBO and the SAO are well represented up to 3 hPa. Based on this, the QBO and the SAO are too strong in MPI-ESM.

The QBO dominates the stratospheric variability between 100 and 10 hPa, which is in accordance with ERA-40 (Fig. 4.1d). The QBO explains about 90% of the variance of the zonal wind on the QBO core levels in MPI-ESM, but only about 80% in ERA-40 (Fig. 4.1d). Because of the stronger QBO, the contribution of the SAO to the total variance is weaker in MPI-ESM than in ERA-40, except for a narrow region from 1 to 0.5 hPa, where the SAO is equally important in both datasets (Fig. 4.1d). Above 0.5 hPa, the amplitude and the relative variance of the QBO increase in MPI-ESM due to the mesospheric QBO (Peña Ortiz et al., 2010), which is not covered in ERA-40 (Fig. 4.1b, d).

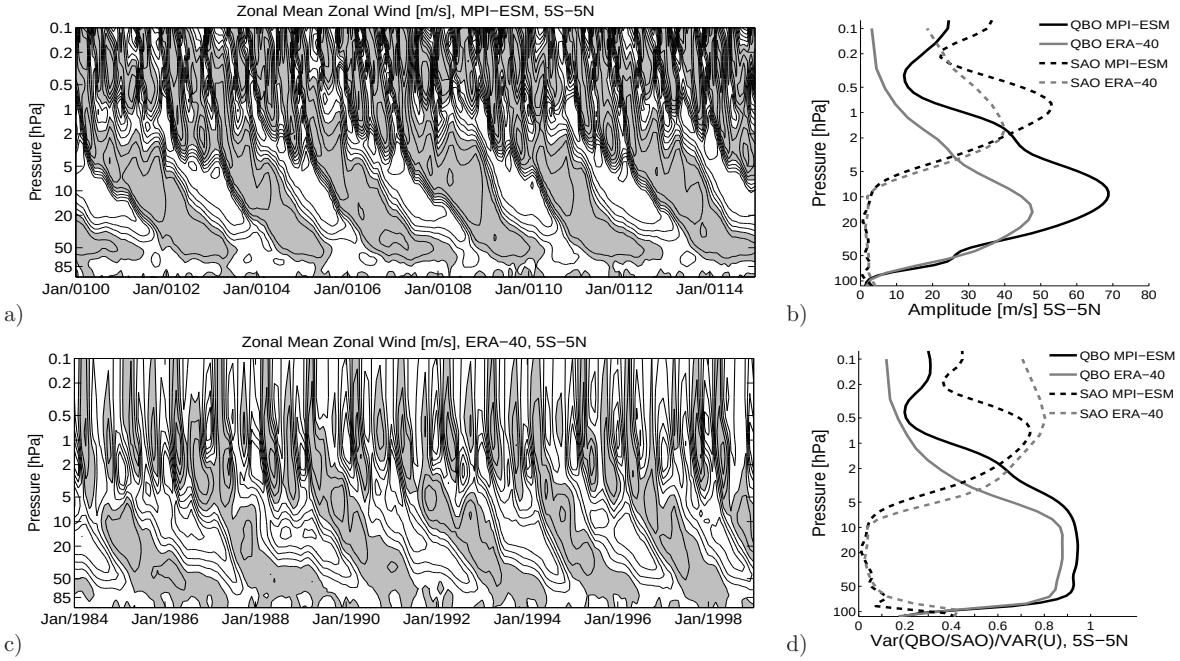

Figure 4.1: a) and c): Time-height cross section of the zonal mean zonal wind in (a) MPI-ESM and in (c) ERA-40. The contour interval is 10 m s^{-1}. Positive wind speeds are highlighted in gray. b): Profiles of the peak to peak zonal wind amplitude of the QBO (solid) and the SAO (dashed) in MPI-ESM (black) and ERA-40 (gray). d): Profiles of the zonal wind variance of the QBO (solid) and the SAO (dashed) relative to the total zonal wind variance in MPI-ESM (black) and ERA-40 (gray). Spectral filters with band passed periods of 20 to 35 and 6 months have been used to isolate the signal of the QBO and the SAO, respectively.

4.4 QBO/SAO Coupling

The SAO and the QBO overlap above 5 hPa (Fig. 4.1). The interaction between both oscillations is illustrated in Figures 4.2a and c, which show composites of the zonal mean zonal wind and the deseasonalized zonal mean zonal wind in MPI-ESM and ERA-40. The composites consist of only those quasi-biennial cycles where the onset of the westerly jet in the deseasonalized wind at 5 hPa (month 0) occurs in May for MPI-ESM and in June for ERA-40. These are the months when the onsets are most frequent in the respective dataset (shown below). At 5 hPa, the deseasonalized and

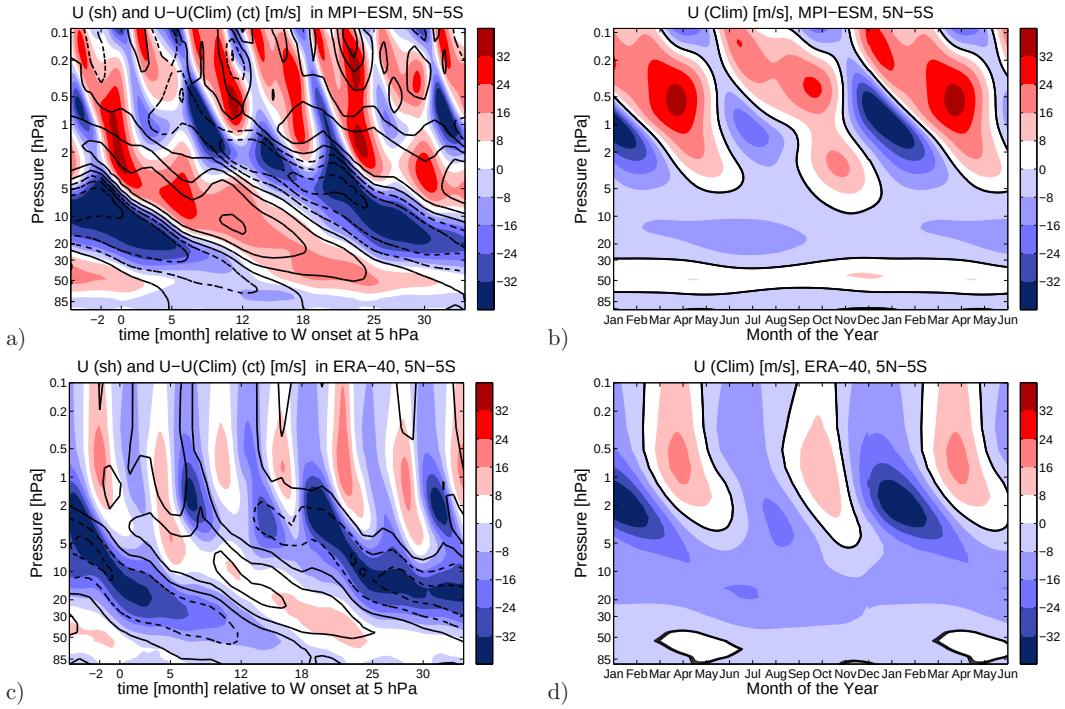

Figure 4.2: a) and c): Time-height cross section of the composite of the zonal mean zonal wind U (shading) and the zonal wind after subtracting the annual climatology U-U(clim) (contours) in (a) MPI-ESM and in (c) ERA-40. The contour interval is 10 m s^{-1}. The zero-wind line and positive wind speeds are solid, negative winds speeds are dashed. The central date (month 0) refers to the onset of the QBO westerly jets in the deseasonalized zonal wind at 5 hPa in May for MPI-ESM and in June for ERA-40. b) and d): Time-height cross section of the climatological zonal mean wind U(clim) in (b) MPI-ESM and in (d) ERA-40. The black line indicates the zero-wind line.

the full zonal wind coincide well in MPI-ESM, while in ERA-40, the QBO westerly jet starts 5 months earlier in the deseasonalized than in the full zonal wind (month 0 and 5 of Fig. 4.2c). Punge and Giorgetta (2007) found that in ERA-40, the zonal wind speed is systematically weaker by 10m/s in the first half of the dataset, probably due to a lower quality of the zonal wind observations during the early years of ERA-40. Deseasonalizing the full zonal wind partly removes the offset, which does not affect the QBO amplitude (Punge and Giorgetta, 2007).

The QBO westerly jet in the zonal wind becomes weaker as it propagates from the upper stratosphere to lower altitudes (Fig 4.2a, c). It becomes more permeable for waves transporting westerly momentum, as fewer waves encounter their critical level, where the phase speed is close to the wind speed (Ern et al., 2011; Yang et al., 2012). Thus, more westerly momentum can reach the upper stratosphere when a relatively weak QBO westerly jet exists in the lower stratosphere than when a stronger QBO westerly jet is in the middle stratosphere. Consequentially, the SAO westerly jet is forced more strongly and can propagate to lower altitudes in the stratosphere at times of a weaker and lower QBO westerly jet (Fig. 4.2a, month 5, 12, 18 and 25). The same considerations are true for the SAO and QBO easterly jets. This dependence of the SAO on the QBO is shown by MPI-ESM and ERA-40, and is in agreement with

results from earlier observational and modeling studies (Dunkerton and Delisi, 1997; Garcia et al., 1997; Scaife et al., 2000; Giorgetta et al., 2006; Peña Ortiz et al., 2010).

In MPI-ESM, the QBO is coupled to the SAO in such a way that at 5 hPa, every QBO westerly shear zone directly connects to a SAO westerly jet. A SAO westerly jet continues as a westerly jet of the QBO after every 4 to 6 semi annual cycles (month 0 and 29 in Fig. 4.2a), when the westerly jet of the previous quasi-biennial cycle, located between 30 and 80 hPa in month 0 of Figure 4.2a, is weak and permeable for a sufficient amount of westerly waves.

For ERA-40, Figure 4.2c shows that the westerly jet of the deseasonalized zonal wind (contours) starts at 5 hPa 5 months earlier than the jet in the actual zonal wind (shading). As found by Dunkerton (1997) and Kuai et al. (2009), the onsets of both jets coincide well with the descent of an SAO westerly phase. However, for the westerly jet of the actual zonal wind this is not always the case, as shown by the jet evolving at 5 hPa in 1985 and 1987 in Figure 4.1c (and a number of westerly jets in earlier years).

In ERA-40, the amplitude of the SAO is larger than the amplitude of the QBO above 5 hPa (Fig. 4.1b). In month 1 to 4 of Figure 4.2c between 5 and 1 hPa, the overlap of the QBO westerly phase in the deseasonalized wind with easterly winds in the actual wind illustrates that the SAO easterly jet masks the QBO westerly phase in the actual wind. Hence, the coupling of the QBO westerly jet to the SAO becomes more obvious when comparing the phase of the SAO with the onset of a QBO westerly jet in the deseasonalized zonal wind.

The climatologies of the zonal wind in the stratosphere in MPI-ESM and ERA-40 are shown in Figure 4.2b and d. Both datasets show a seasonal asymmetry with a stronger semi-annual cycle with maximal westerly winds at 0.5 hPa in March/April and a weaker semi-annual cycle with maximal westerly winds at 0.5 hPa in September/October. This asymmetry is well observed and associated with stronger meridional momentum advection in boreal winter (Delisi and Dunkerton, 1988). Also the composite in Figure 4.2a shows this asymmetry, as the SAO westerly jet at 0.5 hPa is stronger in April (month 11 and 23) than in October (month 17).

A comparison of the zonal wind climatology and the seasonal distribution of the onset of QBO westerly jets in the upper stratosphere gives evidence of the initialization of the QBO westerly phase by SAO westerly jets. At 1 hPa in the simulation and the reanalysis data, the onset of the climatological SAO westerly jets occurs in mid February and mid August (Fig. 4.2b, d). The jets reach 5 hPa some months later around May and October. These months mark the onset of a QBO westerly jet at 5 hPa if the SAO westerly jet continues its decent as a westerly jet of the QBO. This coupling displays in the seasonal distribution of the onsets of the QBO westerly jets in the upper stratosphere shown in Figure 4.3. In MPI-ESM, the onset of the 209 QBO westerly jets at 5 hPa occurs mainly in spring (April/May/June) and in fall (September/October/November), with two distinct peaks in May and in October and few occurrences from December to March (Fig. 4.3a). In the deseasonalized zonal wind in MPI-ESM and ERA-40, the onset of the QBO westerly jet clusters at 5 hPa from April to June (Fig. 4.3b and c). A second cluster extends from October to December in MPI-ESM and from September to November in ERA-40 (Fig. 4.3b and

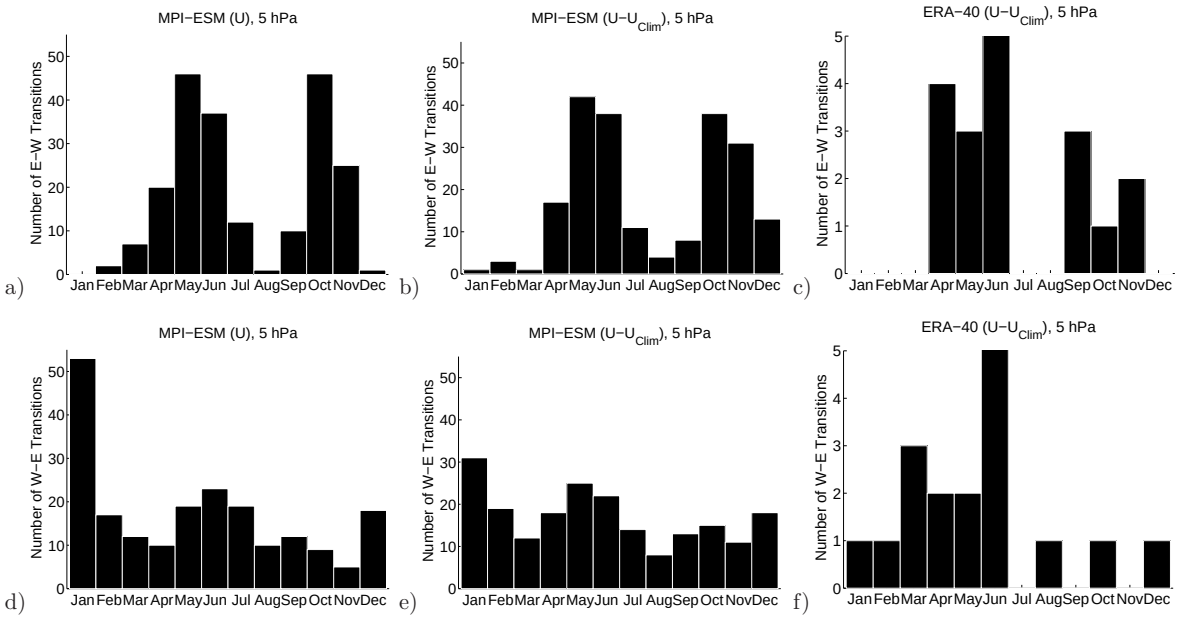

Figure 4.3: Monthly distribution of the onset of the QBO westerly (upper panel) and easterly jet (lower panel) at 5 hPa in the zonal mean wind (U) in (a, d) MPI-ESM and in the deseasonalized zonal wind (U-U$_{Clim}$) in (b, e) MPI-ESM and (c, f) ERA-40.

c). This similar clustering illustrates the good agreement on the coupling of the onset of a QBO westerly phase to the descent of an SAO westerly jet between the model and the reanalysis dataset.

The seasonal distribution of the onset of the easterly jets at 5hPa in MPI-ESM shows some clustering in December/January and from May to July (Fig. 4.3d). During these months, the SAO is in its easterly phase at 5 hPa (Fig. 4.2b). However, the distribution is much broader than the distribution of the onset of the westerly jets (Fig. 4.3a). Although easterly jets are initiated and strengthened by the easterly phase of the SAO above 5 hPa, their occurrence is not limited to it. Once initiated, the easterly jets are not replaced by SAO westerly jets because the QBO westerly jet below filters the necessary westerly wave momentum flux (month 5 and 12 in Fig. 4.2a). The easterly jet is sustained by weak easterly forcing, which increases during SAO easterly phases and as the QBO easterly jet in the lower stratosphere weakens (Peña Ortiz et al., 2010). Because the easterly jet prevails continuously and not only during SAO easterly phases, it can pass 5 hPa and mark the onset of a QBO easterly jet throughout the year.

In ERA-40, the onset of the deseasonalized easterly jets is confined to the period from January to June, contrary to the broad distribution shown by MPI-ESM (cf. Fig. 4.3e and f). Sub sampling successive 40 year long periods of the 500 year long MPI-ESM simulation revealed that there are periods when the distribution is more peaked. However, such periods are rare. Because of the weak seasonality of the onset of the QBO easterly jet in MPI-ESM, the focus of this study lies on the QBO westerly jet.

4.5 Propagation of QBO jets through the middle stratosphere

The different propagation characteristics of the QBO westerly jets starting at 5 hPa in spring and fall in MPI-ESM and ERA-40 are discussed next. Therefore, two composites of quasi-biennial cycles where the westerly jets pass 5 hPa either in April or May or in October or November are computed. For MPI-ESM, the actual zonal wind is considered for these composites, which include 66 and 71 samples in spring and fall, respectively. However, as noted in the discussion of Figure 4.2c, the QBO westerly jet of the actual wind in ERA-40 often is masked by an SAO easterly jet. Hence, in ERA-40 it is more convenient to create the composites based on the onset of the QBO westerly jet in the deseasonalized zonal wind, which include 7 and 3 samples for April/May and for October/November, respectively.

Figure 4.4 shows the time-height cross section of the zonal mean zonal wind and its acceleration in the composites. Figure 4.4a and c shows that the QBO westerly jets starting at 5 hPa in spring propagate quickly to the middle stratosphere and the forcing along the zero-wind line, which separates the upper QBO westerly jet and the easterly jet below, is continuously high. However, westerly jets starting at 5 hPa in fall experience a period of almost zero-acceleration at 7 hPa from December/January to February/March (Fig. 4.4b, d), and

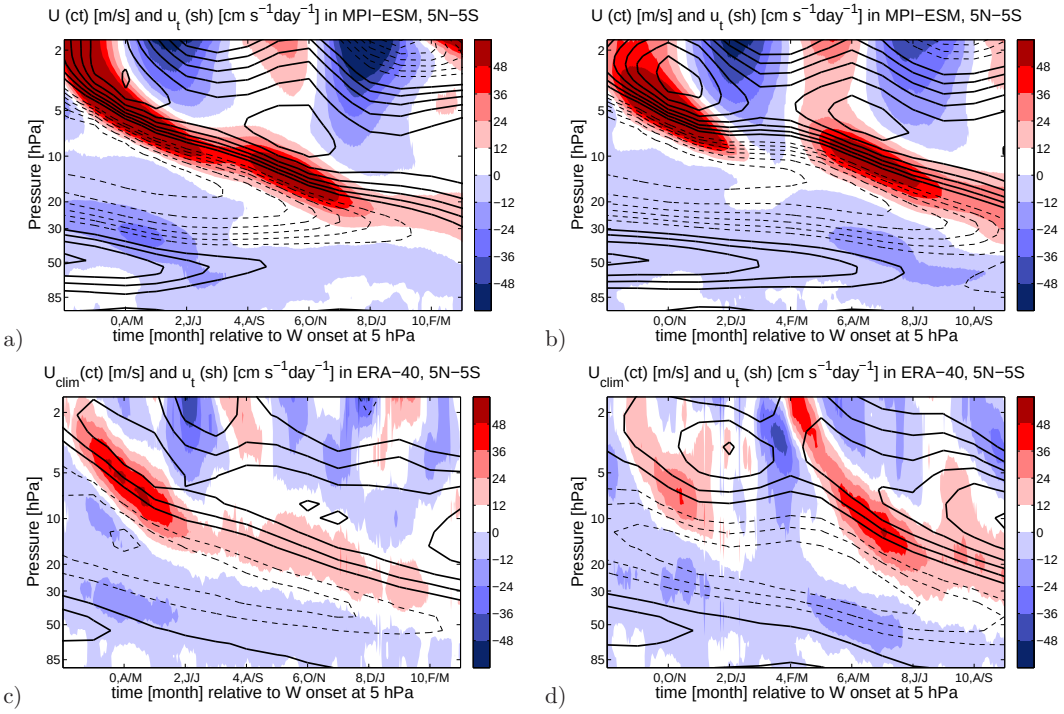

Figure 4.4: Time-height cross section of the composites of the zonal mean zonal wind (contour) and its acceleration (shading) in (a, b) MPI-ESM and the desasonalized zonal wind in (c, d) ERA-40. The contour interval is 5 m/s. The zero-wind line and positive wind speeds are solid, negative wind speeds are dashed. The central date (month 0) refers to the onset fo the QBO westerly jets at 5 hPa in (a, c) April or May or in (b, d) October or November.

hence, stall in their vertical propagation during this period. Thereafter, the mean flow acceleration increases again, and the westerly jet propagates to lower altitudes. Next, the cause of this stalling is discussed in the context of the momentum equation (Eq. 4.1).

In the GCM used for ERA-40, the QBO is generated through the assimilation process. An additional term enters the momentum balance (Eq. 1) which accounts for the assimilation increments and which has not been reported. As the QBO does not emerge from the freely running model, it has to be doubted that the model generated terms of the momentum balance in ERA-40 are sufficient to drive the QBO. As such an investigation is beyond the scope of this study, the stratospheric momentum budget is discussed only for MPI-ESM.

Figure 4.5 shows profiles of the zonal wind and the terms of Equation 4.1 for MPI-ESM in month 2 of the composites of QBO westerly jets initiated in spring (labeled June/July) and fall (labeled December/January) in MPI-ESM. The zonal wind profiles in Figure 4.5 show an upper QBO westerly jet starting at 7 hPa, a lower-level QBO westerly jet with its core at 50 hPa and an easterly jet in between. Such a threefold wind profile has also been found by Pascoe et al. (2005). Figure 4.5 illustrates that the stronger parametrized wave forcing and the stronger vertical momentum advection around 7 hPa (Fig. 4.5c, d) are responsible for the stronger total forcing of the upper QBO westerly jet in June/July compared to December/February (Fig. 4.5a, cf. Fig. 4.4a and b). The difference in the advective forcing (Fig. 4.5d) is due to the annual cycle of the equatorial upwelling. It is weak in June/July, when its extra-tropical Rossby-Waves forcing is low. Hence, in June/July the downward motion induced by the upper QBO westerly jet results in stronger momentum advection than in December/January (Fig. 4.5d). Note that in MPI-ESM, the secondary circulation induced by the QBO westerly jet at high altitudes is strong enough to turn the generally upward equatorial vertical motion downwards, and the momentum advection is positive below the upper QBO westerly jet.

In MPI-ESM, the parametrized wave sources are kept constant in time. Therefore, the difference of the parametrized wave forcing of the upper QBO westerly jet at 7 hPa in Figure 4.5c is due to stronger filtering of the parametrized waves between the wave sources at 700 hPa and the upper stratosphere in December/January compared to June/July. A part of this filtering is done by the QBO westerly jet in the lower stratosphere, located between 80 and 30 hPa in Figures 4.4 and 4.5 (called lower-level westerly jet hereafter). The lower-level westerly jet is stronger in December/January than in June/July (Fig. 4.5). Hence, more parametrized westerly waves meet their critical level, where their phase speed is close to the zonal wind speed, and give their momentum to the mean flow. The structure of the lower-level westerly jet is also important for resolved waves. In December/January, resolved westerly waves (phase speed $c>0$) deposit roughly twice the momentum between 100 and 50 hPa than in June/July (Fig. 4.5b). However, despite the strong filtering in the lower stratosphere in December/January, the peak of the resolved wave forcing of the upper QBO-westerly jet around 7 hPa is only shifted upwards by one model level and not significantly different compared to June/July (Fig. 4.5b). The stronger resolved wave filtering at lower altitudes in December/January is compensated by a seasonal strengthening of

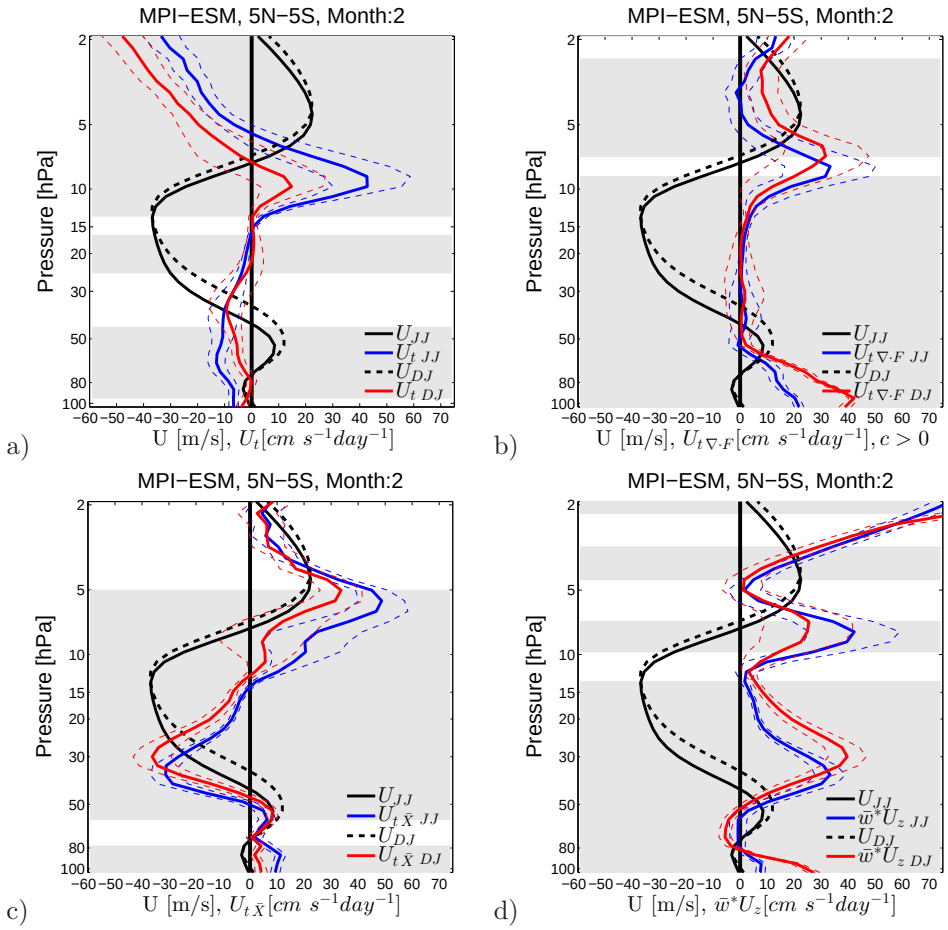

Figure 4.5: Profiles of the zonal mean zonal wind (m s^{-1}) two months after the onset of the QBO westerly jet at 5 hPa in April/May (JJ, solid black) or October/November(DJ, dashed black). The blue and red lines show (a) the respective total acceleration of the zonal wind $\bar{u}_t$, (b) the acceleration due to the resolved EP-Flux divergence from westerly waves $\bar{u}_{t\nabla\cdot F}$ (c>0), (c) the parametrized wave drag and diffusion $\bar{u}_{t\bar{X}}$ and (d) the vertical momentum advection $\bar{w}^*\bar{u}_z$ in cm s^{-1}day $^{-1}$. The gray background indicates a statistical significant difference between the compared forcing. Dashed lines indicate ± one standard deviation.

the resolved westerly waves entering the stratosphere in winter (discussed below).

4.6 Evolution of QBO jets in the lower stratosphere

The difference between the structure of the lower-level westerly jets in month two of the composites in Figure 4.4 and Figure 4.5 becomes more pronounced in later months (not shown). This is due to quick dissipation of the lower-level westerly jet in spring and summer (Fig. 4.4a, c) compared to its prolonged persistence in fall and winter (Fig. 4.4b, d). To which extent seasonal variations of the QBO forcing contribute to the different evolution of the lower-level QBO westerly jet is discussed next, again in the context of the momentum equation (Eq. 1). However, a new set of composites has to be computed, because the weakening of the lower-level westerly jet causes a negative feedback on its forcing, as the slower jet less efficiently absorbs momentum

transported by westerly waves. Sampling months with similar zonal wind profiles in the lower stratosphere excludes the dynamic feedback of the forcing and the flow and allows to discuss the seasonal variability of mean flow acceleration for a given zonal wind profile.

Here, this sample consists of months when the zero-wind line between the lower-level westerly jet and the easterly jet above lies at 33 hPa. To create this sample, it has been checked in which pare of months the zonal wind at 33 hPa turns from westerly in the first month to easterly in the second month. The one of the two months where the zonal wind is closest to 0 m/s has been sampled. Such a wind reversal occurs exactly once at 33 hPa during every quasi-biennial cycle of the model run. Figure 4.6c shows the mean profiles of the zonal wind (black line) and vertical shear (blue line) over the selected months.

The sampling criterion allows some variability of the position of zero wind lines around 33 and 86 hPa (one model level) and, more important, of the strength of the QBO westerly jet at its core around 50 hPa and of the associated vertical shear. To further constrain the wind profile, only those months are sampled where the wind speed at 50 hPa does not exceed the sample mean by more than $\pm$ 1.5 standard deviations. Figure 4.6 shows the mean values over this final 177 samples. The low standard deviations of the zonal wind and the vertical shear illustrate the strong constraint the simple sampling criterions put on the strength and vertical extent of the lower-level westerly jet. At 50 hPa, the wind speed is maximal with a sample mean of 15.4 m/s and a standard deviation of 1.1 m/s (Fig. 4.6). At that level, the 25^{th} and the 75^{th} percentiles of the jet strength are 14.6 and 16.1 m/s (not shown). Hence, for MPI-ESM it was not necessary to constrain the zonal wind further. Applying the same sampling criterions on the actual zonal wind in ERA-40, the core of the lower-level QBO westerly jet has a sample mean zonal wind of 10.7 m/s with a standard deviation of 2.6 m/s and the 25^{th} and the 75^{th} percentiles at 9 and 13 m/s. The larger variability in ERA-40 compared to MPI-ESM is partly due to the small number of quasi-biennial cycles covered by ERA-40.

To further illustrate the accuracy of the sampling method for MPI-ESM, figure 4.7a shows the annual variations of the zonal wind and the shear of the selected months at 50 and 70 hPa, where the zonal wind and the shear, respectively, are strongest (Fig. 4.6c). Both terms have an annual cycle, but vary by little more than 0.5 m/s and 0.5 m/(s km) or less than 10% of the mean values. An issue emerges when separating the selected cases into bins of the months of the year. The sample has a bias towards showing more cases in spring and summer with 58 and 42 cases in April/May and June/July, respectively, compared to 13 and 17 cases in August/September and October/November, respectively, and 30 and 17 cases in December/January and February March, respectively. This strong clustering of the QBO easterly jet's onset can also be observed in ERA-40 (Dunkerton, 1990). In MPI-ESM, seasonal variations of the QBO easterly jet's descent rate, which currently are under investigation, are responsible for the strong clustering at 33 hPa compared to the broad distribution at 5 hPa (Fig. 4.3d). However, using the same amount of cases in each bin and omitting excess months did not qualitatively change the results discussed here.

To discuss the actual forcing of the lower-level westerly jet, Figure 4.6 also shows the

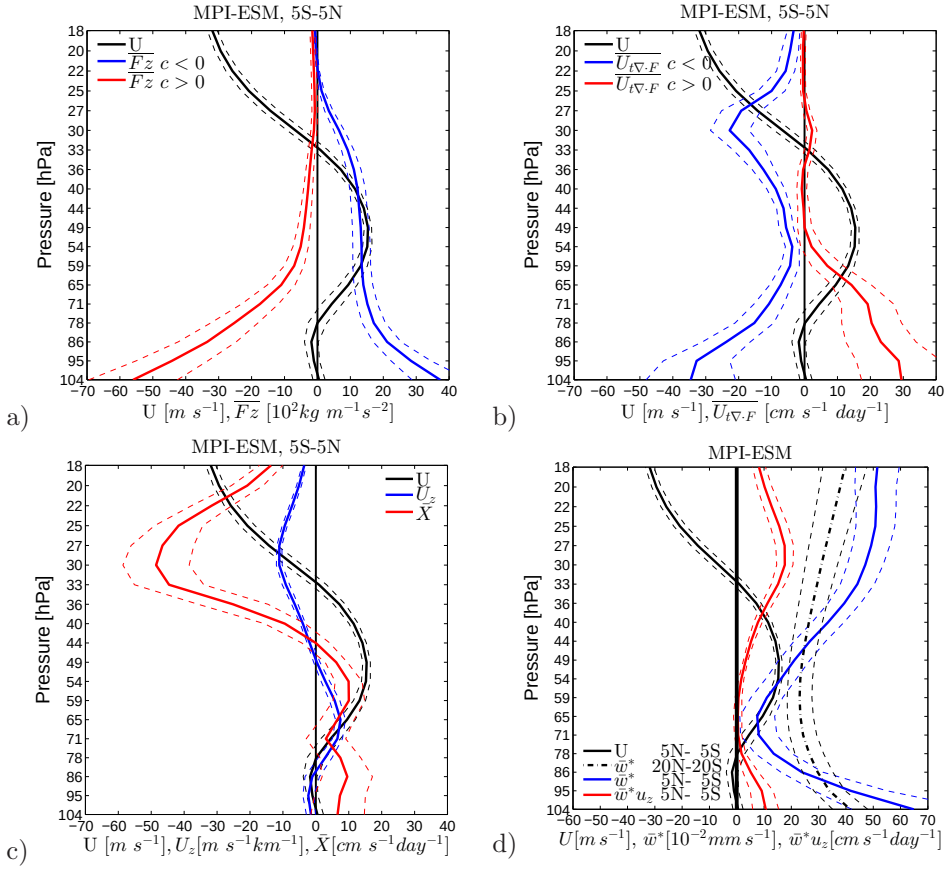

Figure 4.6: a): Profile of the zonal wind in m s^{-1} (black) and the Vertical EP-Flux component in 10^2 kg $m^{-1}s^{-2}$ (F_z) of easterly (blue) and westerly waves (red) averaged from 5°S to 5°N. Dashed lines indicate ± one standard deviation. Only months when the zero-wind line between the lower-level westerly jet and the easterly jet above is located at 33 hPa are considered. b): As a) but for the mean flow acceleration due to the divergence of the horizontal and vertical EP-Flux in cm s^{-1}day $^{-1}$ ($\bar{u}_{\nabla \cdot F}$). c): As a) but for the mean flow acceleration due to the parametrized wave drag and diffusion in cm s^{-1}day $^{-1}$ ($\overline{X}$, red) and the vertical shear of the zonal mean zonal wind in m s^{-1}km^{-1} ($\bar{u}_z$, blue). d) As a) but for the tropical and equatorial upwelling in 10^{-2}mm s^{-1} ($\bar{w}^*$, dash dotted black and blue, respectively) and the equatorial vertical momentum advection in cm s^{-1}day $^{-1}$ ($\bar{w}^* \bar{u}_z$, red). All panels show mean values over 177 samples.

sample mean profiles of the vertical EP-Flux component from easterly and westerly waves (Fig. 4.6a) , the mean flow acceleration due to resolved waves (Fig. 4.6b) and the residual forcing term (Fig. 4.6c). The decrease of the EP-Flux from 100 hPa to the core of the westerly jet at 50 hPa results in pronounced easterly and westerly wave forcing (Fig. 4.6a, b). Above 65 hPa, the parametrized wave forcing becomes stronger than the resolved wave forcing, especially around the zero wind line at 33 hPa (cf. Fig. 4.6b and c). This compares well to earlier studies of the QBO's momentum balance (Giorgetta et al., 2006; Kawatani et al., 2010a; Evan et al., 2012b), which showed that small scale gravity waves are equally important for the forcing of the QBO westerly jet as large scale equatorial waves and dominate the wave forcing of the QBO easterly jet.

Figure 4.7 shows the quantities shown in Figure 4.6 sorted by the month of the year.

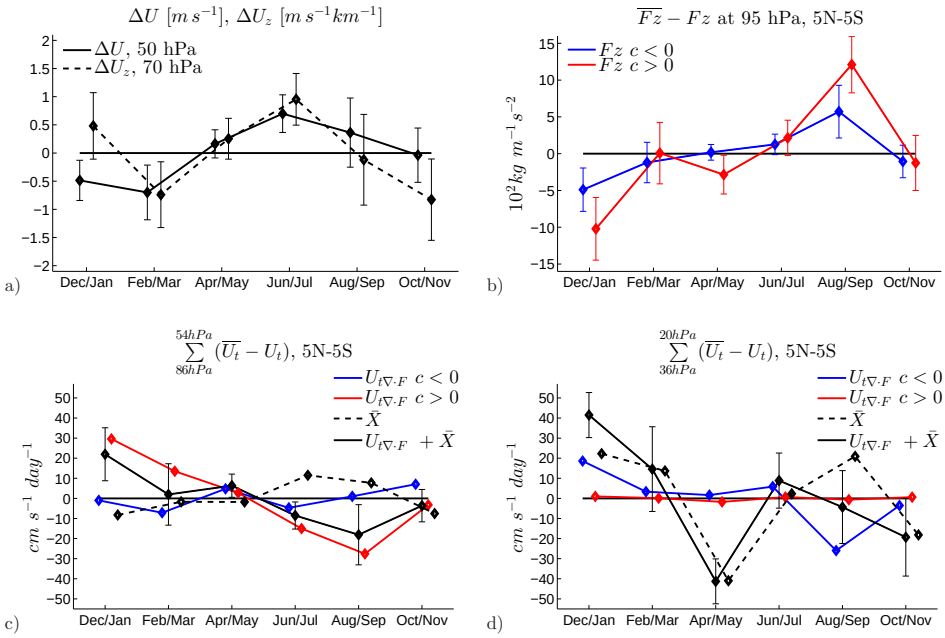

Figure 4.7: a) Zonal mean wind at 50 hPa in m s^{-1} (solid) and strength of the vertical shear at 70 hPa in m $s^{-1}km^{-1}$ (dashed). b): Vertical component of the EP-Flux due to resolved easterly (blue) and westerly waves (red) at 95 hPa. c) and d): Mean flow acceleration due to resolved easterly (blue) and westerly waves (red), parametrized waves and diffusion (dashed black) and their sum (solid black). The values are sums over the lower margin of the westerly jet from 86 to 54 hPa (c) and the easterly jet from 36 to 20 hPa (d). Errorbars indicate the 95% confidence interval. In all plots, only months when the zero-wind line between the lower-level westerly jet and the easterly jet above is located at 33 hPa are considered. The annual mean values of the selected months have been subtracted from the monthly values. In a), positive deviations display higher wind speeds and stronger shear. In b), negative (positive) perturbations of the EP-Flux carried by westerly (easterly) waves display stronger wave activity. In c) and d) positive (negative) deviations from westerly (easterly) wave forcing display stronger westerly (easterly) wave forcing. For the whole stratospheric profiles see Figure 4.6.

At 95 hPa, below the region influenced by the QBO, the vertical EP-Flux from resolved westerly waves has a pronounced seasonal cycle of roughly 25% or 10^3 kg/ms^2 around the mean value (Fig. 4.7b). Note that westerly (easterly) waves carry a negative (positive) EP-Flux (Fig. 4.6a), and negative (positive) deviations from the mean value display stronger wave activity. Hence, the westerly wave activity is highest in Dec/Jan, and lowest in Aug/Sep (Fig. 4.7b). The seasonal cycle of the resolved westerly wave forcing, summed over the depth of the lower-level QBO westerly jet from 86 to 54 hPa ($\pm$ 30 cm $s^{-1}day^{-1}$), follows the cycle of the EP-Flux (Fig. 4.7c). The seasonal cycle of EP-Flux carried by resolved easterly waves and its mean flow acceleration are weak compared to the seasonal cycle of the westerly forcing (Fig. 4.7b, c).

Over the depth of the lower-level westerly jet, the residual forcing $\bar{X}$, dominated by parametrized waves, shows an annual cycle ($\pm$ 10 cm $s^{-1}day^{-1}$), which is out of phase with the resolved westerly wave forcing. It is strongest from June to September and weakest in December/January (Fig. 4.7c). The parametrized wave sources are constant

in time. Therefore, the annual cycle of the parametrized wave forcing is the result of wave filtering between the wave sources at 700 hPa and the lowermost stratosphere. In total, the resolved and parametrized wave forcing of the lower-level westerly jet is lowest from June to September and strongest in December/January (Fig. 4.7c, black line).

Not only the forcing of the lower-level westerly jet contributes to its persistence, but also the drag from the QBO easterly jet, starting at 33 hPa in the selected months (Fig. 4.6). Summed over the lower edge of the easterly jet from 36 to 20 hPa (Fig. 4.6b,c), parametrized waves determine the semi-annual cycle of the total wave forcing ($\pm$ 40 cm s^{-1}day^{-1}). It is strongest (most negative) in April and May and weakest (most positive) from December to March (Fig. 4.7d).

It remains to analyze the influence of the equatorial upwelling on the evolution of the QBO jets in the lower stratosphere. Figure 4.6d shows the mean profiles of the equatorial and tropical residual vertical velocity and the vertical advection of momentum ($\bar{w}^*$ and $\bar{w}^* u_z$ in Eq. 4.1, respectively). The values have been averaged over 5°N to 5°S and over 20°N to 20°S for the equatorial and the tropical region, respectively.

The tropical residual vertical velocity is minimal with 0.25 mm/s at 70 hPa and increases below and above (Fig. 4.6d). The secondary circulation of the QBO (Randel et al., 1998) results in lower (higher) equatorial residual vertical velocities below (above) the core of the lower-level westerly jet at 50 hPa (Fig. 4.6d). The equatorial vertical momentum advection below and within the lower-level westerly jet is close to zero (Fig. 4.6d). It becomes positive above 50 hPa and is strongest just above the zero-wind line of the zonal wind at 33 hPa, where the momentum advection hinders the downward propagation off the easterly jet. Figure 4.8 shows the annual variations of the upwelling and the momentum advection below and above the lower-level westerly jet in the selected months. At 33 hPa, the tropical upwelling has an annual cycle (Fig. 4.8a) which is driven by the seasonal cycle of the northern hemisphere Rossby wave activity. The equatorial upwelling and vertical momentum advection, though altered by the QBO induced secondary circulation, closly follow the seasonal cycle of the tropical upwelling (Fig. 4.8b, c). The resistance to the propagation of the easterly jet is strongest in late

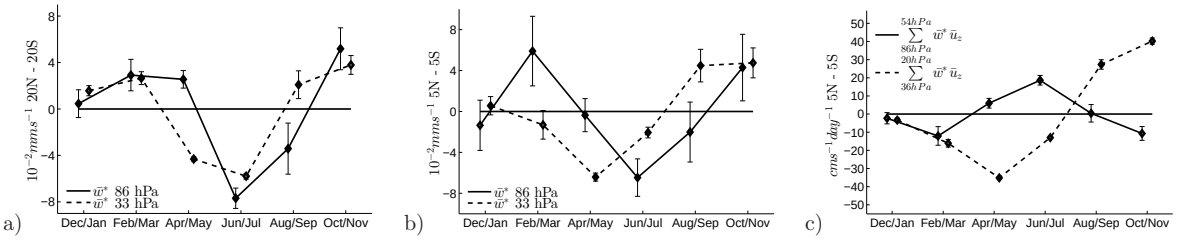

Figure 4.8: a) and b): Seasonal variations of the vertical upwelling $\bar{w}^*$ in (a) the tropical region (20°S to 20°N) and (b) the equatorial region (5°N to 5°S, blue). c): Vertical advection of momentum $\bar{w}^* \bar{u}_z$ in the equatorial region. Only months when the zero wind line between the lower-level westerly jet and the easterly jet above is located at 33 hPa are considered. Values below and above the QBO westerly jet in the selected months are drawn in solid and dashed lines, respectively. The mean values shown in Figure 4.6d have been subtracted from the monthly values. Errorbars indicate the 95% confidence intervals.

summer and fall and weakest in April/May (Fig. 4.8c).

After excluding the influence of the weakening lower-level westerly jet on the forcing, one can summarize Figures 4.6 to 4.8: From April to July, the lower-level westerly jet can erode quickly because the westerly wave forcing (Fig. 4.7c), which sustains the westerly jet, and the advective resistance to the propagation of the easterly jet above the lower-level westerly jet (Fig. 4.8c) are below their annual mean. At the same time, the wave forcing of the easterly jet (Fig. 4.7d) is stronger than the annual mean. Later in August/September, the westerly wave forcing is weakest within the annual cycle (Fig. 4.7c) and usually no longer capable of supporting a lower-level westerly jet, which has been weakened over spring and summer.

Qualitatively, the results shown in Figures 4.6 to 4.8 are similar if the zero-wind line, which separates the lower-level westerly jet and the easterly jet at 33 hPa, is at lower altitudes (not shown). This allows to further discuss the evolution of the QBO jets in the lower stratosphere in MPI-ESM in Figure 4.4. The total zonal acceleration shown in Figure 4.4a and b is just the sum of the forcing terms shown in Figures 4.7c and d and Figure 4.8c for a particular wind profile. Hence, the strong easterly forcing around 33 hPa from April to July in Figure 4.4a and b (month 0 to 3 and 5 to 8, respectively) results from the seasonally strong easterly wave forcing and the weak vertical advection illustrated in Figure 4.7c and 4.8c.

4.7 Phase Alignment in Comparison to ERA-40

After discussing seasonal differences in the evolution of the QBO westerly jets, Figures 4.9a and b show the seasonal distribution of QBO westerly jets in the deseasonalized wind initiated by the SAO at 5 hPa from April to June and from September to November throughout the stratosphere in MPI-ESM and ERA-40, respectively. The distributions shows two channel-like structures, which consist of jets initiated in spring and fall and which propagate downwards at similar rates. Seasonal peaks can be attributed to either the spring or the fall set of jets throughout the stratosphere. This illustrates that the coupling of the QBO westerly jet's onset to the SAO at high altitudes projects on the seasonal distribution of the QBO westerly jet's onset throughout the stratosphere.

Between 7 and 10 hPa, the distribution of the QBO westerly jets initiated at 5 hPa in fall (red shading in Fig. 4.9a, b) shows only few occurrences from January to March. This gap in the distribution is due to the stalling of the QBO westerly jets above 7 hPa shown in Figure 4.4 b and c.

In MPI-ESM, the QBO westerly jets starting at 5 hPa in spring and fall cluster at 55 hPa from July to December (Fig. 4.9c, gray bars) and from March to July (Fig. 4.9c, black bars), respectively, and thus, are responsible for peaks in the distribution of the onset of all QBO westerly jets (Fig. 4.9c, red curve). In ERA-40, the distribution at 55 hPa is less clear, due to the small sample size of only 18 quasi-biennial cycles (Fig. 4.9d). However, the onset of westerly jets tends to cluster from May to August (Fig. 4.9d, red line), mostly due to the frequent occurrence of QBO westerly jets starting

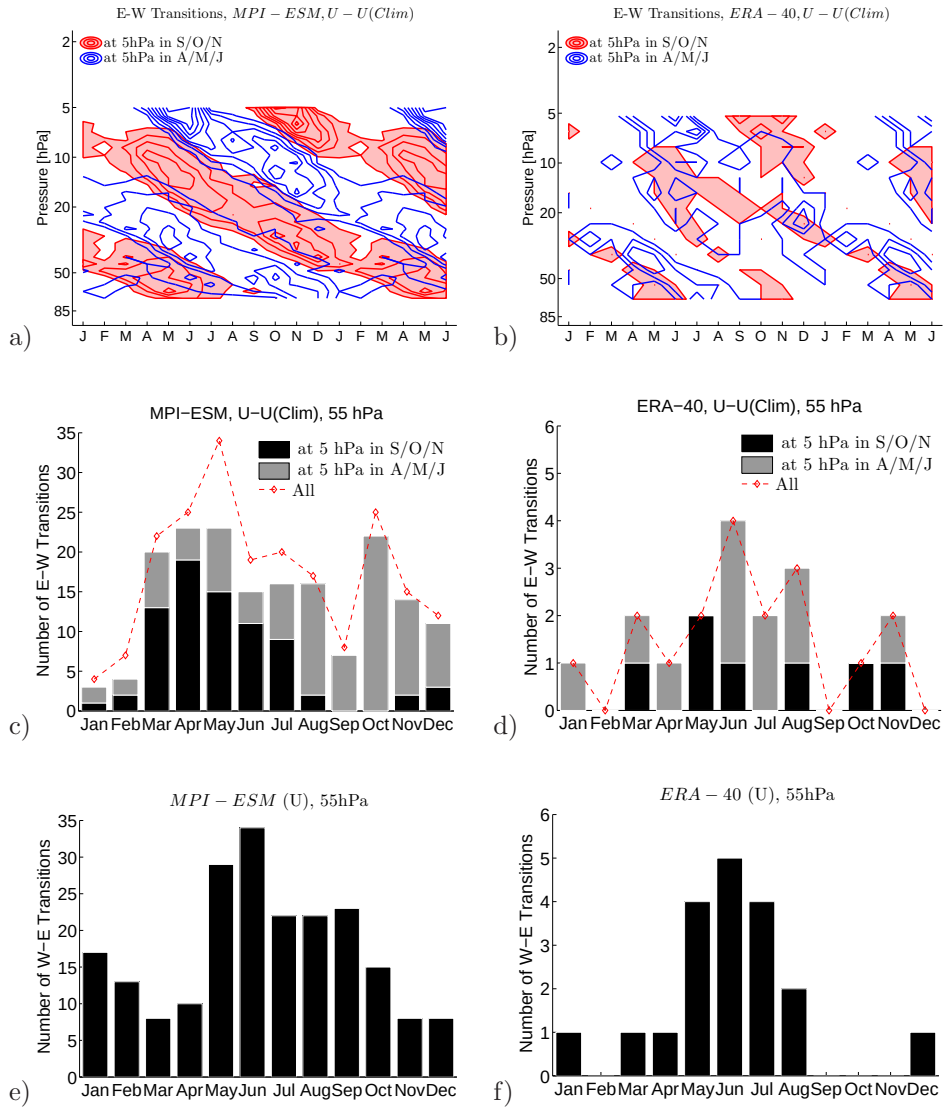

Figure 4.9: a), b): Distribution of the onset of the QBO westerly jets in the deseasonalized zonal wind throughout the stratosphere in (a) MPI-ESM and (b) ERA-40. The intervals are 5 cases for MPI-ESM and 1 case for ERA-40. Jets originating at 5 hPa in spring or fall are indicated in blue and red (plus shading), respectively. c), d): Distribution of the onset of the QBO westerly jets in the deseasonalized zonal wind at 55 hPa in (c) MPI-ESM and (d) ERA-40. Jets originating at 5 hPa in spring and fall are indicated in gray and black, respectively. The distribution of all QBO westerly jets is drawn in dashed red. e), f): Distribution of the onset of the QBO easterly jets in the zonal wind at 55 hPa in (e) MPI-ESM and (f) ERA-40.

at 5 hPa in spring (Fig. 4.9d, gray bars). This shift to earlier months in ERA-40 compared to MPI-ESM indicates that QBO westerly jets starting at 5 hPa in spring propagate downwards faster in ERA-40 than in MPI-ESM.

The tendency of the lower-level westerly jet to dissipate mainly during the summer months manifests in the clustering of the onset of the easterly jet. In MPI-ESM, it occurs at 55 hPa mainly between May and September, and less frequently during the rest of the year (Fig. 4.9e). This is in good agreement with the ERA-40 dataset (Fig. 4.9f).

4.8 Conclusions

In this study, seasonal aspects of the Quasi-Biennial Oscillation in the tropical stratosphere have been investigated with a 500 year long simulation of the Max Planck Institute-Earth System Model. The model internally generates a QBO, which, compared to the ERA-40 dataset, is realistic with respect to the period and vertical extent, but has a stronger amplitude.

First, it has been shown that the onset of QBO westerly jets at 5 hPa mainly occurs from April to June and from September to November (Section 4.4). In these months, the climatological SAO westerly jets reach the upper stratosphere. This, and the observation that every QBO westerly jet is an uninterrupted continuation of a SAO westerly jet, leads to the conclusion that the QBO westerly jets are induced by the SAO as described by previous authors (Lindzen and Holton, 1968; Dunkerton, 1997; Kuai et al., 2009).

Theoretical and idealized model studies and tank experiments showed that QBO westerly jets can evolve in the upper stratosphere without the periodic occurrence of SAO westerly jets (Holton and Lindzen, 1972; Plumb, 1977; Plumb and McEwan, 1978; Mayr et al., 2010). However, over the region where it is active, the westerly phase of the SAO facilitates the deposition of westerly wave momentum. When the QBO westerly jet is weak, SAO westerly jets can propagate deep into the upper stratosphere (Dunkerton and Delisi, 1997; Garcia et al., 1997; Peña Ortiz et al., 2010), leave the regions where periodical easterly momentum advection disturbs the westerly jet and continue as a westerly jet of the QBO.

Within the sets of QBO westerly jets starting at 5 hPa in spring or fall, jets propagate downwards at similar rates (Section 4.7). Thus, the seasonal clustering in the upper stratosphere extends to lower altitudes. Therefore, the coupling of the QBO westerly jet's onset to the SAO provides an explanation for the phase alignment of the QBO westerly jets found in MPI-ESM and in ERA-40 throughout the stratosphere.

Second, the presented study showed that the propagation of QBO westerly jets initiated in fall in ERA-40 and MPI-ESM comes to a halt at 7 hPa during winter (Fig. 4.4b, d). In MPI-ESM, this is due to variations of the equatorial upwelling and the parametrized wave forcing. In the simulation, the parametrized wave sources are constant in time. However, stronger wave filtering in the lower stratosphere and in the troposphere in winter impose the annual cycle of parametrized wave momentum reaching the stratosphere.

Third, it has been shown that the observed stalling of the QBO easterly jet in the lower stratosphere in fall and winter (e.g. Pascoe et al., 2005), which previously has been attributed to the seasonal strengthening of the vertical upwelling (Kinnersley and Pawson, 1996; Hampson and Haynes, 2004), is supported by a seasonal weakening of the parametrized easterly wave momentum reaching the stratosphere (Section 4.6). Further, the seasonal strengthening of the resolved westerly wave forcing in winter supports the QBO westerly jet in the lower stratosphere, which thus dissipates less quickly.

In the future, seasonal variations of the wave activity should be investigated in simulations resolving also QBO-relevant small scale gravity waves. Further, a comparison of global climate models internally generating a QBO to find consistent features of the QBO phase alignment and the coupling to the SAO is desirable. To investigate the SAO-QBO coupling, observations with high spatial and temporal resolution in the upper stratosphere are important. However, the principal limitation of a short observational record, with a small number of observed QBO cycles remains.

Acknowledgments We thank two anonymous reviewers for constructive suggestions improving the paper. The MPI-ESM modeling group is acknowledged for invaluable technical support. We thank Elisa Manzini and Hauke Schmidt for fruitfull discussions. Computational resources and the model output of the 500 year piControl simulation were made available by Deutsches Klimarechenzentrum (DKRZ)through support from the Bundesministerium für Bildung und Forschung (BMBF).

Chapter 5

Conclusions and Outlook

5.1 Conclusions

This thesis presents an analysis of the forcing of the quasi-biennial oscillation in the tropical stratosphere (QBO). The thesis is based on ECHAM6 and the Max Planck Institute Earth system model (MPI-ESM) truncated at T63 and T255 and with 95 levels in the vertical. The Hines parametrization of non orographic gravity waves (Hines, 1997a,b) accounts for the contribution of unresolved waves to the stratospheric momentum balance. Most of today's global climate models (GCM) truncate at similar wave numbers as MPI-ESM, and a small number of these GCMs also has a vertical resolution which is sufficient to resolve the wave-mean flow interactions crucial for the internal generation of the QBO. Giorgetta et al. (2006) showed how the forcing of the QBO in such a model splits into contributions from resolved and parametrized waves and advection. This study extends the work of Giorgetta et al. (2006) by analyzing the spectral decomposition of the resolved wave field based on temperature perturbations, the vertical EP-Flux and the zonal acceleration due to the EP-Flux divergence for ECHAM6 and MPI-ESM as done for high resolution models by Kawatani et al. (2010a); Ortland and Alexander (2011) and (Evan et al., 2012b). The study also relates the vertical structure of Kelvin waves to radiative wave damping, compares the importance of radiative and diffusive wave damping for the dissipation of waves and investigates the evolution of the resolved wave field and wave forcing when increasing the spectral resolution of the applied model. Further, the thesis investigates how seasonal variations of the equatorial wave activity, the upwelling and the semiannual oscillation in the uppermost stratosphere cause the well observed seasonal modulations of the quasi-biennial cycle.

Each chapter of this thesis has its own conclusion. In the following, the main results are concludet.

First, In order to simulate a QBO, the applied model has to excite a spectrum of tropical waves. The latent heating within convective clouds is considered the most important wave source in the tropics (Holton and Lindzen, 1972; Manzini and Hamilton, 1993; Fritts and Alexander, 2003, and references therein) and hence, the amplitude and the spatial and temporal variability of tropical convection in a GCM determines the amount

of resolved wave momentum available to force the QBO. Chapter 2 showed that in MPI-ESM, the spectral variance of tropical precipitation due to waves with wave numbers up to 20 and frequencies up to 0.5 cycles per day matches TRMM observations. The model overestimates the unorganized tropical precipitation and hence, underestimates the relative importance of Matsuno type Kelvin waves, Equatorial Rossby gravity waves and n1 easterly waves. However, equatorial waves are still the dominant modes of low frequency planetary scale precipitation variability. The model further underestimates the strength of the tropospheric wave sources with wave numbers higher than 20 and frequencies higher than 0.5 cycles per day, which suggests that also the wave momentum at theses spectral ranges is too low.

Second, a GCM has to allow the waves to carry wave momentum away from the tropospheric wave sources towards the shear zones associated with the QBO jets. Further, the model has to provide mechanisms for the waves to dissipate, such as radiative and diffusive wave damping, in order to deposit the wave momentum and accelerate the QBO jets. Chapter 2 compared the wave-number frequency spectra of the e-folding time of wave induced perturbations due to long wave radiation and horizontal diffusion. In accordance with idealized studies conducted by Ern et al. (2009a), long wave radiative damping, which increases with decreasing vertical wave number of the waves, is the most important damping process for large scale equatorial waves. For small scale gravity waves, horizontal diffusion is the most important damping mechanism. Due to the radiative and diffusive wave damping, the wave momentum decreases with increasing distance from the tropospheric wave sources, even in the absence of critical levels. Hence, the westerly and easterly wave momentum available to force the QBO jets decreases with increasing altitude of the zero wind lines marking the onset of the easterly and westerly jets. Further, it is found that the horizontal diffusion scheme efficiently suppresses waves with wave numbers larger than 30, independent from the wave's frequencies. Hence the suppressed spectrum, though resolved in the model, does not contribute considerably to the QBO's forcing.

Third, owing to the limited spectral resolution of MPI-ESM, unresolved waves and their interaction with the resolved flow are parametrized. In the model version truncating at T63, the parametrized gravity waves contribute 50 % and 70% to the forcing of the QBO westerly and easterly jet, respectively.

In Chapter 3, the influence of the spectral resolution on the QBO has been investigated by comparing AMIP-Type simulations of ECHAM6 truncated at T63 and T255. Considering resolved waves, the high resolution version has three advantages over the low resolution version.

First, the tropical wave sources in the high resolution version are stronger than in the low resolution version over the whole range of zonal wave numbers resolved in both models.

Second, in the high resolution version, the diffusive wave damping in the absence of critical levels acts on waves with much larger wave numbers than in the low resolution version. Hence, the forcing of the QBO jets due to waves with wave numbers ranging from 20 to 64 is stronger in the high resolution version.

Third and most obviously, the larger spectral resolution adds zonal wave momentum due to previously unresolved waves.

To account for the larger spectrum of resolved waves in the ECHAM6 version truncating at T255 compared to the version truncating at T63, the source spectrum of the parametrized waves has been weakened in the high resolution version. Hence, below 10 hPa, the sum of the resolved and parametrized wave forcing of the QBO jets is equal during most of the quasi-biennial cycle. However, due to its lower amplitude, the oscillation in the high resolution version needs less momentum to swing back and forth, thus, the QBO period is 7 months shorter. The lower amplitude is due to increased resolved easterly wave drag within the QBO westerly jet in the upper stratosphere.

To extend the perspective from a single QBO phase as in Chapter 2 and 3 to the whole quasi-biennial cycle, Chapter 4 shows how seasonal variations of the equatorial wave activity, the upwelling and the global circulation cause the well observed seasonal modulation of the QBO. Previous modeling studies addressing seasonal aspects of the QBO were based on prescribed variation of the vertical velocities within simplified models (Kinnersley and Pawson, 1996; Hampson and Haynes, 2004). Chapter 4 analyzes the first 500 years of the piControl simulation conducted with MPI-ESM where the QBO is embedded into the global circulation of the GCM. Hence, the variability of the resolved wave forcing and the equatorial upwelling, which are described in detail in Chapter 2 and 3, are internally generated and thus, consistent with the simulated climate. This sets a realistic setting, within which variations of the QBO can be investigated. In particular, Chapter 2 shows the following:

First, the onset of QBO westerly jets at 5 hPa mainly occurs from April to June and from September to November, when the climatological SAO westerly jets reach the upper stratosphere. Together with the observation that every QBO westerly jet is an uninterrupted continuation of a SAO westerly jet, this leads to the conclusion that the QBO westerly jets are induced by the SAO as described by previous authors (Lindzen and Holton, 1968; Dunkerton, 1997; Kuai et al., 2009). Within the sets of QBO westerly jets starting at 5 hPa in spring or fall, jets propagate downwards at similar rates (Section 4.7). Thus, the seasonal clustering in the upper stratosphere extends to lower altitudes. Therefore, the coupling of the QBO westerly jet's onset to the SAO provides an explanation for the phase alignment of the QBO westerly jets found in MPI-ESM and in ERA-40 throughout the stratosphere.

Second, the propagation of QBO westerly jets initiated in fall in ERA-40 and MPI-ESM comes to a halt at 7 hPa during winter. In MPI-ESM, this is due to variations of the equatorial upwelling and the parametrized wave forcing.

Third, the observed stalling of the QBO easterly jet in the lower stratosphere in fall and winter (e.g. Pascoe et al., 2005), which previously has been attributed to the seasonal strengthening of the vertical upwelling (Kinnersley and Pawson, 1996; Hampson and Haynes, 2004), is supported by a seasonal weakening of the parametrized easterly wave momentum reaching the stratosphere. Further, the seasonal strengthening of the resolved westerly wave forcing in winter supports the QBO westerly jet in the lower stratosphere, which thus dissipates less quickly.

5.2 Outlook and Ongoing Work

In ECHAM6 and MPI-ESM, the structure of the QBO, the zonal wind tendencies and the spectrum of tropical precipitation show systematic biases compared to the ERA-40 reanalysis data set and TRMM observations. The structure of the QBO is determined by the forcing, and the forcing is strongly dependent on convectively triggered waves. Hence, the shown biases of the QBO and its forcing lead to the conclusion that the stratospheric wave spectrum in the models discussed here is not fully representative for the wave field in nature but rather, for a wave field sufficient to force a QBO like oscillation.

Every general circulation model shows biases in the structure of the QBO and the wave field below and above the tropopause (Boville and Randel, 1992; Manzini and Hamilton, 1993; Horinouchi et al., 2003; Lott et al., 2013). The need to parametrize large parts of the wave spectrum led to some, though not full, understanding of how the projection of tropical convection on the spectra of freely propagating waves depends on the strength and depth of the convective heating and the background wind (see reviews by Fritts and Alexander, 2003; Alexander et al., 2010). The filtering of waves in the tropopause region additionally alters the wave spectra between the wave sources and the stratosphere (Yang et al., 2012; Maury et al., 2011; Lott et al., 2013). However, although the spectra of large scale equatorial waves in observations and in GCMs are well documented (Randel and Gille, 1991; Mote and Dunkerton, 2004; Alexander and Ortland, 2010; Horinouchi et al., 2003; Ern et al., 2008; Yang et al., 2012) and it is know that the choice of the convection parametrization strongly influences the magnitude of the wave spectra (Horinouchi et al., 2003), there are no studies directly relating the spectra of parametrized convection to resolved waves in GCMs. As a large part of tropical precipitation is convectively coupled (Wheeler et al., 2000), the understanding of the wave generation processes will not only improve the understanding of the dynamics of the QBO but also of the variability of tropical precipitation. To do so, one should compare the strength, the vertical structure and vertical horizontal and temporal extent of tropical precipitation events and the associated heating rates in GCMs to observations and try to improve, if necessary and possible, the representation of these parameters. Further, to investigate the origin of the stratospheric wave field, one could estimate the wave response to the convective heating based on observations and model data as done by Ortland and Alexander (2011) using idealized models.

Studies on the atmospheric wave spectrum generally suffer from the the lack of observational constraints on the magnitude of small scale waves. Using high resolution GCMs resolving also QBO-relevant small scale gravity waves, the realism of the simulated wave field can be verified indirectly by the wave induced forcing of the QBO, given that the QBO in the model has a realistic amplitude profile. Currently, such efforts are being made by gradually reducing the parametrized wave drag in the high resolution ECHAM6 to obtain the observed QBO period. Further, recently there has been success in predicting the zonal wind structure of the QBO some months ahead, and an analysis of the forcing of the QBO in these model runs should be illuminating.

Until high resolution models become standard in Climate science, the simulation of seasonal modulations of the QBO with course resolution models benefits from the

implementation of gravity wave parameterizations which couple the wave sources to convection (Kim et al., 2013) and the implementation of such a scheme into ECHAM6 is ongoing.

This thesis did not address the interaction of the QBO with other processes in the climate system. First, the scope of this study was to focus on the wave-mean flow interactions driving the QBO. Second, preliminary studies conducted in the course of this thesis showed that some of the teleconections involving the QBO, such as the Holton and Tan effect, the effect of the QBO on tropical convection and the influence of ENSO on the QBO are only weakly developed in MPI-ESM. Third, further research for example on the influence of volcanic aerosols on the QBO jets in the lower stratosphere is still ongoing.

List of Figures

Bibliography

Alexander, M. J., Geller, M., McLandress, C., Polavarapu, S., Preusse, P., Sassi, F., Sato, K., Eckermann, S., Ern, M., Hertzog, A., Kawatani, Y., Pulido, M., Shaw, T. a., Sigmond, M., Vincent, R., and Watanabe, S. (2010). Recent developments in gravity-wave effects in climate models and the global distribution of gravity-wave momentum flux from observations and models. *Q. J. R. Meteorol. Soc.*, (July):n/a–n/a.

Alexander, M. J. and Ortland, D. A. (2010). Equatorial waves in High Resolution Dynamics Limb Sounder (HIRDLS) data. *J. Geophys. Res.*, 115(D24):1–10.

Allen, S. and Vincent, R. (1995). Gravity wave activity in the lower atmosphere: Seasonal and latitudinal variations. *J. Geophys. Res.*, 100(D1):1327–1350.

Andrews, D., Holton, J., and Leovy, C. B. (1987). *Middle Atmosphere Dynamics*. Academic Press, 1 edition.

Anstey, J. A. and Shepherd, T. G. (2008). Response of the northern stratospheric polar vortex to the seasonal alignment of QBO phase transitions. *Geophys. Res. Lett.*, 35(22):4–7.

Anstey, J. A. and Shepherd, T. G. (2013). High-latitude influence of the quasi-biennial oscillation. *Q. J. R. Meteorol. Soc.*, 140(678):1–21.

Baldwin, M. P. (2005). Tropical stratospheric zonal winds in ECMWF ERA-40 reanalysis, rocketsonde data, and rawinsonde data. *Geophys. Res. Lett.*, 32(9):L09806.

Baldwin, M. P. and Dunkerton, T. J. (1991). Quasi-Biennial Oscillation above 10 MB. *Geophys. Res. Lett.*, 18(7):1205–1208.

Baldwin, M. P. and Dunkerton, T. J. (2001). Stratospheric harbingers of anomalous weather regimes. *Science*, 294(5542):581–4.

Baldwin, M. P., Gray, L. J., Dunkerton, T. J., Hamilton, K., Haynes, P. H., Randel, W. J., Holton, J. R., Alexander, M. J., Hirota, I., Horinouchi, T., Jones, D. B. A., Kinnersley, J. S., Marquardt, C., Sato, K., and Takahashi, M. (2001). The quasi-biennial oscillation. *Rev. Geophys.*, 39(2):179.

Booker, J. and Bretherton, F. (1967). The critical layer for internal gravity waves in a shear flow. *J. Fluid Mech.*, 27(03):513–539.

Boville, B. A. and Randel, W. J. (1992). Equatorial waves in a stratospheric GCM: Effects of vertical resolution. *J. Atmos. Sci.*, 49:785–801.

Canziani, P. O. and Holton, J. R. (1998). Kelvin waves and the quasi-biennial oscillation: An observational analysis. *J. Geophys. Res.*, 103(D24):31509.

Crueger, T., Hohenegger, C., and May, W. (2013). Tropical precipitation and convection changes in the Max Planck Institute Earth system model (MPI-ESM) in response to CO 2 forcing. *J. Adv. Model. Earth Syst.*, 5(1):85–97.

Delisi, D. P. and Dunkerton, T. J. (1988). Seasonal variation of the semiannual oscillation. *J. Atmos. Sci.*, 45(19):2772–2787.

Dunkerton, T. J. (1990). Annual variation of deseasonalized mean flow acceleration in the equatorial lower stratosphere. *Meteorol. Soc. Japan, J.*, 68(4):499–508.

Dunkerton, T. J. (1991). Nonlinear Propagation of Zonal Winds in an Atmosphere with Newtonian Cooling and Equatorial Wavedriving. *J. Atmos. Sci.*, 48(2):236–263.

Dunkerton, T. J. (1997). The role of gravity waves in the quasi-biennial oscillation. *J. Geophys. Res.*, 102(D22):26053–26076.

Dunkerton, T. J. and Baldwin, M. P. (1991). Quasi-biennial modulation of planetary-wave fluxes in the Northern Hemisphere winter. *J. Atmos. ...*, 48:1043–1061.

Dunkerton, T. J. and Delisi, D. P. (1985). Climatology of the equatorial lower stratosphere. *J. Atmos. Sci.*, 42(4):376–396.

Dunkerton, T. J. and Delisi, D. P. (1997). Interaction of the quasi-biennial oscillation and stratopause semiannual oscillation. *J. Geophys. Res.*, 102(D22):107–116O.

Dunkerton, T. J. and Fritts, D. (1984). Transiend Gravity Wave-Critical Layer Interaction. Part I: Convectve Adjustment and the Mean Zonal Acceleration. *J. Atmos. Sci.*, 41(6):992–1007.

Ern, M., Cho, H.-K., Preusse, P., and Eckermann, S. D. (2009a). Properties of the average distribution of equatorial Kelvin waves investigated with the GROGRAT ray tracer. *Atmos. Chem. Phys.*, 9(20):7973–7995.

Ern, M., Lehmann, C., Kaufmann, M., and Riese, M. (2009b). Spectral wave analysis at the mesopause from SCIAMACHY airglow data compared to SABER temperature spectra. *Ann. Geophys.*, 27(1):407–416.

Ern, M. and Preusse, P. (2009a). Quantification of the contribution of equatorial Kelvin waves to the QBO wind reversal in the stratosphere. *Geophys. Res. Lett.*, 36(21):L21801.

Ern, M. and Preusse, P. (2009b). Wave fluxes of equatorial Kelvin waves and QBO zonal wind forcing derived from SABER and ECMWF temperature space-time spectra. *Atmos. Chem. Phys. Discuss.*, 9(2):5623–5677.

Ern, M., Preusse, P., Gille, J. C., Hepplewhite, C. L., Mlynczak, M. G., Russell, J. M., and Riese, M. (2011). Implications for atmospheric dynamics derived from global observations of gravity wave momentum flux in stratosphere and mesosphere. *J. Geophys. Res.*, 116(D19):1–24.

Ern, M., Preusse, P., Krebsbach, M., Mlynczak, M. G., and Russell, J. M. (2008). Equatorial wave analysis from SABER and ECMWF temperatures. *Atmos. Chem. Phys.*, 8(4):845–869.

Evan, S., Alexander, M. J., and Dudhia, J. (2012a). Model Study of Intermediate-Scale Tropical InertiaGravity Waves and Comparison to TWP-ICE Campaign Observations. *J. Atmos. Sci.*, 69(2):591–610.

Evan, S., Alexander, M. J., and Dudhia, J. (2012b). WRF simulations of convectively generated gravity waves in opposite QBO phases. *J. Geophys. Res. Atmos.*, 117:D12117.

Fels, S. B. (1982). A Parameterization of Scale-Dependent Radiative Damping Rates in the Middle Atmosphere. *J. Atmos. Sci.*, 39:1141–1152.

Fritts, D. and Alexander, M. J. (2003). Gravity wave dynamics and effects in the middle atmosphere. *Rev. Geophys.*, 41(1):1–64.

Garcia, R. R., Dunkerton, T. J., Lieberman, R. S., and Vincent, R. A. (1997). Climatology of the semiannual oscillation of the tropical middle atmosphere. *J. Geophys. Res.*, 102(27):19–32.

Garcia, R. R. and Lieberman, R. (2005). Large-scale waves in the mesosphere and lower thermosphere observed by SABER. *J. Atmos. Sci.*, 62:4384–4399.

Giorgetta, M. A., Bengtsson, L., and Arpe, K. (1999). An investigation of QBO signals in the east Asian and Indian monsoon in GCM experiments. *Clim. Dyn.*, 15(6):435–450.

Giorgetta, M. A., Jungclaus, J., Reick, C., Legutke, S., Brovkin, V., Crueger, T., Esch, M., Fieg, K., Glushak, K., Gayler, V., Haak, H., Hollweg, H.-D., Kinne, S., Kornblueh, L., Matei, D., Mauritsen, Thorsten Mikolajewicz, U., Müller, W., Notz, D., Raddatz, T., Rast, S., Roeckner, E., Salzmann, M., Schmidt, H., Schnur, Reiner Segschneider, J., Six, K., Stockhause, Martina Wegner, J., Widmann, H., Wieners, Karl-Hermann Claussen, M., Marotzke, J., and Stevens, B. (2013a). CMIP5 simulations of the Max Planck Institute for Meteorology (MPI-M) based on the MPI-ESM-MR model: The amip experiment.

Giorgetta, M. A., Jungclaus, J., Reick, C., Legutke, S., Brovkin, V., Crueger, T., Esch, M., Fieg, K., Glushak, K., Gayler, V., Haak, H., Hollweg, H. D. Kinne, S., Kornblueh, L., Matei, D., Mauritsen, T., Mikolajewicz, U., Müller, W., Notz, D., Raddatz, T. J., Rast, S., Roeckner, E., Salzmann, M., Schmidt, H., Schnur, R., Segschneider, J., Six, K., Stockhause, M., Wegner, J., Widmann, H., Wieners, K. H., Claussen, M., Marotzke, J., and Stevens, B. (2012). CMIP5 simulations of the Max Planck Institute for Meteorology (MPI-M) based on the MPI-ESM-MR model: The piControl experiment, served by ESGF. World Data Center for Climate.

Giorgetta, M. A., Jungclaus, J., Reick, C., Legutke, S., Brovkin, V., Crueger, T., Esch, M., Fieg, K., Glushak, K., Gayler, V., Haak, H., Hollweg, H. D. Kinne, S., Kornblueh, L., Matei, D., Mauritsen, T., Mikolajewicz, U., Müller, W., Notz, D., Raddatz, T. J., Rast, S., Roeckner, E., Salzmann, M., Schmidt, H., Schnur, R., Segschneider, J., Six, K., Stockhause, M., Wegner, J., Widmann, H., Wieners, K. H., Claussen, M., Marotzke, J., and Stevens, B. (2013b). Climate and carbon cycle changes from 1850 to 2100 in MPI-ESM simulations for the Coupled Model Intercomparison Project phase 5 (2013). *J. Adv. Model. Earth Syst.*, 5(3):572–597.

Giorgetta, M. A., Manzini, E., and Roeckner, E. (2002). Forcing of the quasi-biennial oscillation from a broad spectrum of atmospheric waves. *Geophys. Res. Lett.*, 29(8):1245.

Giorgetta, M. A., Manzini, E., Roeckner, E., Esch, M., and Bengtsson, L. (2006). Climatology and forcing of the quasi-biennial oscillation in the MAECHAM5 model. *J. Clim.*, 19:3882–3901.

Gray, L. J. and Pyle, J. (1989). A two-dimensional model of the quasi-biennial oscillation of ozone. *J. Atmos. Sci.*, 46(2):203–220.

Hamilton, K. and Hsieh, W. (2002). Representation of the quasi-biennial oscillation in the tropical stratospheric wind by nonlinear principal component analysis. *J. Geophys. Res.*, 107:4232.

Hampson, J. and Haynes, P. (2004). Phase alignment of the tropical stratospheric QBO in the annual cycle. *J. Atmos. Sci.*, 61(21):2627–2637.

Hines, C. O. (1997a). Doppler-spread parameterization of gravity-wave momentum deposition in the middle atmosphere. Part 1: Basic formulation. *J. Atmos. Solar-Terrestrial Phys.*, 59(4):371–386.

Hines, C. O. (1997b). Doppler-spread parameterization of gravity-wave momentum deposition in the middle atmosphere. Part 2: Broad and quasi monochromatic spectra, and implementation. *J. Atmos. Solar-Terrestrial Phys.*, 59(4):387–400.

Hitchcock, P., Shepherd, T. G., and Yoden, S. (2010). On the Approximation of Local and Linear Radiative Damping in the Middle Atmosphere. *J. Atmos. Sci.*, 67(6):2070–2085.

Holton, J. (1972). Waves in the equatorial stratosphere generated by tropospheric heat sources. *J. Atmos. Sci.*, 29(2):368–375.

Holton, J. and Lindzen, R. (1972). An updated theory for the quasi-biennial cycle of the tropical stratosphere. *J. Atmos. Sci.*, 29(6):1076–1080.

Holton, J. and Tan, H. (1980). The influence of the equatorial quasi-biennial oscillation on the global circulation at 50 mb. *J. Atmos. Sci.*, 37(10):2200–2208.

Horinouchi, T., Pawson, S., Shibata, K., Langematz, U., Manzini, E., Giorgetta, M. A., Sassi, F., Wilson, R., Hamilton, K., De Grandpre, J., and Others (2003). Tropical cumulus convection and upward-propagating waves in middle-atmospheric GCMs. *J. Atmos. Sci.*, 60:2765–2782.

Huffman, G. J., Bolvin, D. T., Nelkin, E. J., Wolff, D. B., Adler, R. F., Gu, G., Hong, Y., Bowman, K. P., and Stocker, E. F. (2007). The TRMM Multisatellite Precipitation Analysis (TMPA): Quasi-Global, Multiyear, Combined-Sensor Precipitation Estimates at Fine Scales. *J. Hydrometeorol.*, 8(1):38–55.

Jungclaus, J., Fischer, N., Haak, H., Lohmann, K., Marotzke, J., Matei, D., Mikolajewicz, U., Notz, D., and von Storch, J. (2013). Characteristics of the ocean simulations in MPIOM, the ocean component of the MPI-Earth system model. *J. Adv. Model. Earth Syst.*, 5(2):422–446.

Kawatani, Y., Watanabe, S., Sato, K., Dunkerton, T. J., Miyahara, S., and Takahashi, M. (2010a). The Roles of Equatorial Trapped Waves and Internal InertiaGravity Waves in Driving the Quasi-Biennial Oscillation. Part I: Zonal Mean Wave Forcing. *J. Atmos. Sci.*, 67(4):963–980.

Kawatani, Y., Watanabe, S., Sato, K., Dunkerton, T. J., Miyahara, S., and Takahashi, M. (2010b). The Roles of Equatorial Trapped Waves and Internal InertiaGravity Waves in Driving the Quasi-Biennial Oscillation. Part II: Three-Dimensional Distribution of Wave Forcing. *J. Atmos. Sci.*, 67(4):981–997.

Kiladis, G., Wheeler, M., Haertel, P., Straub, K., and Roundy, P. (2009). Convectively coupled equatorial waves. *Rev. Geophys.*, 47(RG2003).

Kim, J.-E. and Alexander, M. J. (2013). Tropical precipitation variability and convectively coupled equatorial waves on submonthly time-scales in reanalyses and TRMM. *J. Clim.*, 26:3013–3030.

Kim, Y.-H., Bushell, A. C., Jackson, D. R., and Chun, H.-Y. (2013). Impacts of introducing a convective gravity-wave parameterization upon the QBO in the Met Office Unified Model. *Geophys. Res. Lett.*, 40(9):1873–1877.

Kinnersley, J. and Pawson, S. (1996). The descent rates of the shear zones of the equatorial QBO. *J. Atmos. Sci.*, 53(14):1937–1949.

Krismer, T. R. and Giorgetta, M. A. (2014). Wave Forcing of the Quasi-Biennial Oscillation. *J. Atmos. Sci.*, in revisio.

Krismer, T. R., Giorgetta, M. A., and Esch, M. (2013). Seasonal aspects of the quasibiennial oscillation in MPIESM and ERA40. *J. Adv. Model. Earth Syst.*, 5(2):406–421.

Kuai, L., Shia, R.-L., Jiang, X., Tung, K.-K., and Yung, Y. L. (2009). Nonstationary Synchronization of Equatorial QBO with SAO in Observations and a Model. *J. Atmos. Sci.*, 66(6):1654–1664.

Labitzke, K. (1987). Sunspots, the QBO, and the stratospheric temperature in the north polar region. *Geophys. Res. Lett.*, 14(5):535–537.

Labitzke, K. and Loon, H. V. (1988). Associations between the 11-year solar cycle, the QBO and the atmosphere. Part I: the troposphere and stratosphere in the northern hemisphere in winter. *J. Atmos. Terr. Phys.*, 50(3):197–206.

Li, T., Leblanc, T., McDermid, I. S., Wu, D. L., Dou, X., and Wang, S. (2010). Seasonal and interannual variability of gravity wave activity revealed by long-term lidar observations over Mauna Loa Observatory, Hawaii. *J. Geophys. Res.*, 115(D13103):1–10.

Liess, S. and Geller, M. a. (2012). On the relationship between QBO and distribution of tropical deep convection. *J. Geophys. Res.*, 117(D0310).

Lin, J., Kiladis, G., Mapes, B., Weickmann, K., Sperber, K., Lin, W., Wheeler, M., Schubert, S., Del Genio, A., Donner, L., and Others (2006). Tropical intraseasonal variability in 14 IPCC AR4 climate models. Part I: Convective signals. *J. Clim.*, 19(12):2665–2690.

Lindzen, R. (1971). Equatorial Planetary Waves in Shear: Part I. *J. Atmos. Sci.*, 28(4):609–622.

Lindzen, R. and Holton, J. (1968). A Theory of the Quasi-Biennial Oscillation. *J. Atmos. Sci.*, 25:1095–1107.

Lott, F. (1999). Alleviation of Stationary Biases in a GCM through a Mountain Drag Parameterization Scheme and a Simple Representation of Mountain Lift Forces. *Mon. Weather Rev.*, 127:788–801.

Lott, F., Denvil, S., Butchart, N., Cagnazzo, C., Giorgetta, M. A., Hardiman, S., Manzini, E., Krismer, T. R., Duvel, J.-p., Maury, P., Scinocca, J., Watanabe, S., and Seiji, Y. (2013). Kelvin and Rossby gravity waves packets in the lower stratosphere of some high-top CMIP5 models. *J. Geophys. Res. Atmos.*, accepted.

Lu, B.-W., Pandolfo, L., and Hamilton, K. (2009). Nonlinear Representation of the Quasi-Biennial Oscillation. *J. Atmos. Sci.*, 66(7):1886–1904.

Manzini, E., Giorgetta, M. a., Esch, M., Kornblueh, L., and Roeckner, E. (2006). The Influence of Sea Surface Temperatures on the Northern Winter Stratosphere: Ensemble Simulations with the MAECHAM5 Model. *J. Clim.*, 19(15):3863–3881.

Manzini, E. and Hamilton, K. (1993). Middle atmospheric traveling waves forced by latent and convective heating. *J. Atmos. Sci.*, 50:2180–2200.

Manzini, E. and McFarlane, N. a. (1998). The effect of varying the source spectrum of a gravity wave parameterization in a middle atmosphere general circulation model. *J. Geophys. Res.*, 103(D24):31,523–31,539.

Marsland, S., Haak, H., Jungclaus, J., Latif, M., and Röske, F. (2003). The Max-Planck-Institute global ocean/sea ice model with orthogonal curvilinear coordinates. *Ocean Model.*, 5(2):91–127.

Matsuno, T. (1966). Quasi-Geostrophic Motions in the Equatorial Area. *J. Meteorol. Soc. Japan*, 44(2):25–43.

Mauritsen, T., Stevens, B., Roeckner, E., Crueger, T., Esch, M., Giorgetta, M. A., Haak, H., Jungclaus, J., Klocke, D., Matei, D., Mikolajewicz, U., Notz, D., Pincus, R., Schmidt, H., and Tomassini, L. (2012). Tuning the climate of a global model. *J. Adv. Model. Earth Syst.*, 4(3).

Maury, P., Lott, F., Guez, L., and Duvel, J.-P. (2011). Tropical variability and stratospheric equatorial waves in the IPSLCM5 model. *Clim. Dyn.*, 40(9-10):2331–2344.

Mayr, H., Mengel, J., Chan, K., and Huang, F. (2010). Middle atmosphere dynamics with gravity wave interactions in the numerical spectral model: Zonal-mean variations. *J. Atmos. Solar-Terrestrial Phys.*, 72:807–828.

Möbis, B. and Stevens, B. (2012). Factors controlling the position of the Intertropical Convergence Zone on an aquaplanet. *J. Adv. Model. Earth Syst.*, 4(4).

Mote, P. W. and Dunkerton, T. J. (2004). Kelvin wave signatures in stratospheric trace constituents. *J. Geophys. Res.*, 109(D3):D03101.

Mote, P. W., Rosenlof, K. H., Mcintyre, E., Carr, E. S., Gille, J. C., Holton, J., Kinnersley, S., Pumphrey, H. C., Russell, M., and Wal, J. W. (1996). An atmospheric tape recorder : The imprint of tropical tropopause temperatures on stratospheric water vapor. *J. Geophys. Res.*, 101(95):3989–4006.

Naujokat, B. (1986). An Update of the Observed Quasi-Biennial Oscillation of the Stratospheric Winds over the Tropics. *J. Atmos. Sci.*, 43(17):1873–1877.

Nordeng, T. E. (1996). Extended versions of the convective parametrization scheme at ECMWF and their impact on the mean and transient activity of the model in the tropics. ECMWF Research Department Techn. Memo 206, ECMWF, Reading,.

Orr, A., Bechtold, P., Scinocca, J., Ern, M., and Janiskova, M. (2010). Improved Middle Atmosphere Climate and Forecasts in the ECMWF Model through a Nonorographic Gravity Wave Drag Parameterization. *J. Clim.*, 23(22):5905–5926.

Ortland, D. A. and Alexander, M. J. (2011). Solutions to the Vertical Structure Equation for Simple Models of the Tropical Troposphere. *J. Atmos. Sci.*, 68(9):2061–2072.

Ortland, D. A., Alexander, M. J., and Grimsdell, A. W. (2011). On the Wave Spectrum Generated by Tropical Heating. *J. Atmos. Sci.*, 68(9):2042–2060.

Pascoe, C. L., Gray, L. J., Crooks, S. A., Juckes, M. N., and Baldwin, M. P. (2005). The quasi-biennial oscillation: Analysis using ERA-40 data. *J. Geophys. Res.*, 110(D8):1–13.

Peña Ortiz, C., Ribera, P., Garcia-Herrera, R., Giorgetta, M. A., and Garcia, R. R. (2008). Forcing mechanism of the seasonally asymmetric quasi-biennial oscillation secondary circulation in ERA-40 and MAECHAM5. *J. Geophys. Res.*, 113(D16):1–16.

Peña Ortiz, C., Schmidt, H., Giorgetta, M. A., and Keller, M. (2010). QBO modulation of the semiannual oscillation in MAECHAM5 and HAMMONIA. *J. Geophys. Res.*, 115(D21):1–19.

Piani, C., Durran, D., and Alexander, M. J. (2000). A numerical study of three-dimensional gravity waves triggered by deep tropical convection and their role in the dynamics of the QBO. *J. Atmos. Sci.*, 57(22):3689–3702.

Plumb, R. (1977). The Interaction of Two Internal Waves with the Mean Flow: Implications fot the Theory of the Quasi-Biennial Oscillation. *J. Atmos. Sci.*, 34(12):1847–18598.

Plumb, R. and McEwan, A. (1978). The Instability of a Forced Standing Wave in a Viscous Stratified Fluid: A Laboratory Analogue of. the Quasi-Biennial Oscillation. *J. Atmos. Sci.*, 35:1827–1839.

Punge, H. J. and Giorgetta, M. A. (2007). Differences between the QBO in the first and in the second half of the ERA-40 reanalysis. *Atmos. Chem. Phys.*, 7(2005):599–608.

Punge, H. J. and Giorgetta, M. A. (2008). Net effect of the QBO in a chemistry climate model. *Atmos. Chem. Phys.*, 8:6505–6525.

Raddatz, T. J., Reick, C. H., Knorr, W., Kattge, J., Roeckner, E., Schnur, R., Schnitzler, K.-G., Wetzel, P., and Jungclaus, J. (2007). Will the tropical land biosphere dominate the climate carbon cycle feedback during the twenty-first century? *Clim. Dyn.*, 29(6):565–574.

Randel, W. J. and Gille, J. C. (1991). Kelvin wave variability in the upper stratosphere observed in SBUV ozone data. *J. Atmos. Sci.*, 48:2330–2349.

Randel, W. J., Wu, F., Russell, J. M., Roche, A., and Waters, J. (1998). Seasonal Cycles and QBO Variations in Stratospheric CH 4 and H 2 O Observed in UARS HALOE Data. *J. Atmos. Sci.*, 55(2):163–185.

Reed, R. J., Campbell, W. J., Rasmussen, L. A., and Roesas, D. G. (1961). Evidence of a Downward-Propagating , Annual Wind Reversal in the Equatorial Stratosphere the period. *J. Geophys. Res.*, 66(3):813–818.

Roeckner, E., Bäuml, G., Bonaventura, L., Brokopf, R., Esch, M., Giorgetta, M. A., Hagemann, S., Kirchner, I., Kornblueh, L., and Tompkins, A. (2003). The Atmospheric general circulation model ECHAM5 Report No. 349 Model description. Technical Report 349.

Sato, K. and Dunkerton, T. J. (1997). Estimates of momentum flux associated with equatorial Kelvin and gravity waves. *J. Geophys. Res.*, 102(D22):247–261.

Scaife, A. A., Butchart, N., and Warner, C. D. (2000). Realistic Quasi-Biennial Oscillations in a simulation of the global climate. *Geophys. Res. Lett.*, 27(1):3481–3484.

Schmidt, H., Alterskjæ r, K., Bou Karam, D., Boucher, O., Jones, A., Kristjánsson, J. E., Niemeier, U., Schulz, M., Aaheim, A., Benduhn, F., Lawrence, M., and Timmreck, C. (2012a). Solar irradiance reduction to counteract radiative forcing from a quadrupling of CO2: climate responses simulated by four earth system models. *Earth Syst. Dyn.*, 3(1):63–78.

Schmidt, H., Rast, S., Bunzel, F., Esch, M., Giorgetta, M. A., Kinne, S., Krismer, T. R., Stenchikov, G., Timmreck, C., Tomassini, L., and Walz, M. (2012b). The response of the middle atmosphere to anthropogenic and natural forcing in the CMIP5 simulations with the MPI-ESM. *J. Adv. Model. Earth Syst.*, submitted.

Schoeberl, M. R., Douglass, a. R., Stolarski, R. S., Pawson, S., Strahan, S. E., and Read, W. (2008). Comparison of lower stratospheric tropical mean vertical velocities. *J. Geophys. Res.*, 113(D24):D24109.

Stevens, B., Giorgetta, M. A., Esch, M., Mauritsen, T., Crueger, T., Rast, S., Salzmann, M., Schmidt, H., Bader, J., Block, K., Brokopf, R., Fast, I., Kinne, S., Kornblueh, L., Lohmann, U., Pincus, R., Reichler, T., and Roeckner, E. (2012). The Atmospheric Component of the MPI-ESM: ECHAM6. *J. Adv. Model. Earth Syst.*, 5(2):146–172.

Takahashi, M. (1996). Simulation of the stratospheric Quasi-Biennial Oscillation using a general circulation model. *Geophys. Res. Lett.*, 23(6):661–664.

Takahashi, M. (1999). Simulation of the quasi-biennial oscillation in a general circulation model. *Geophys. Res. Lett.*, 26(9):1307–1310.

Thompson, D. W. J., Baldwin, M. P., and Wallace, J. M. (2002). Stratospheric Connection to Northern Hemisphere Wintertime Weather : Implications for Prediction. *J. Clim.*, 15:1421–1428.

Thompson, D. W. J. and Wallace, J. M. (2001). Regional climate impacts of the Northern Hemisphere annular mode. *Science*, 293(5527):85–9.

Tiedtke, M. (1989). A comprehensive mass flux scheme for cumulus parameterization in large- scale models. *Mon. Weather Rev.*, 117(8):1779–1800.

Tomassini, L., Gerber, E. P., Baldwin, M. P., Bunzel, F., and Giorgetta, M. A. (2012). The role of stratosphere-troposphere coupling in the occurrence of extreme winter cold spells over northern Europe. *J. Adv. Model. Earth Syst.*, 4(3).

Veryard, R. G. and Ebdon, R. A. (1961). Fluctuations in tropical stratospheric winds. *Meteorol. Mag.*, 90:125–143.

Wallace, J. M., Panetta, R. L., and Estberg, J. (1993). Representation of the Equatorial Stratsopheric Quasi-Biennial Oscillation in EOF Phase Space. *J. Atmos. Sci.*, 50(12):1751–1762.

Watson, P. a. G. and Gray, L. J. (2014). How Does the Quasi-Biennial Oscillation Affect the Stratospheric Polar Vortex? *J. Atmos. Sci.*, 71(1):391–409.

Wheeler, M. and Kiladis, G. (1999). Convectively coupled equatorial waves: Analysis of clouds and temperature in the wavenumber- frequency domain. *J. Atmos. Sci.*, 56:374–399.

Wheeler, M., Kiladis, G., and Webster, P. (2000). Large-scale dynamical fields associated with convectively coupled equatorial waves. *J. Atmos. Sci.*, 57(5):613–640.

Xue, X.-H., Liu, H.-L., and Dou, X.-K. (2012). Parameterization of the inertial gravity waves and generation of the quasi-biennial oscillation. *J. Geophys. Res.*, 117(D06103).

Yang, G.-Y., Hoskins, B., and Gray, L. J. (2012). The Influence of the QBO on the Propagation of Equatorial Waves into the Stratosphere. *J. Atmos. Sci.*, 69(10):2959–2982.

Yang, G.-Y., Hoskins, B. J., and Slingo, J. M. (2011). Equatorial Waves in Opposite QBO Phases. *J. Atmos. Sci.*, 68(4):839–862.

Zhu, X. (1993). Radiative Damping Revisited: Parameterization of Damping Rate in the Middle Atmosphere. *J. Atmos. Sci.*, 50:3008–3021.

Acknowledgements

First and foremost, special thanks are due to my adviser Marco Giorgetta for his precise, steady, subtle, professional and personal supervision as well as his companionship during countless safely climbed routes, exhausting runs and speedy biking trips.

I thank Hauke Schmidt and Elisa Manzini for being experienced co-advisers, for their indispensable scientific input and their personal interest. I thank Jin-Song von Storch for keeping us all on track, Bjorn Stevens for his patronage and Monika Esch for her technical support.

I thank the Middle and Upper Atmosphere Group with Ulrike, Claudia, Matthias, Katharina, Felix and Stergios for being my in-house scientific pear group.

Special thanks are due to Antje Weitz, Cornelia Kampmann and Wiebke Boehm from the Max Planck Research School for Earth System Modeling for their immense effort to keep the sea calm at any time.

For their warm welcome, familiar atmosphere and the joyful time we spent together, I thank my office mates of the first hour, Natascha and Andreas. I also thank Rabea and Bart for accompanying the final days as a PhD.

I thank my fellow students and friends, Eleftheria, Suvarchal, Fanni, Olga, Stergios, Dimitris, Nasia Steffen, Fanny, Peter, Michi, Sebastian, Philipp, Thomas, David, Rika, Malte, Louise, Freja, Florian, Francesco, Moritz, Niklas, Ben, and so many more for the time we spent together and for always walking on for another hour.

I thank my Parents, Christine and Rainer, and my sisters and brother, Hanna, Lukas and Isabella for being family. And I thank Olga for shining every day.



ISSN 1614-1199